Doctoral Thesis

Study on Pore Structure Control and Characterization of Porous Ceramics Using Starch as a Pore-Forming Agent

デンプンを造孔剤に用いたセラミックス多孔体の

気孔構造制御とその評価に関する研究

Masako Uematsu

植松 昌子

Materials Chemistry and Engineering Course

Graduate School of Chemical Sciences and Engineering

Hokkaido University

March, 2023

Acknowledgements

First of all, I would like to express my sincere gratitude to my supervisor, Professor Tetsuo Uchikoshi, for his encouragement, extensive discussions, and broad mind.

I would like to thank the thesis committee members, Professor Kiyoharu Tadanaga, Professor Yuji Masubuchi, Professor Toshihiro Shimada, and Professor Naoto Shirahata, for their valuable comments on my PhD work.

Most of the experiments in this thesis were performed at the National Institute for Materials Science (NIMS) under the Hokkaido University - NIMS Joint Graduate School Program. I sincerely thank all of the involved NIMS staff members, especially those of the Fine Particles Engineering group of NIMS for giving me the time for the various experiments. I would like to give my special thanks to Dr. Kento Ishii, Ms. Megumi Ito, Dr. Sadaki Samitsu, Dr. Izumi Ichinose, Dr. Edhuan Bin Ismail, Dr. Takanobu Hiroto, Dr. Thi Kim Ngan Nguyen, Dr. Hideo Okuyama, Dr. Tohru S. Suzuki, and Professor Takamasa Ishigaki (Hosei University).
I would like to thank the secretary, Ms. Yoko Watanabe, for supporting my student life at NIMS.
I am grateful to the collaborators of the Laboratory for Innovative Key Materials and Structures, Dr. David Berthebaud, and Dr. Jean-François Halet for their helpful discussions.

I would like to also acknowledge Dr. Dalal Asker, Dr. Tarek S. Awad and Professor Benjamin D. Hatton for their warm welcome to the University of Toronto and their great help with my experiments.

Finally, I would like to give the biggest thanks go to my family for their understanding and support.

Masako Uematsu

Contents

Chapter 1| Introduction

1.1 Classification of pores and application of porous materials

1.1.1 Classification of pores

Porous materials are classified into three grades depending on their pore diameter d: micropore (d < 2 nm), mesopore (2 nm < d < 50 nm) and macropore (d > 50 nm), according to IUPAC[1]. In addition, pores with the size of less than100 nm are defined as 'nanopores' in the IUPAC report, however, it should be noted that pores of less than 5 nm size are often called 'nanopores' in the field of gas adsorption measurement[2]. In this study, the discussion of pore size uses the terms micropore, mesopore, and macropore according to the IUPAC definitions.

There is also a classification from the view point of practical applications. For example, in the field of fluid filtration, there are categories, such as nanofiltration / reverse osmosis (d < 1 nm), ultrafiltration (1nm < d < 100 nm), microfiltration (100nm < d < 10 μm), and filtration (d > 10μm) based on the size of the particles to be removed and the mesh size of the filter[3-5]. A rough range of pore diameter d is shown here, however, the classification of filtration systems is still ambiguous[6], and there are differences in the criteria depending on the literature. Documents are confirmed that set the boundary between nanofiltration and ultrafiltration at 2 nm, and the boundary between ultrafiltration and microfiltration at 50 nm[7, 8]. Figure 1.1 shows the pore size classification according to the IUPAC and the filtration categories with the rough pore size criteria. Although the divisions of filtration are not exact, it is practical to estimate the size of material separated by the filter.

Pores can also be classified by their shape[9, 10]. Figure 1.2 is a schematic illustration of the pore morphology with reference to the IUPAC literature[11].

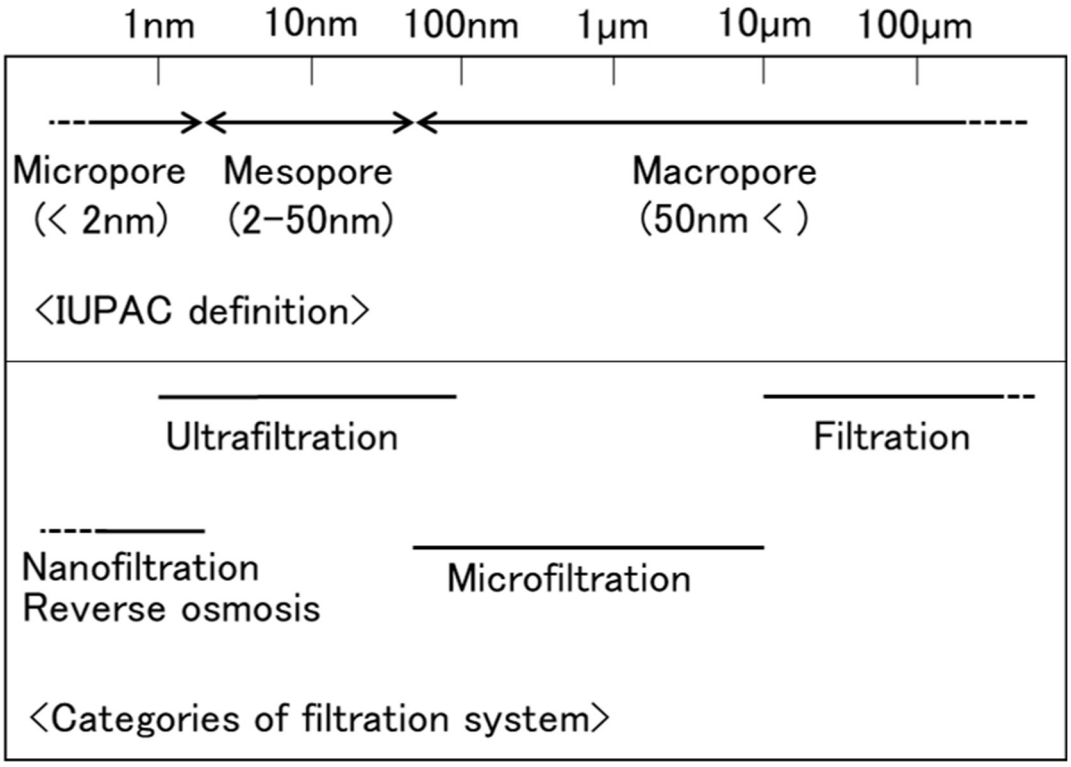

Figure 1.1. Pore size classification according to the IUPAC and the filtration categories with the pore size criteria

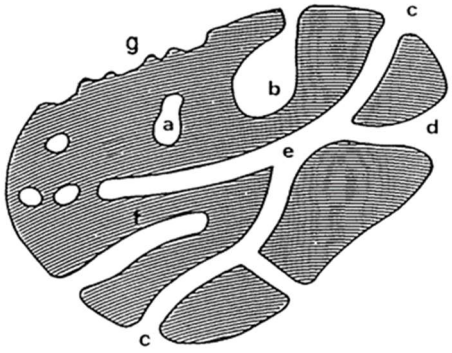

Figure 1.2. Classification of pores according to their morphology modified from [11])
(a)Closed pore, (b)Bottleneck-shape blind pore, (c) Cylindrical connected pore,
(d) Funnel-shape connected pore, (e) Open at two ends (through) pore,
(f) Cylindrical blind pore, (g) Pore or surface roughness

First, the distinction between an open pore and closed pore is very important. Closed pores, shown in Figure 1.2(a), are isolated from the surrounding environment and inert to fluid flow and adsorption processes. Closed pores are desirable for a thermal insulation porous body because they reduce heat transfer associated with mass transfer, and are also acceptable as a function of weight reduction and applications where continuity of the matrix is required such as heater materials and electrodes.

On the other hand, Figure 1.2(b)-(f) are open pores which have a continuous channel of communication with the external surface of the body. The pores like (b) and (f) with one entrance and one end, are described as blind pores, and (e) is open at two ends (through), connected, or networked pores. Pores with a constant width are called cylindrical pores either open (c) or blind (f), and that with non-constant widths (b) and (d) are called bottleneck-shape and funnel-shape, respectively. A simple convention for distinguishing whether (g) is pore or surface roughness is to consider a surface hole deeper than its width as a pore. Blind pores are not suitable for filtration applications, but are acceptable for adsorption.

The pore shape is also related to the characterization method. The mercury porosimetry method described in Section 1.4.3 assumes a cylindrical open pore, and gas adsorption measurement may assume the pore shape to estimate the pore size distribution.

The pore size and pore shape of the porous material are selected according to the application.

1.1.2 Application of macroporous ceramics

Porous materials are used in many fields such as chemical synthesis, environment, energy, optics, medicine, and electronics [3, 10, 12-14]. Porous ceramics bulk bodies have the advantage that the intrinsic properties of the ceramic, such as heat resistance, corrosion resistance, high strength, low density, biocompatibility, heat transfer properties, and electromagnetic properties, can be combined with those of distributed pores within the matrix. The properties of porous materials include, for example, gas and liquid permeability, adsorption properties, catalytic performance, low thermal conductivity, high electrical resistivity, thermal shock resistance, and light weight. Some examples of practical applications related to the materials or applications dealt with in this study and other possible applications are briefly introduced in this section.

One of the examples of applications is automobile exhaust gas filters[3, 15, 16]. Exhaust gas from diesel engine vehicles contains particulate matter (PM), which consists of aggregates of carbon fine particles, soluble organic fraction, oxygen-containing organic compounds, and sulfate particles. A porous ceramic filter called a diesel particulate filter (DPF) is used to remove the PM from the gas. The DPF employs a structure called a wall-through filter[17], in which the exhaust gas passes through the walls of porous ceramics with a honeycomb structure. Figure 1.3 shows the commercial DPF filters and sectional view of the wall-through monolith, the representative structure of the DPF. The PM is trapped in the pores and walls of the ceramics. Fine particles accumulated in the DPF are removed by oxidation. Therefore, many DPFs are coated with an oxidation catalyst containing Pt or Pd. Cordierite and SiC are often used as the materials for the DPF.

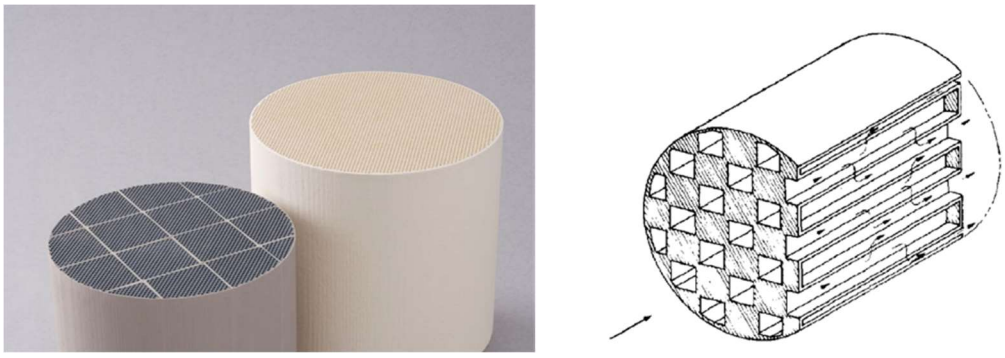

Figure 1.3. Commercial DPF filters and sectional view of the wall-through monolith (modified from [17, 19])

Exhaust gases from automobiles contain not only PM, but also CO, NO_x, and unburned hydrocarbons (HC)[18]. These emissions are regulated by law in Japan, Europe, and the United States. Under regulations that have become increasingly strict in recent years, it is difficult for one filter unit to deal with all the discharged substances. For this reason, multiple filters are used in combination, effectively utilizing the controlled pore structure of the porous body and the structure of the catalyst-carrying ceramics. Zeolite catalysts have been put into practical use for decomposing nitrogen oxides (NO_x) contained in automobile exhaust gases. Zeolite catalysts are also described later in Section 1.2. Ceramic porous bodies having a high specific surface area are often used as catalysts, catalyst carriers, and adsorbents, thus not limited to exhaust gas treatment.

Porous ceramics are also used as water purification filters. Various ceramic filters have been proposed to remove bacteria and harmful chemicals from drinking water. For example, there are pot-type filters for easily obtaining clean water at a low cost and tubular filters for precise filtration[20-22]. Figure 1.4 shows a photograph of a commercially-available tubular ceramic water purification membrane and module.

Ceramic filters are more durable than organic hollow fibers and can be recycled for use, and are expected to serve as point of use (PoU) filters to supply safe water in developing countries.

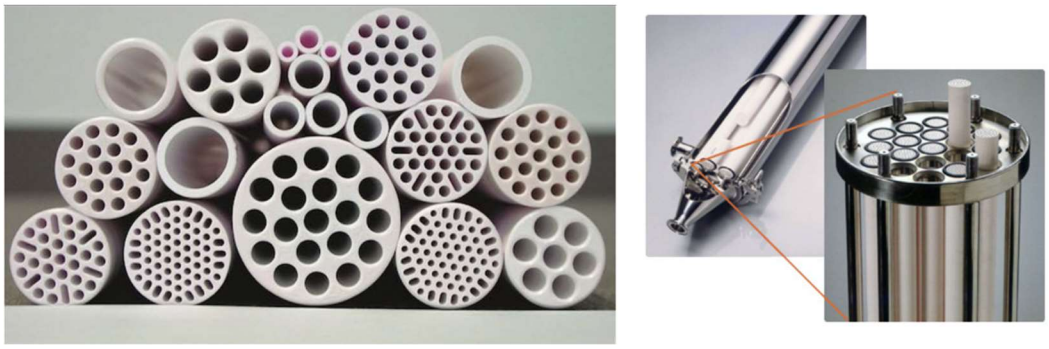

Figure 1.4. Photograph of commercially-available tubular ceramic water purification membranes and a module (modified from [23] [24])

In the field of biomaterials, open porous ceramics with an excellent biocompatibility are used as bioimplants for bone regeneration. For example, hydroxyapatite is the main component of human teeth and bones, has a high biocompatibility, and has long been studied as artificial bone[25-27]. Figure 1.5 shows an example of the appearance of the HAp artificial bone products and the microstructure of the artificial bone (85% porosity)[28]. Porous materials used as biomaterials often have pores on the order of 100 μm, matching the size of cells[29]. Porous ceramics, which have an excellent chemical stability and a structure suitable for biochemical reactions, are also used as bioreactors.

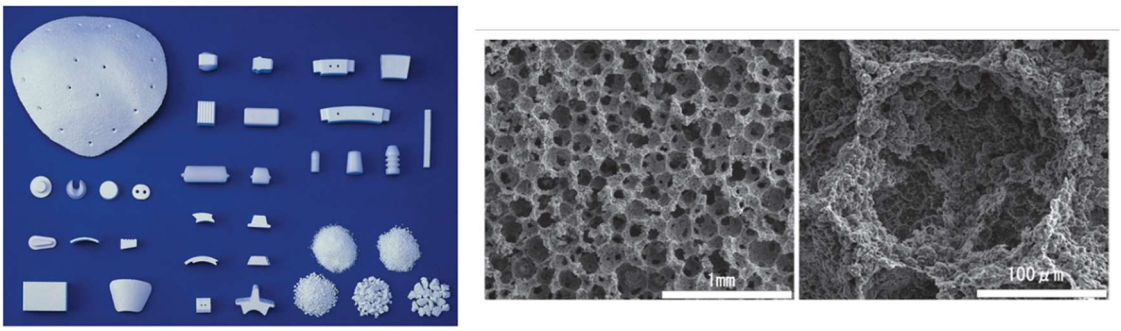

Figure 1.5. Example of the appearance of the HAp artificial bone products and the microstructure of the artificial bone (85% porosity) (modified from [28])

Other typical applications of ceramic porous bodies include refractories and heaters. Porous ceramics have been used as refractories in various industrial furnaces due to their low thermal conductivity and high thermal shock damage resistance. On the other hand, electrically-conductive porous ceramics, such as silicon carbide, are also applied to heaters and heat exchangers due to their heat resistance and fluid permeability.

In electrochemical devices, such as gas sensors, fuel cells, and transducers, porous ceramics are often incorporated as key parts, such as electrodes, taking advantage of their porous structure for fluid permeability, large reaction area, and unique electromagnetic functions.

The applications of ceramic porous bodies are wide-ranging as introduced. The control and characterization of the pore structure, which significantly affects the properties, is very important in any application.

1.1.3 Application of microporous and mesoporous materials

Microporous and mesoporous materials are used as adsorbents, materials for separation, catalysts and support materials in various fields such as the environment, chemical industry, biology, medicine, and agriculture [30].

Activated carbon is a material that has been used for a very long time. It has been widely used as an adsorbent because it has a high specific surface area and can be manufactured at a low cost [10].

Zeolite is a representative microporous material and the most widely used catalyst in industry. It has been utilized in the form of a powder, molded pellets, or membrane[31-35] due to its uniform-sized micropores and surface performance as a solid acid. The pores of most zeolites are less than 1 nm [36], thus it is difficult to react large molecules inside or support nanoparticles. The structure and properties of the zeolite crystal are described in detail in Section 1.2. Efforts to expand the pore size of zeolites[30, 37-39] and search for new mesoporous materials have been made. Mesoporous silica, such as MCM-41 and FSM-16 developed in 1990s, synthesized using surfactant templates is well known as a mesoporous material[40-42]. However, mesoporous silica cannot be expected to have a catalytic function because the pore walls are amorphous silica with a poor reactivity[43]. Attempts have been made to introduce catalytic metal oxides into the silica frameworks[44-47], and the synthesis of mesoporous materials with a transition metal oxide skeleton[48, 49] to improve the reactivity of the mesoporous material.

Porous coordination polymers (PCPs) and metal-organic frameworks (MOFs) are porous materials that have attracted attention due to their flexibility in pore size design and simple synthesis processes[50]. PCPs and MOFs are generally produced in a powder form by a hydrothermal synthesis.

Microporous and mesoporous materials, such as zeolites, mesoporous silica, and MOFs, are obtained as synthesized powders. The fine powder materials are often difficult to use in industry without changing the form, thus scale-up of the structures is required. Figure 1.6 shows the typical sequence of interactive tasks followed in a catalyst development program for the material, such as zeolites, and Figure 1.7 shows the commonly applied components in the catalyst formulation[34]. Additives incorporated to facilitate the shaping or to enhance the properties of technical catalysts change the composition, structure, porosity, and performance with respect to research catalysts. Scale-up is an important issue in the successful implementation of new materials. Research that introduces higher-order structures and expresses functions when scaling-up microporous and mesoporous materials has the potential for future progress.

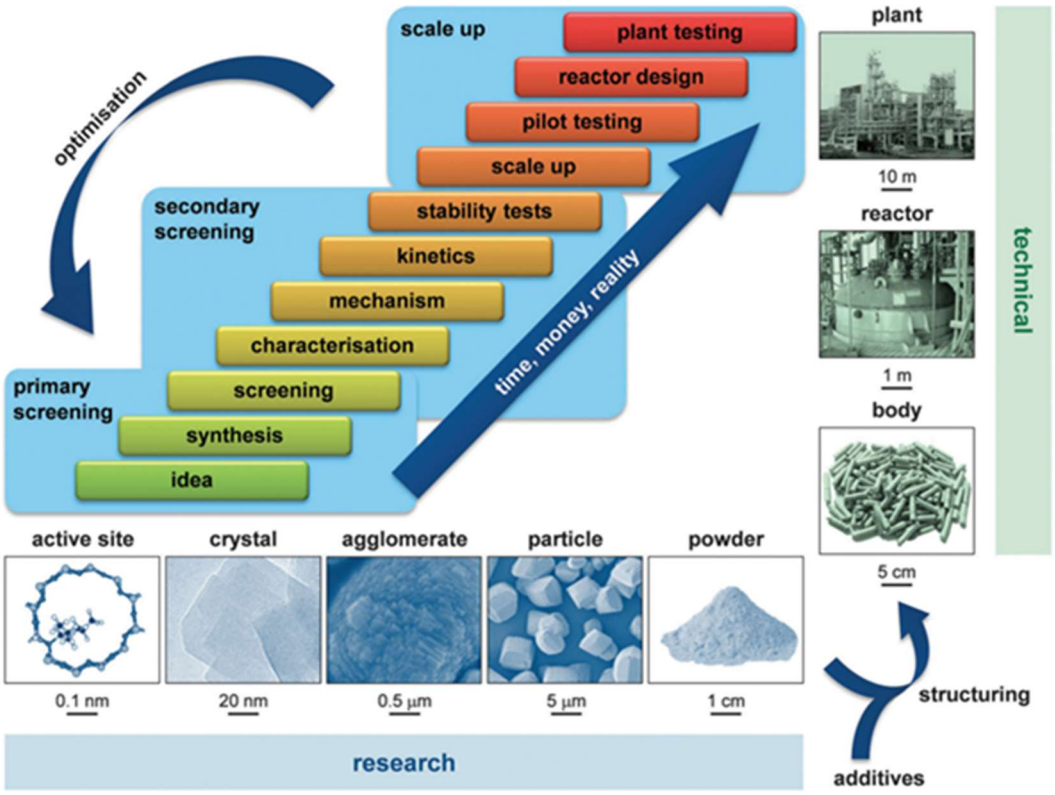

Figure 1.6. Typical sequence of interactive tasks followed in a catalyst development program [34]

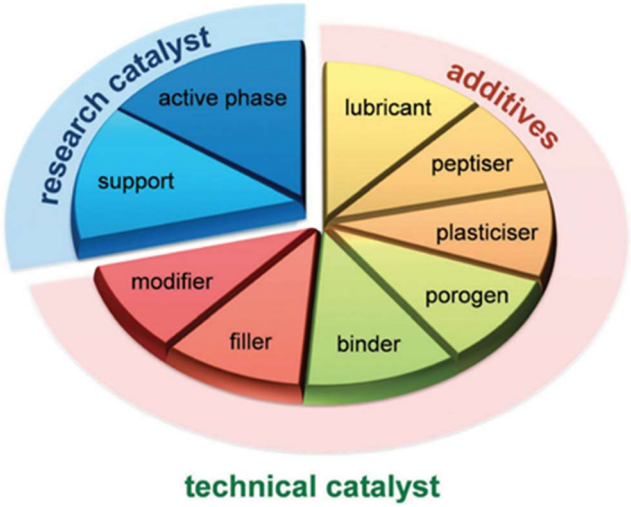

Figure 1.7. Commonly applied components in catalyst formulation[34]

1.1.4 Designing of pore structure

Attempts have been made to combine microporous materials and mesoporous materials that have the ability as molecular sieves or adsorbents with larger-scale structures to apply their functions. For example, a monolithic ceramic made from silica gel has been put to practical use as a column for liquid chromatography[51]. It has a structure that combines the mesopores of silica gel and macropores of the monolith. According to a report, the monolith with smaller macropores and higher porosity became a more efficient column. Figure 1.8 shows the microstructure of the reported material.

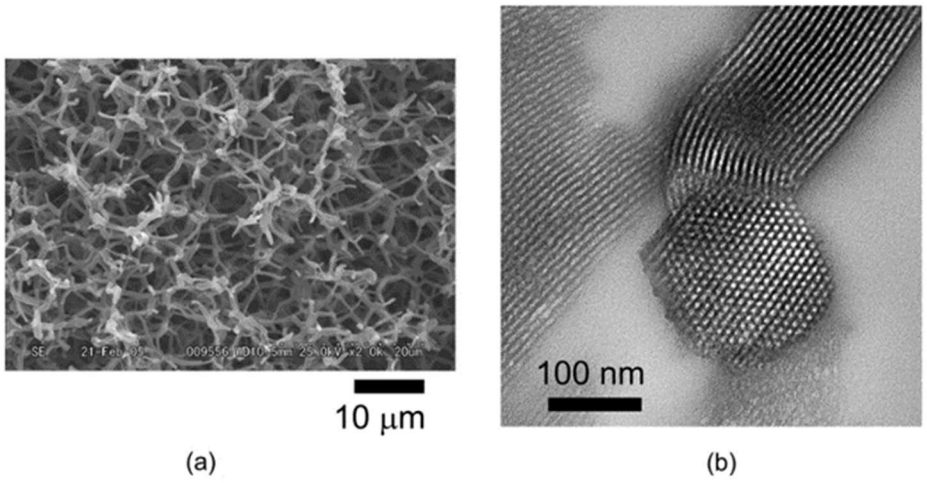

Figure 1.8. Structure of a monolithic silica gel with highly ordered two-dimensional hexagonal mesopores (a) SEM image, (b) TEM image (modified from [51])

Another example is zeolite membranes that have been developed as a gas separation filter[52-56]. Membranes of various types of zeolites such as FAU, MFI, and DDR, have been synthesized for the separation of hydrocarbon gases and CO_2. The development and commercialization of the DDR-type zeolite membranes for carbon dioxide separation (Figure 1.9) [57] and zeolite membranes for dehydration from bioethanol[58-60] are being promoted as carbon-neutral technologies that are of significant interest in recent

years. These materials have a structure in which the surface of a ceramic macroporous support is covered with a zeolite membrane.

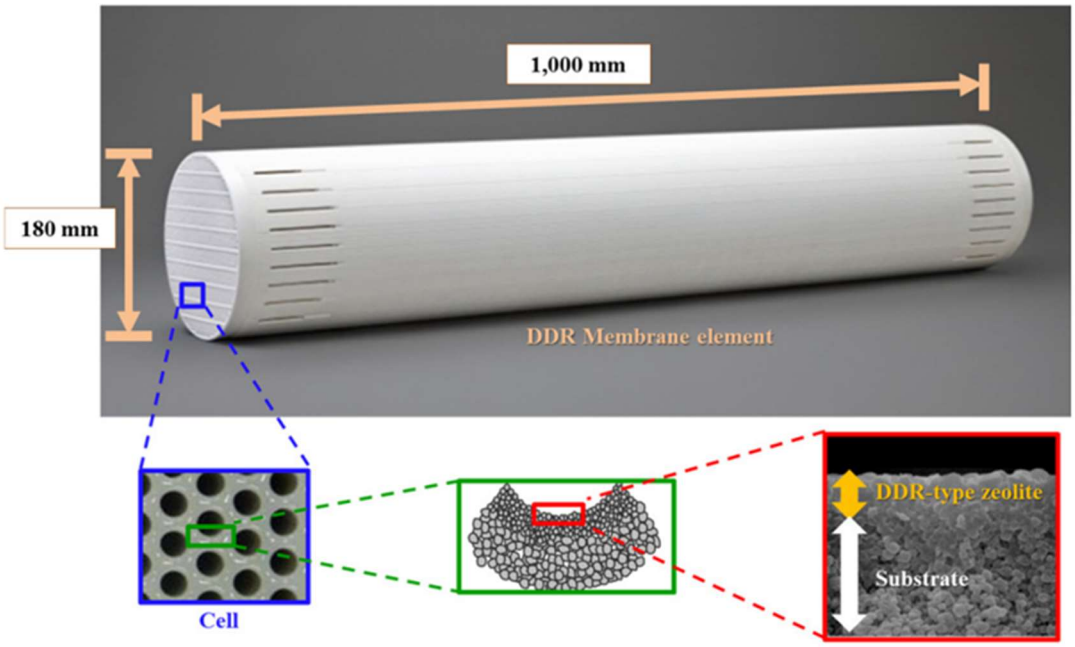

Figure 1.9. DDR-type zeolite membranes for carbon dioxide separation [57]

In this research, I aim to develop functions by controlling the higher-order structures that combine the functionality of fine structures in different scales. Zeolite, which is a microporous material, was chosen as the first material of interest. Fabrication of the zeolite bulk body by sintering is difficult as it decomposes at high temperatures. Ceramics bulk bodies with micropores, mesopores, and macropores are fabricated using a zeolite with a highly-reactive surface as a material, and the bulk functions are characterized. The functionality of the zeolites is described in Section 1.2.

As a second material of interest, hydroxyapatite, was selected. Hydroxyapatite (HAp), with the chemical formula $Ca_5(PO_4)_3OH$, is considered the structural template for the mineral phase of bone, dentin and enamel. HAp has been used for artificial bones and artificial tooth roots (implant materials) as a biomaterial with an excellent biocompatibility. HAp also exhibits many functions, such as ion exchange properties, ion adsorption properties, catalytic properties, and ion conduction properties.

Figure 1.10 shows the crystal structure of hydroxyapatite[61-63]. HAp typically has a hexagonal crystal structure with a $P6_3/m$ space group, and its crystal unitcell is characterized as $a=b$=0.942 nm, c=0.688 nm, $\alpha = \beta = 90°$, γ=120°.There are two major crystal planes, which are the *a(b)*-plane (*ac* and *bc* crystal faces) and the *c*-plane (*ab* crystal face). The *a(b)*-plane is rich in calcium ions and positively charged, while the *c*-plane is rich in phosphate and hydroxide ions and negatively charged[64].

Single-crystal HAp particles with two types of anisotropy were synthesized by Aizawa et al. The *a(b)*- and *c*-planes exhibit anisotropic characteristics, such as resolvability, biocompatibility, and adsorptive activity.

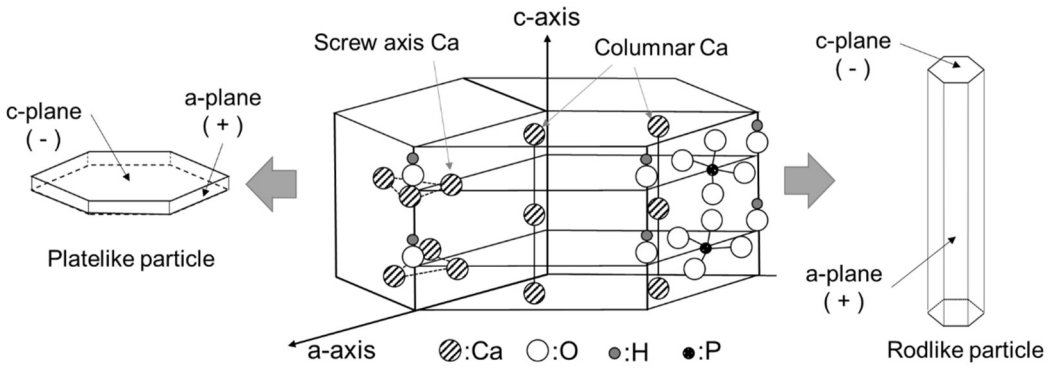

Figure 1.10. Crystal structure of hydroxyapatite

By using HAp crystals with a significantly exposed *a*-plane as a filter, viruses of which their surface is mainly negatively charged [65, 66], can be removed with a high efficiency by utilizing electrostatic attraction. In addition, HAp is a biomaterial ceramic that is quite safe for the human body and can be reused by heat treatment. In this study, fabrication of the HAp porous body with a positively charged *a*-plane exposure and continuous pore structure was attempted. To expose the positive sites, rodlike HAp particles, which have a large *a*-plane surface area, were used as the raw materials.

HAp has a significant potential as a material for filter applications. In this study, the filter application that combines the microstructure and macroporous structure of HAp was investigated. Methods for controlling the macroporous structure is introduced in Section 1.3, and characterization of the pore structure are described in Section 1.4.

1.2 Microstructure and synthesis method of zeolite

1.2.1 Microstructure of zeolite

Zeolites are crystalline aluminosilicates and are microporous materials known as molecular sieves[10, 16, 30, 67]. The primary building unit of zeolite is a tetrahedral structure of SiO_4 or AlO_4, which are collectively written as TO_4. The TO_4 tetrahedra are linked by sharing O as shown in Figure 1.11 to form a three-dimensional framework. A silicate having the chemical composition of SiO_2 is electrically neutral, but an aluminosilicate in which a part of Si^{4+} is replaced with Al^{3+} become electrically negative. The cations involved in the zeolite structure compensate for the negative charge of the aluminosilicate framework.

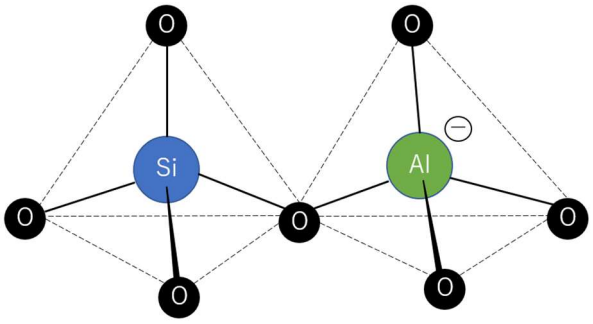

Figure 1.11. Tetrahedral basic unit of zeolite

The chemical composition of zeolite is represented by formula1, where M^{I} and M^{II} are monovalent and divalent cations, respectively [68].

$$(M^{I}, M^{II}_{1/2})_m (Al_m Si_n O_{2(m+n)}) \cdot x H_2O, (n \geqq m) \quad \text{—formura1}$$

M^{I}: Li^+, Na^+, K^+, Tl^+ etc.. M^{II}: Mg^{2+}, Ca^{2+}, Sr^{2+}, Ba^{2+} etc..

The M^{I} and M^{II} cations and H_2O are confined in cages or channels within the zeolite structure and do not participate in the framework.

Since zeolite containing water of crystallization is stable, dehydrated zeolite is available as a strong adsorbent for water. When hydrogen ion binds to electrically negative oxygen, Brønsted acid sites are generated. Brønsted acid sites changes to Lewis acid sites by heat dehydration, and Lewis acid sites changes to Brønsted acid sites upon hydration as shown in Figure 1.12. Zeolites are widely used as catalysts due to their solid acid property.

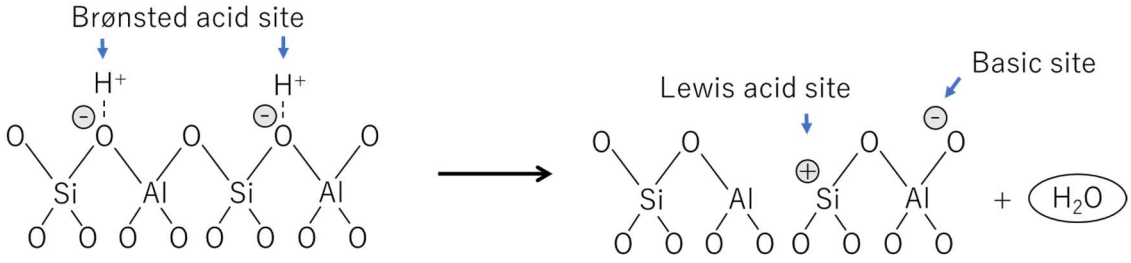

Figure 1.12. Acid site of zeolite

The zeolite crystalline structure has many variations due to the geometric bonding of the TO_4 tetrahedra, called the framework. Zeolites are classified according to the framework that is given the code name of FTC (Framework Type Code) consisting of three capital letters that is approved and organized in a database by the Structure Commission of the International Zeolite Association (IZA-SC)[36, 69]. However, zeolites with disordered framework structures were difficult to describe by FTC, which assumes a completely ordered structure in three dimensions. Therefore, a second database was proposed by the IZA Structure Commission in June 2022 to classify zeolites with disordered structures as Intergrowth Families, separate from zeolites with FTC codes. According to the IZA-SC database, 248 types of zeolites with FTC and 40 Intergrowth

Families have been reported as of January 2023. However, there are only about 12 types of zeolites that are currently industrially used [31]. Among them, the most frequently used zeolites for industry are only five types called the “Big five”, i.e., faujasite (FAU), mordenite (MOR), ferrierite (FER), ZSM-5 (MFI), and beta(BEA)[70]. Figure 1.13 shows the framework of the 'Big 5' zeolite and examples of representative materials with the framework. BEA zeolites marked with an asterisk are classified as beta in the new classification of the intergrowth family.

Framework Type Code	FAU	FER	MFI	MOR	*BEA (Beta)
Framework	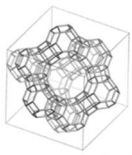 Viewed along [111]	 Viewed along [001]	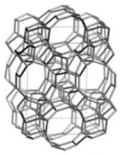 Viewed along [010]	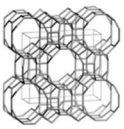 Viewed along [001]	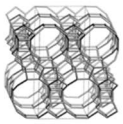 Viewed along [010]
Materials	Faujasite Zeolite X Zeolite Y	Ferrierite	ZSM-5 Silicalite	Mordenite	Beta

Figure 1.13. Framework of 'Big 5' zeolite and examples of representative materials with the framework (modified from [69])

The zeolite crystal structure contain micropores that are derived from their respective frameworks. A tubular pore is called a channel, and a cage-like pore is called a cavity. Zeolites exhibit a molecular sieving effect due to its pores which have the size on the order of a molecular scale. The IZA database presents the geometric structure data of zeolites, and the size of the channel that contributes to the material diffusion can be simply expressed by the maximum number of connecting tetrahedral atoms (T-atoms) and the size of the ring. In the Big 5, FER and MFI have 10-membered rings, and FAU, MOR, and Beta have 12-membered rings. Zeolites are conventionally classified by the

maximum number of T-rings. A zeolite with an 8-membered ring is called a small-pore zeolite, with a 10-membered ring is a medium pore zeolite, with a 12-membered ring is a large pore size zeolite, and with over a 14-membered ring is an extra-large pore zeolite. The current largest ring is the 30-membered ring of the ITQ-37 mesoporous chiral zeolite, known as an extra-large pore zeolite[36, 71].

Quantitative information on the size of channel systems is also provided by calculations on the diameter of the largest possible included sphere. These diameter data indicate the pore size of the largest sphere that can be included inside the structure. In addition, the sizes of the spheres that can diffuse along the a-b-c axes through the idealized channel are also labeled as the max diameter of a sphere that can diffuse. The maximum value of the largest possible included sphere is 1.645nm for the TSC type zeolite, and that of the maximum sphere that can be diffused is 1.212 nm indicated by ITQ-44, the IRR type zeolite. However, it should be noted that these data are theoretical calculations involving ideal crystals and some assumptions.

1.2.2 Properties of zeolite

Zeolites are widely used in adsorbents, industrial catalysts (solid acid catalysts), builders (detergent), desiccants, ion exchangers, wastewater treatment, fertilizers, and feed additives[68].

Due to the microporous structure, a phenomenon occurs in which the molecules that enter the pores are adsorbed and stay inside the pores. The adsorption characteristics vary depending on the type of zeolite. Factors that affect the adsorption properties of zeolites include the pore structure (dimensions, number of ring members, shape), pore size controlled by ion exchange and chemical reaction, hydrophilicity controlled by the Si/Al ratio, the polarity of adsorbents, size and shape of the adsorbed molecules, and diffusion coefficient changing with the temperature[68].

As catalysts, zeolites indicate three types of shapes selectivity depending on their micropore structure as follows: (a) Reactant shape selectivity: molecules that are too large to enter the zeolite pores cannot reach the acid sites for reaction and are therefore not converted into products. (b) Transition state shape selectivity: molecules (and transition states) that are too large to fit inside a pore do not form. (c) Product shape selectivity: new molecules are formed in the adsorbed phase but are too large to desorb as products[16].

Zeolite functions as a catalyst carrier for supporting metal ions that reduces and decomposes NOx are mentioned in Section 1.1.2. Three-way catalysts, which decompose and remove carbon monoxide (CO), unburned hydrocarbon (HC), and nitrogen oxides (NOx), are widely used for automobile exhaust gas treatment [16]. A three-way catalyst generally has a structure in which the main catalyst, such as Rh, Pt, and Pd, and a co-catalyst, such as CeO_2, are supported on a honeycomb monolithic carrier made of

ceramics such as alumina. Exhaust gas contains oxygen. When there is an excess of oxygen, the reduction of NOx is insufficient, while on the other hand, when there is a limited supply of oxygen, the removal of CO and HC is incomplete. By controlling the amount of fuel injected according to the amount of air, complete treatment is achieved, but the conventional three-way catalyst has the weakness of imperfect treatment of NOx when oxygen is excessively supplied. Cu-ZSM-5, which supports copper ions by ion exchange, was proposed as a reduction catalyst to solve this problem[72]. This catalyst was not put to practical use because its activity decreased in the presence of water, but later catalysts were developed in which various ions were supported on ZSM-5. For example, the Ir-Pt/MFI catalyst has been put into practical use.

As already mentioned, the pore size of currently known zeolites is limited to less than 2 nm, which limits the size of substances that can be supported. Metal ions can be supported by zeolites in terms of size, but functional nanoparticles of several nanometers in size, which have been studied in recent years, cannot be supported. Applications of zeolites are being further expanded by increasing the types of supported substances.

1.2.3 Synthesis method

Zeolites also exist as natural aluminosilicates, but in industrial applications, they are commonly artificially synthesized by a hydrothermal synthesis (HTS)[67, 73]. For the hydrothermal synthesis of zeolites, organic structure directing agents (OSDA) are used to control the microstructure of the zeolite and silica/alumina ratio[74, 75]. OSDA is also called a template. Processes with various OSDAs have been proposed to synthesize novel zeolites.

Figure 1.14 shows a typical hydrothermal synthesis (HTS) method of a zeolite[73, 76]. First, amorphous reactants containing silica and alumina with a cation source, OSDA and water are mixed to prepare a basic (high pH) aqueous precursor. The precursor is then heated in a sealed autoclave. The T atom sources maintain their amorphous structure in the precursor just after the heating starts, but the zeolite crystals are gradually synthesized through the steps of an 'induction period', 'nucleation' and 'crystal growth'[73, 77]. The synthesis temperature and time period depend on the type of zeolite and synthesis process. The synthesis is typically carried out at 100-200°C for several hours to several days, but in recent years, a method of synthesizing in a short time by applying a high temperature has been reported[78-80]. The synthesized zeolites are generally obtained as crystalline powders, collected after filtration, washing, and drying. OSDA-free synthesis methods have also been investigated in which zeolite seeds are added to the precursor[81-84].

Seed crystals of zeolite are also used in the secondary growth method that is a general process to synthesize zeolite membranes. In this method, seed crystals are evenly attached to the surface of the substrate, then grown into a membrane by a

hydrothermal synthesis. For various zeolites, the attaching and synthesizing process of the seed crystals have been investigated[85-87].

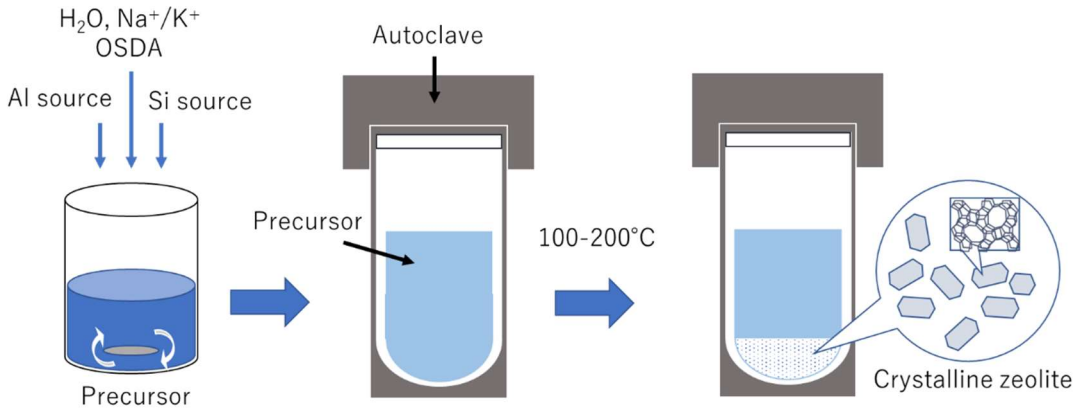

Figure 1.14. Hydrothermal synthesis (HTS) method of zeolite

A solid-phase reaction process called the dry-gel conversion (DGC) is also known as one of the synthesis methods of zeolites. It has been reported by Xu et al. in 1990 that a dry aluminosilicate gel could be transformed to an MFI by contact with the vapors of water in an autoclave[88]. It was a process in which the dried precursor gel is converted to a zeolite in a steam of water or an organic solvent at high temperature and pressure. DGC comes in two variations; i.e., vapor-phase transport (VPT) and steam assisted conversion (SAC)[89, 90]. The two differ in whether OSDA is included in the precursor gel or in the reaction vapor.

Figure 1.15 shows two DGC methods; i.e., vapor-phase transport (VPT) and steam-assisted conversion (SAC). It is reported that MFI, FER, and MOR zeolites synthesized by the VPT method have different compositions from zeolites synthesized by the conventional HTS method, and the ratio of Na to the SiO_2/Al_2O_3 ratio is low. Moreover,

in the SAC method, the synthesis reaction, which normally takes several days, was completed in several hours [90]. In recent years, a method has also been proposed for the rapid synthesis of zeolites by only heating a solid gel in an autoclave without using a solvent[91]. The advantages of the DGC method are that it synthesizes zeolites with a composition that cannot be obtained by the ordinary HTS process, and that it uses less solvent.

Attempts have also been made to fabricate mesoporous material and zeolite composites by applying SAC. Research has been conducted to synthesize zeolite-mesoporous composites by the SAC method using mesoporous silica SBA-15 as the raw material[92]. It has been reported that the meso-structure regularity is lost and collapsed as the long-range structure of the zeolites is formed, and the reaction proceeded faster when the Si/Al ratio was higher.

In the HTS method, zeolites were rapidly synthesized without OSDA by adding seed crystals, and in the DGC method, a high Si ratio facilitated conversion to the zeolite. Furthermore, the green body tends to retain its shape with DGC because it does not come into direct contact with the solution.

Based on this information, the DGC method was attempted to create a bulk zeolite in this study by treating the green body made of zeolite crystal powder and colloidal silica with a high-pressure water vapor. A surface reaction between the colloidal silica and zeolite has the possibility to produce a strong bulk body.

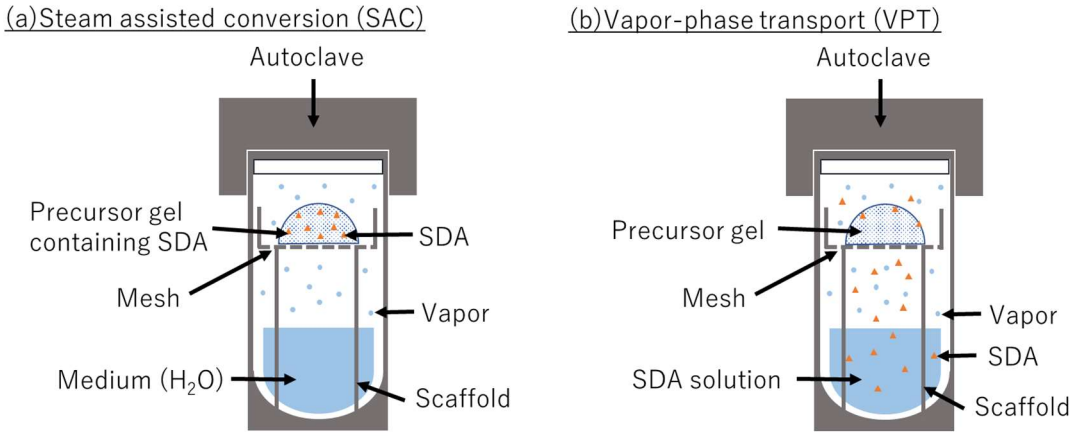

Figure 1.15. Dry gel conversion (DGC) method (a) Steam-assisted conversion (SAC), (b)Vapor-phase transport (VPT)

1.3 Processing technique for macroporous ceramics

1.3.1 General method

In this section, the major fabrication techniques for a porous ceramic body are introduced. Figure 1.16 shows representative fabrication processes for macroporous ceramics. The process of (a) partial sintering, (b) sacrificial fugitives, (c) replica templates, and (d) direct foaming [3, 13, 14, 93, 94] are described.

Partial sintering (Figure 1.16 (a)) is the simplest method to fabricate porous ceramics. This is a technique in which the sintering is interrupted after necking between particles is formed due to material diffusion on the surface leaving the spaces between the particles as pores. The pore size depends on the size of the raw material powder, and the porosity varies depending on the density of the compact, sintering conditions, and the addition of sintering additives. This method has an advantage that a porous body with a uniform structure can be easily obtained. However, it is difficult to produce ceramics with a porosity of more than 50% by this method.

Sacrificial fugitives (Figure 1.16 (b)) are also a widely used technique. In this method, a pore-forming agent is dispersed in the ceramic compact and removed by sublimation or combustion before or during sintering. The size, shape and amount of the pore-forming agent can be controlled to create a variety of structures.

The pore forming agents are generally classified into synthetic organic matters (polymer beads[93, 95-100], etc.), natural organic matters (starch[101-111], cellulose[112], etc.), inorganic matters (carbon[113, 114], fly ash[115, 116], glass particles[117], etc.), liquid (water[118-120], and emulsions[121], etc.).

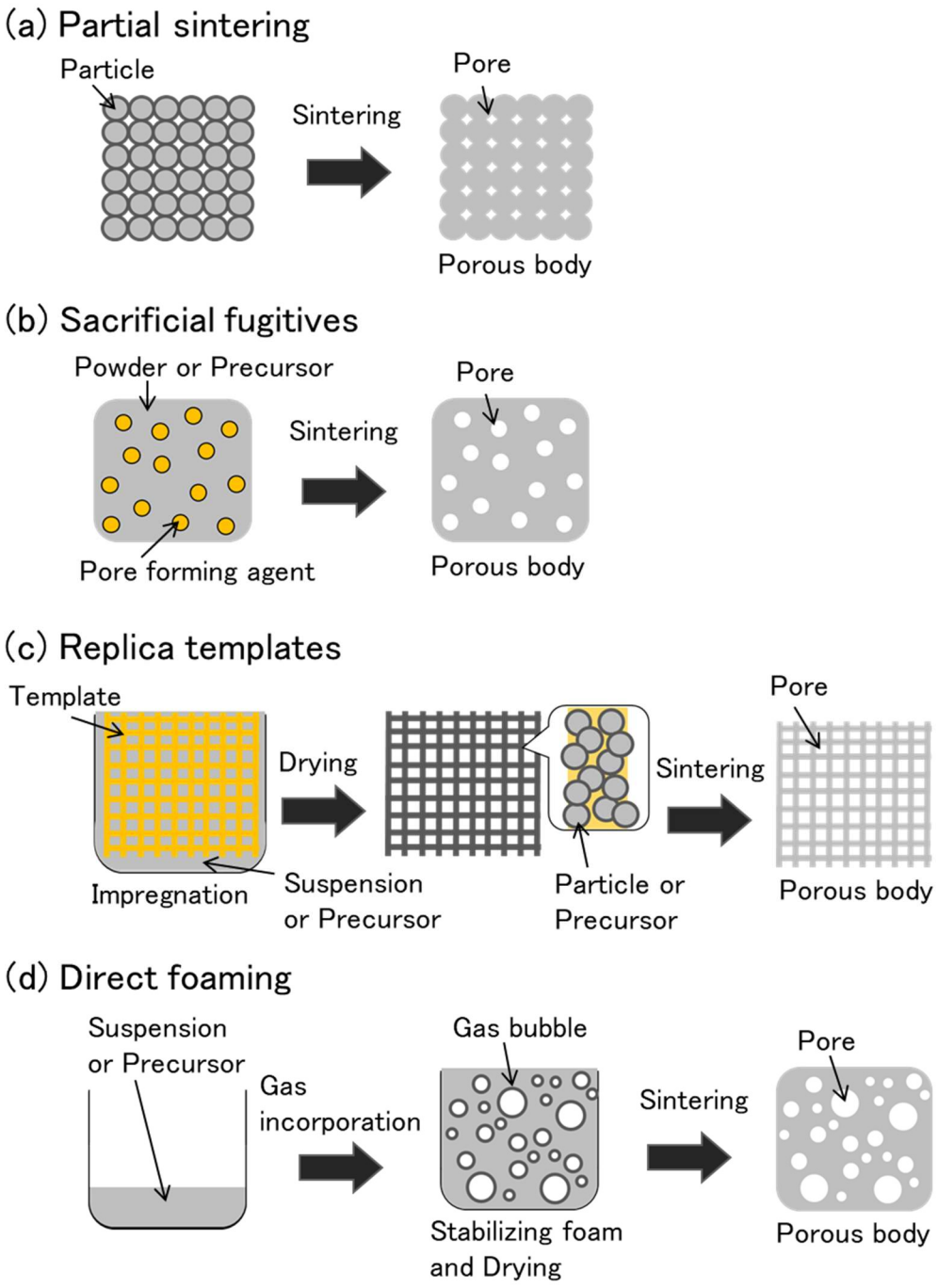

Figure 1.16. Representative fabrication processes for macroporous ceramics

Polymethyl methacrylate (PMMA) is one of the frequently used synthetic organic pore forming agents. Polymer beads create spherical pores that reflect the size and shape

of the pore forming agent[97]. The structure can be controlled by the amount of added beads, but the pores in the compact will be isolated if the pore forming agent particles do not contact with each other. Attempts were made to connect the polymer beads and create open pores by chemical treatment with acetone prior to adding the pore former to the slurry[99]. Particles of starch have also been used as a pore forming agent. A process called starch consolidation has been proposed in which starch is added to the slurry followed by heating[101, 102, 107-110]. This method is explained as a process in which the starch absorbs water, which causes the ceramic particles to encounter each other and harden the compact, showing spherical pores in the form of starch particles.

Figure 1.17 shows the microstructure of porous ceramics using PMMA and corn starch as the pore-forming agents, and the structure of the porous alumina by the starch consolidation technique[93, 110, 111].

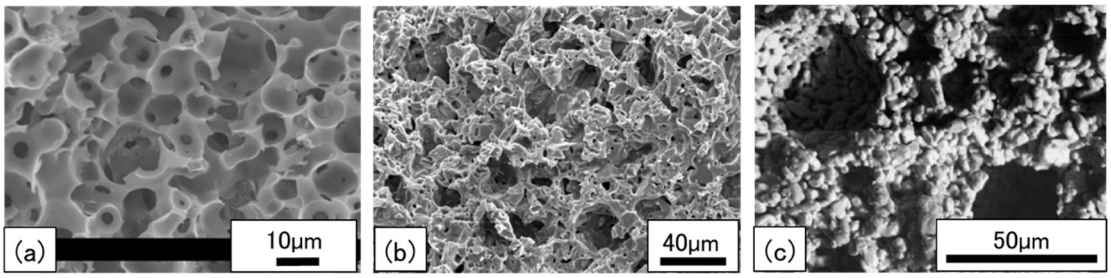

Figure 1.17. Microstructure of porous material fabricated by sacrificial template (a) a microcellular SiOC foam obtained by the burn-out of polymeric microbeads with 25-μm diameter (modified from [93]), (b) a porous SiC ceramics fabricated by adding 46wt% cornstarch with a diameter of 15-25μm (modified from [111]), (c) a porous alumina sintered at 1700°C after starch consolidation with 8wt% corn starch (no description of starch particle size, modified from [110])

The freeze-dry casting method reported by Fukushima et al. and Fukasawa et al. is considered as a kind of sacrificial fugitives[118-120]. The water-based suspension was frozen in one direction, and the ice is sublimed under reduced pressure before sintering. Porous bodies with honeycomb-like shapes and communicating pores in the freezing direction were obtained using this method. This is a method in which the structure changes depending on the freezing direction. Figure 1.18 shows the structure of the porous SiC obtained by the freeze-dry casting [120].

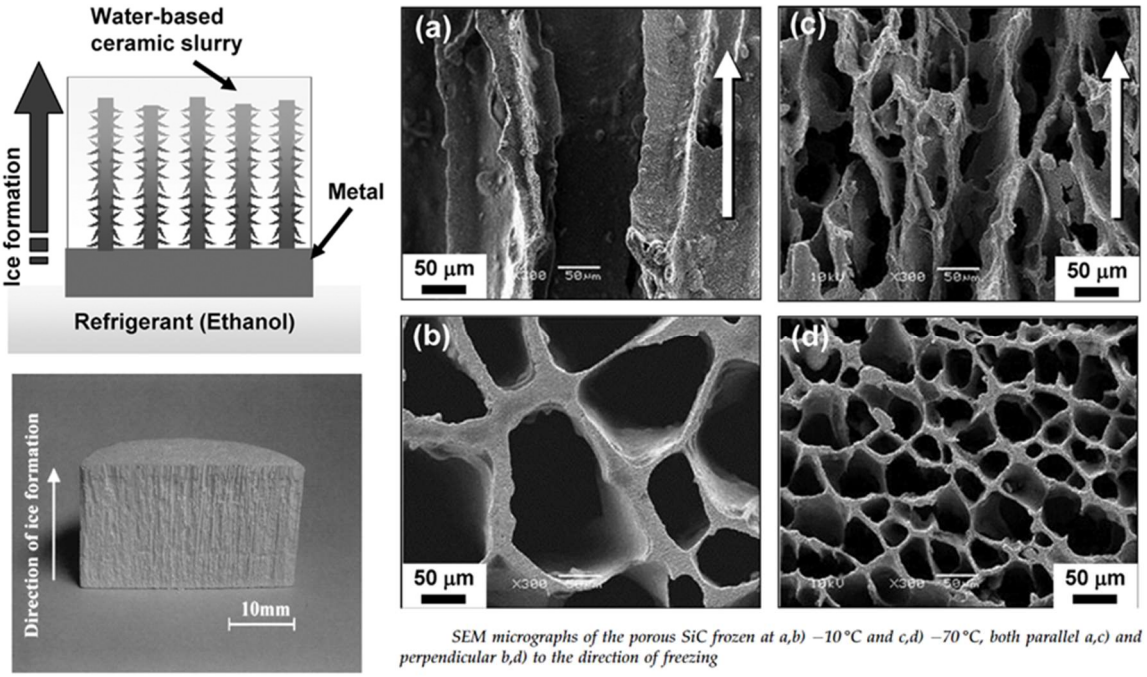

SEM micrographs of the porous SiC frozen at a,b) −10 °C and c,d) −70 °C, both parallel a,c) and perpendicular b,d) to the direction of freezing

Figure 1.18. Structure of the porous SiC obtained by the freeze-dry casting (modified from [120])

Replica templates (Figure 1.16 (c)) create very uniquely-shaped pores to reflect the shape of various replicas such as polyurethane foam, woods, and coral [122-125]. In this method, the porous structure template is impregnated with a ceramic slurry or precursor solution, then the template is removed by heat treatment after drying, and the remaining ceramic green is densified by sintering. Figure 1.19 and Figure 1.20 show examples of the pore structure of a porous body obtained by using the replica templates.

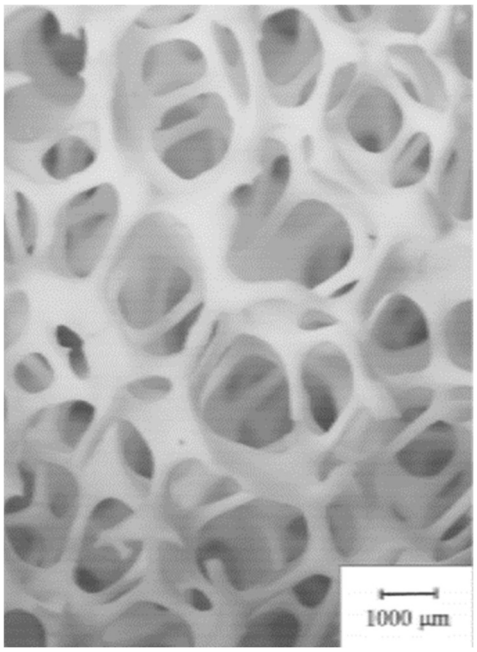

Figure 1.19. Cellular structures obtained by ceramic replication with polyurethane foam, alumina and colloidal silica (modified from[122])

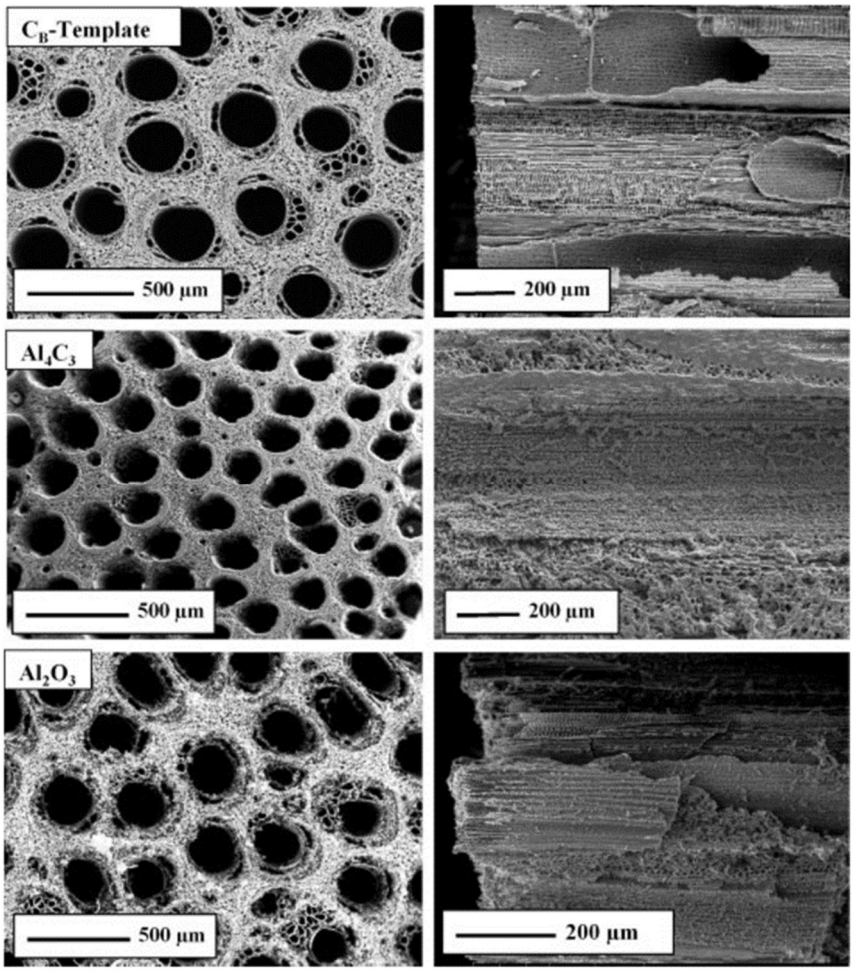

Figure 1.20. Scanning electron microscopy images of porous ceramics fabricated by replica template: pyrolyzed biocarbon template from rattan (C_B-template), the Al_4C_3 sample after aluminum-vapor infiltration at 1600 C for 1 h, and the biomorphic Al_2O_3 ceramic after sintering at 1600 C for 3 h in air. Left column: axial cut (perpendicular to the cell elongation); Right column: longitudinal cut (parallel to the cell elongation) (modified from [124])

Although there are few research examples, replica templates have also been applied to fabricate zeolite bulks. Zeolite is a material that is difficult to solidify by sintering, but it is possible to take on the challenge of depositing crystals on the surface of a template at a high density and removing the template to create a bulk. The fabrication of ZSM-5 zeolite monoliths by the replica template using polyurethane foam has been reported

[126]. It was a monolith foam having macropores with the size of 100-300 μm, and a self-standing structure is fabricated. Figure 1.21 shows the structure of the zeolite monolith prepared using a template of polyurethane foam.

Hierarchically-porous zeolites using diatom skeletons as templates have also been proposed[127]. An attempt was made to synthesize the MFI zeolite on the surface of a diatom skeleton with the size of 10 x 20 μm, and a unique structure was obtained. Figure 1.22 shows the morphology of the diatoms before and after growth of the MFI zeolite crystals.

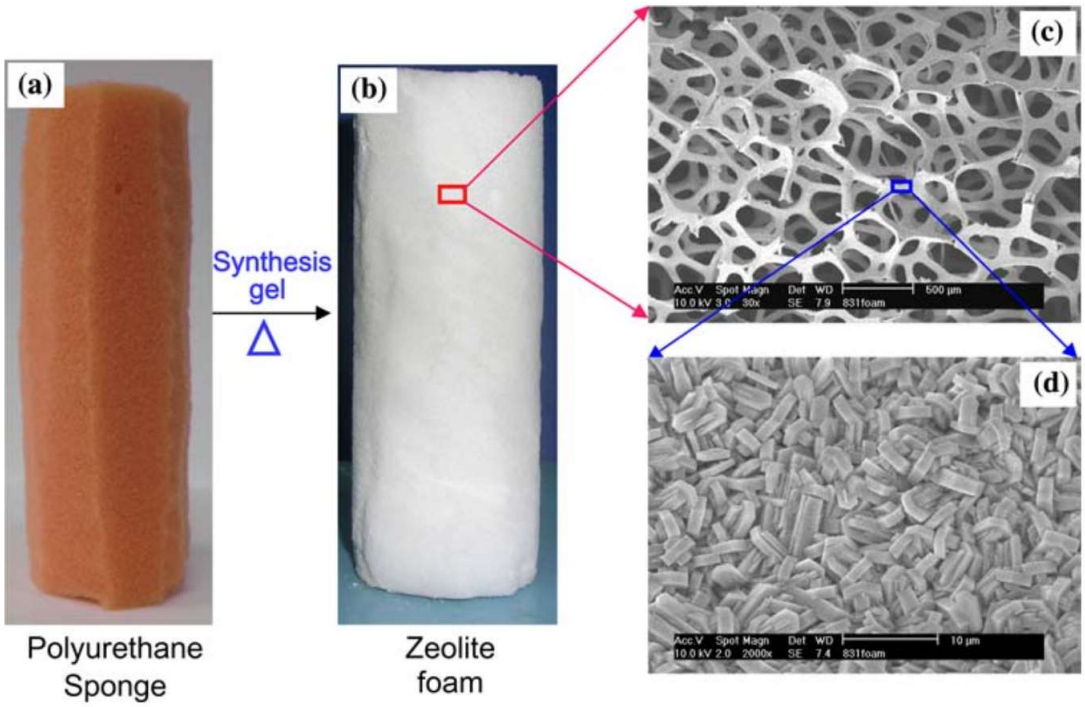

Figure 1.21. Morphology of ZSM-5 monolith foam, (a) photograph of polyurethane foam, (b) ZSM-5 monolith foam, (c) SEM images of ZSM-5 foam and (d) magnified portion of ZSM-5 foam (modified from [126])

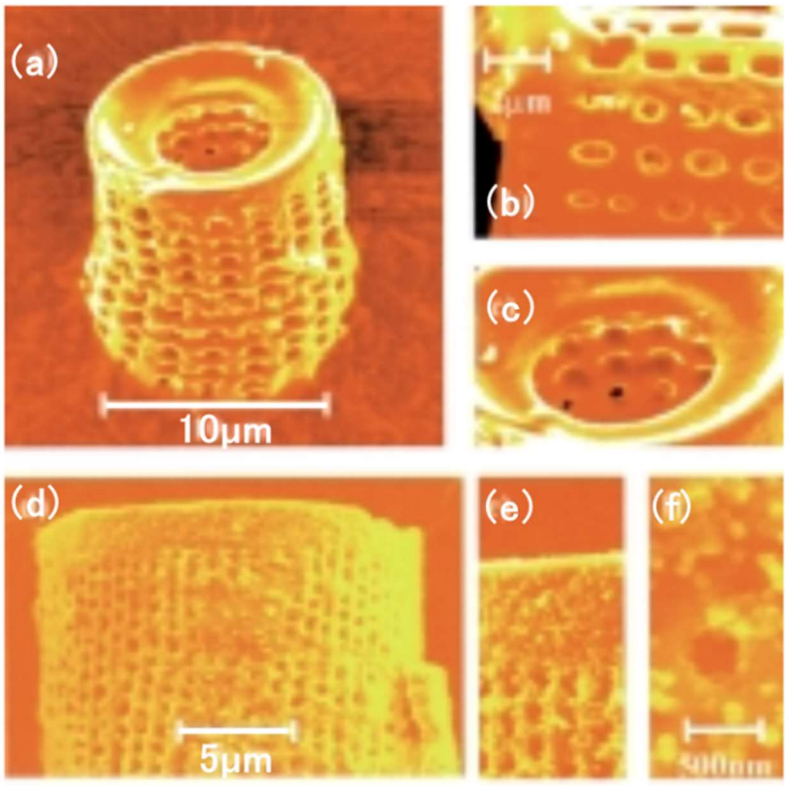

Figure 1.22. Morphology of the diatoms before and after growth of the MFI zeolite crystal, (a-c) The parent diatom with overall dimension of about 1020μm, (d- f) The diatoms after a 3-h hydrothermal growth (modified from [127])

Some attempts are being made to make zeolite bulks, even though the structure is different from the bulk body in this study. Direct foaming (Figure 1.16 (d)) is a method in which gas bubbles are introduced into a suspension or precursor, stabilized, dried, and sintered to obtain a porous body. Liquid foams are thermodynamically unstable systems due to their high gas–liquid interfacial area. Surfactants are used to stabilize fine bubbles in suspensions, and various formulations have been proposed [14]. In addition, it is desirable that the bubbles are difficult to move, as they rise in a suspension according to the Stokes equation. The forming method is suitable for producing porous bodies with a high porosity of about 45-97%[128]. As an example of the structure of

ceramics made by direct foaming, ZrC ceramics made by the carbothermal reduction of ZrO_2 and C are shown in Figure 1.23[129]. Water, methanol, n-pentane (blowing agent) and ammonia (curing agent) were used for the foaming. Regarding the shape of the air bubbles, spherical pores are formed by this method. Due to the high porosity and degassing during sintering, spaces are opened between the pores to create an interconnected structure. When the porosity is particularly high, a reticulate structure is formed by leaving the structure of the pore interface[129-131]. It is suitable for fabricating a continuous pore structure, but fabrication of a strong structure with low porosity is difficult.

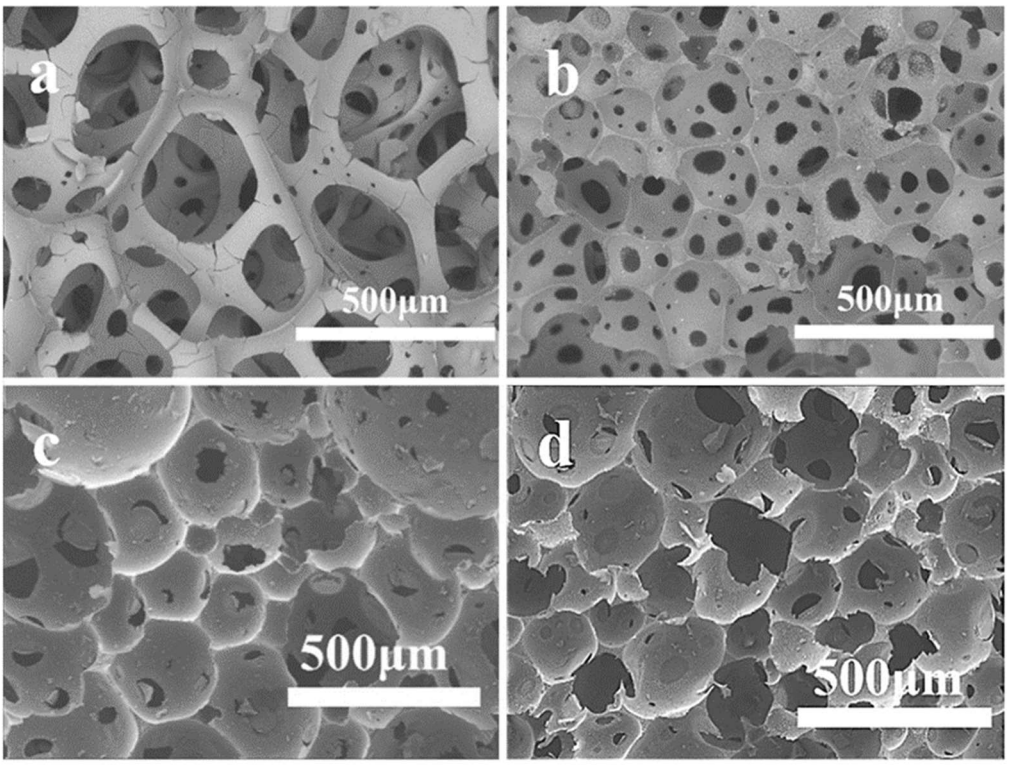

Figure 1.23. ZrC ceramics made by the carbothermal reduction of ZrO_2 and C by the forming system of water, methanol, n-pentane (blowing agent) and ammonia (curing agent) (modified from [129])

Various fabrication methods and structures of the macroporous materials were introduced. While each result is an impressive achievement, challenges in the process for producing a porous body still remain. In partial sintering, the pore volume and pore size depend on the grain size of the raw material, thus the structure cannot be freely designed. In sacrificial fugitives and direct foaming, there is a strong relationship between the number of pores and connectivity, so there tends to be a trade-off relationship between the strength and connectivity. With replica templates, very interesting structures were obtained, however, in order to evenly introduce the material into the template, a structure of large macropores tends to be created. In this study, a process to create a structure with finely interconnected macropores even in materials with a moderate porosity and strength was proposed.

1.3.2 Starch as a pore-forming agent

As mentioned in Section 1.3.1, starch has been used as a pore-forming agent in the sacrificial fugitive in previous studies. However, in these studies, starch is reported as a kind of particulate pore former that forms spherical pores.

On the other hand, starch is generally known to form network structures[132, 133]. Our research group is investigating the use of the network structure of starch as a pore-forming agent for making connected porous structures[134].

Starch is a polysaccharide that is produced by photosynthesis in plants. Starch is composed of amylose, which has a linear structure, and amylopectin, which has a complex branched structure, and is produced by various plants such as corn, wheat, rice, potato, and cassava. Raw starch powder is not soluble in water at room temperature and forms an opaque suspension. However, starch forms a gel with an α-starch network when heated with water and the gel turns into solidified ß-starch after cooling. These properties of starch networking upon heating and cooling are called gelatinization and retrogradation, respectively. This phenomenon is thought to be a kind of phase transition that occurs when amylose and amylopectin, which are macromolecular components constituting starch, absorb and separate water. Figure 1.24 shows the morphological changes in rice starch due to gelatinization and retrogradation. This change occurs by the mechanism shown in the schematic illustration of Figure 1.25. When water is added to starch and heated, gelatinization occurs, and the starch granules absorb water and swell. Amylose dissolves in hot water. Amylopectin does not dissolve in hot water, but it absorbs water and swells. Upon subsequent cooling, the starch hardens as the amylose molecules rearrange and the amylopectin molecules recrystallize.

In this study, the fabrication of interconnected macropore ceramics using starch networked by gelatinization and retrogradation as a pore-forming agent was attempted.

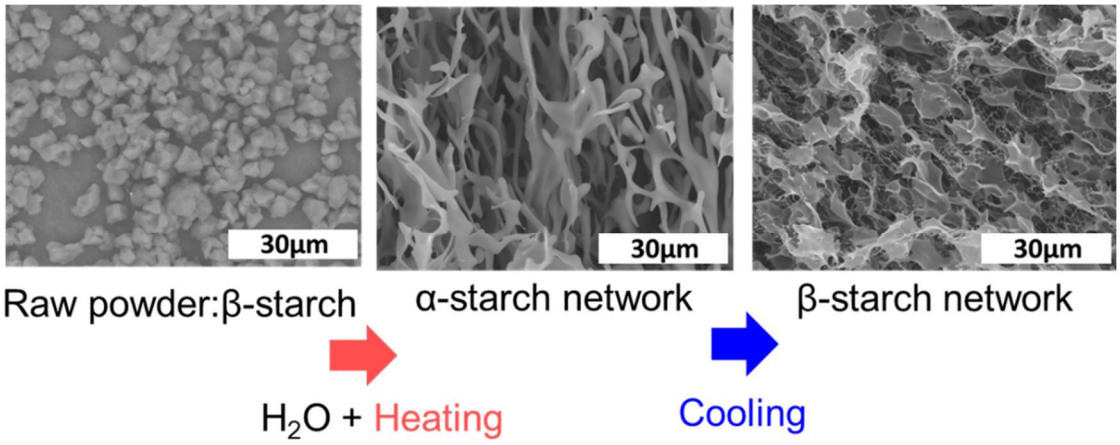

Figure 1.24. Morphological changes of rice starch due to gelatinization and retrogradation [134]

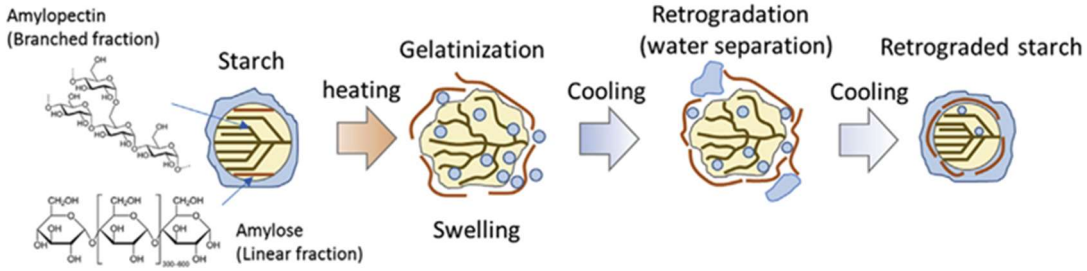

Figure 1.25. Phenomena of starch gelatinization and retrogradation [134]

1.4 Characterization method for pore structure

1.4.1 General characterization method

The following section describes the general methods for the characterization of pore materials. Gas adsorption/desorption measurements, mercury porosimetry, structure observations with an electron microscope (Scanning electron microscope: SEM, Transmission Electron Microscope: TEM), observations with an optical microscope and X-ray computed tomography are known. These methods are used according to the size of the pores that need to be characterized. Whether a quantitative evaluation or qualitative characterization is required is an important factor. Figure 1.26 shows the pore size range applicable to each characterization method[135].

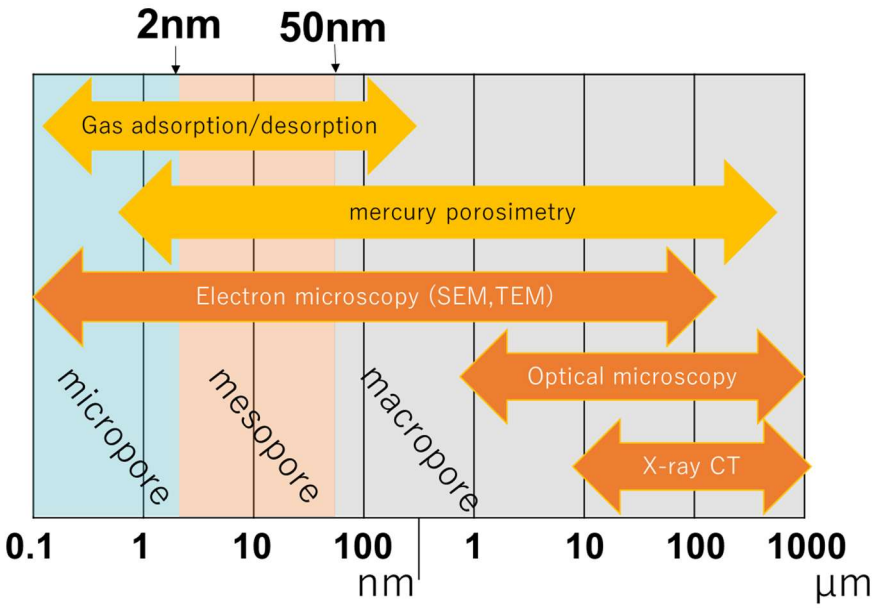

Figure 1.26. Characterization method for pore structure

The gas adsorption measurement can quantify micropores up to about 500 nm in diameter, but it is said that pore diameters up to about 100 nm can be measured with a high accuracy[136]. Mercury porosimetry is often used for the quantitative evaluation of

pores with diameters larger than of 100 nm. However, in recent years, the use of mercury tends to be restricted due to its designation as a hazardous substance in the RoHS Directive, and alternative methods are desired.

SEM, TEM, and optical microscopy are often used for the characterization of the pore morphology. The observations of a pore structure by a microscope is a convenient method, but characterization is sometimes difficult because the observed structure is limited to two dimensions. In addition, it is difficult to quantitatively evaluate the size and amount of the pores. It should be noted that the machining method of the observed sample may change the apparent pore structure. When observing the fracture surface, the sample breaks from the fragile point with large pores. There is also a method of fixing the structure with resin and polishing the cross section for observation, but since porous materials are generally fragile, particles tend to fall off during the polishing, making sample processing difficult in many cases. There is a three-dimensional observation method using SEM that combines a focused ion beam (FIB) device[137]. The maximum field of view of this observation method is about 100 μm square, and the sample is destroyed during observation. Although it is a difficult technique for observing fragile porous materials, the method can be selected when a detailed three-dimensional observation is desired with a field of view of 100 μm or less.

Another three-dimensional observation method is X-ray Computed Tomography. With general industrial micro–X-ray Computed Tomography equipment, it is difficult to image structures of several microns in terms of resolution. X-ray microtomography at a synchrotron radiation facility can be cited as a method that enables three-dimensional observations with a higher resolution, but the ease of use is a problem.

1.4.2 Gas adsorption/desorption measurement

Physical adsorption (physisorption) measurements are used for the determination of the surface area and pore size distribution[138]. At cryogenic temperatures, weak molecular attraction forces will cause the gas molecules to reversibly adsorb on the surface of the solid material. Gas is added to the sample in controlled doses, and the pressure in the sample container is measured after each dosing. A direct relationship exists between the pressure and the volume of gas in the sample container if the temperature is constant. The volume of gas adsorbed by the sample can be determined by measurement of the reduced pressure due to the adsorption. This relationship is known as an adsorption isotherm [139]. Physisorption isotherms were grouped into six types by the IUPAC[1]. Furthermore, Type I and Type Ⅳ have the sub-categories (a) and (b), respectively. The classification of physisorption isotherms is shown in Figure 1.27. Differences in the isotherm shapes are explained by phenomena during the adsorption process such as micropore filling, monolayer-adsorption, multilayer-adsorption, and capillary condensation.

A description of the classifications taken from the IUPAC report is as follows:

Reversible Type I isotherms are given by microporous solids having relatively small external surfaces. This limiting uptake of the amount of adsorptive is governed by the accessible micropore volume. A steep uptake at very low p/p_0 is due to enhanced adsorbent-adsorptive interactions in narrow micropores, resulting in micropore filling. Type I(a) isotherms are given by microporous materials having mainly narrow micropores (of width < ~ 1 nm); Type I(b) isotherms are found with materials having pore size

distributions over a broader range including wider micropores and possibly narrow mesopores (< ~ 2.5 nm).

Reversible Type II isotherms are given by the physisorption of most gases on nonporous or macroporous adsorbents. The shape is the result of unrestricted monolayer-multilayer adsorption up to high p/p_0.

In the case of a Type III isotherm, there is no Point B and therefore no identifiable monolayer formation; the adsorbent-adsorbate interactions are now relatively weak and the adsorbed molecules are clustered around the most favorable sites on the surface of a nonporous or macroporous solid.

Type IV isotherms are given by mesoporous adsorbents (e.g., many oxide gels, industrial adsorbents, and mesoporous molecular sieves). The adsorption behaviour in mesopores is determined by the adsorbent-adsorptive interactions and by the interactions between the molecules in the condensed state. In this case, the initial monolayer-multilayer adsorption on the mesopore walls, which takes the same path as the corresponding part of a Type II isotherm, is followed by pore condensation. Pore condensation is the phenomenon whereby a gas condenses to a liquid-like phase in a pore at a pressure p less than the saturation pressure p_0 of the bulk liquid.

In the case of a Type IVa isotherm, capillary condensation is accompanied by hysteresis. This occurs when the pore width exceeds a certain critical width, which is dependent on the adsorption system and temperature (e.g., for nitrogen and argon adsorption in cylindrical pores at 77 K and 87 K, respectively, hysteresis starts to occur for pores wider than ~ 4 nm). With adsorbents having mesopores of smaller width, completely reversible Type IVb isotherms are observed. In principle, Type IVb isotherms are also given by conical and cylindrical mesopores that are closed at the tapered end.

In the low p/p_0 range, the Type V isotherm shape is very similar to that of Type III and this can be attributed to relatively weak dsorbent–adsorbate interactions. At higher p/p_0, molecular clustering is followed by pore filling. For instance, Type V isotherms are observed for water adsorption on hydrophobic microporous and mesoporous adsorbents.

The reversible stepwise Type VI isotherm is representative of layer-by-layer adsorption on a highly uniform nonporous surface. The step-height now represents the capacity for each adsorbed layer, while the sharpness of the step is dependent on the system and the temperature. Amongst the best examples of Type VI isotherms are those obtained with argon or krypton at low temperature on graphitised carbon blacks.

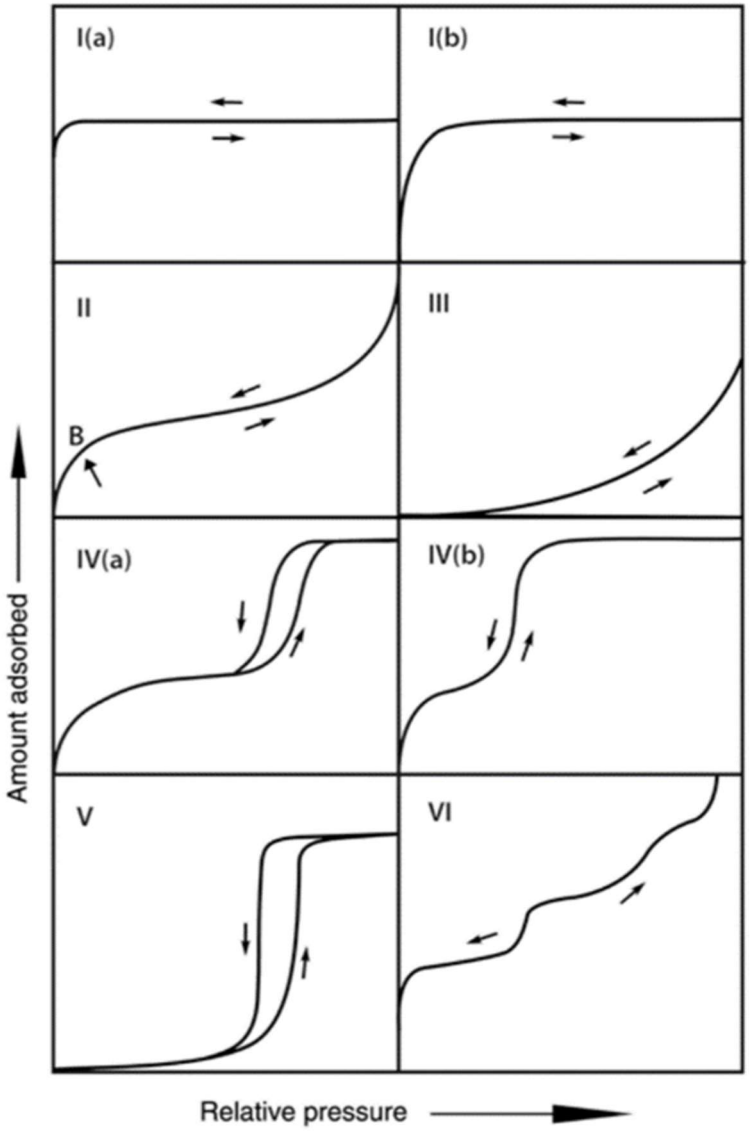

Figure 1.27. Classification of physisorption isotherms [1]

The surface area of the material can be calculated from knowledge of the size and number of the adsorbed gas molecules. The theory of gas adsorption in multimolecular layers, as a means of determining the surface area of materials, was first described by Brunauer et al. in 1938[140]. The Brunauer-Emmett-Teller (BET) gas adsorption method has become the most widely used standard procedure for the determination of the surface areas of porous materials. The BET equation is used to determine the volume of a gas

needed to form a monolayer on the surface of a sample. The BET equation is defined as follows:

$$\frac{1}{v[(p_0/p)-1]} = \frac{c-1}{v_m c}\left(\frac{p}{p_0}\right) + \frac{1}{v_m c}$$

where v is the specific amount of the adsorbed gas at the relative pressure p/p_0, v_m is the monolayer capacity of the adsorbed gas, p is the pressure, p_0 is the saturation pressure of a substance being adsorbed at the adsorption temperature, and C is the BET constant.

The Langmuir theory assumes that gas molecules form a monolayer adsorption which is an ideal situation. For a multilayer adsorption, assuming all layers are in equilibrium and do not interact with each other, the BET equation approximates the Langmuir equation. The surface area is determined from the slope and intercept of the BET plot. The BET equation is used in the range of p/p_0=0.05-0.35 due to the assumption of the BET formula that the gas adsorption layer is infinite does not hold in the high-pressure region.

The hysteresis loop observed in mesoporous materials is explained by capillary condensation[141]. The following Kelvin equation applies:

$$r_k = -\frac{2\gamma V_m}{RT\ln\left(\frac{p}{p_0}\right)}$$

where r_k is the radius, γ is the surface tension, V_m is the molar volume, p/p_0 is the relative pressure, R is the gas constant, T is the absolute temperature, p is the vapor pressure

and p_0 is the saturated vapor pressure on a flat surface. The BJH-plot method uses Wheeler's cylindrical pore model to convert the relative pressure into the pore diameter and obtain the mesopore size distribution from the desorption isotherm[142-144]. BJH plots are not applicable to micropores as the capillary condensation theory is not applicable to pores smaller than 2 nm.

A schematic representation of the relationship between the isotherms and the progress of gas adsorption/desorption is shown in Figure 1.28.

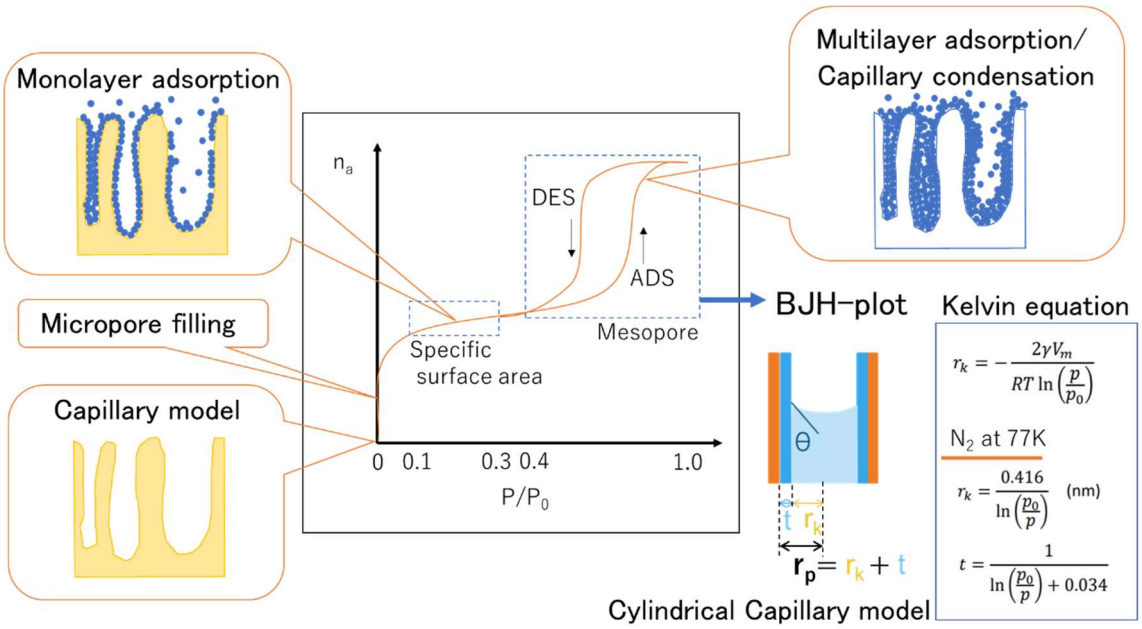

Figure 1.28. Relationship between the isotherms and the progress of gas adsorption/desorption

1.4.3 Mercury porosimetry

Mercury porosimetry[145, 146] is a common method employed for the characterization of relatively large pores, in particular macropores. Ordinary liquids that contact with capillaries on a solid surface enter the pores by capillary action, while mercury is forced out of the capillaries due to the large surface tension that exhibits a contact angle of over 90° with most solids. The mercury porosimetry utilizes this phenomenon.

The method is applied to a cylindrical pore model and the following equation holds:

$$\Delta P = -2\gamma \cos(\theta)/R$$

where ΔP is the pressure across the interface, γ is the fluid surface tension, θ is the contact angle of the fluid and R is the equivalent radius of the cylindrical pores.

Mercury porosimetry generally characterize the pore size distribution from the intrusion curve at pressurization, but there are also cases where the extrusion curve is measured. It has been reported that the indentation curve and the extrusion curve do not overlap when the pore shape is not cylindrical, but like an 'ink-bottle' shape; the entrance is narrow and the diameter increases toward the inside. Attention should be paid to the difference between the theoretical assumptions and actual pore shapes.

1.4.4 Three-dimensional observation method by liquid immersion technique

The structure produced by the starch pore-forming agent has a size order of several microns, as shown in Figure 1.24, Section 1.3.2. In order to effectively characterize the pore structure with a size order of several microns made by the starch pore forming agent introduced in the previous chapter, a unique characterization technique by confocal laser fluorescence microscopy using a liquid immersion method was applied. The technique is a three-dimensional observation method of a ceramics internal structure in high resolution based on observation methods developed to characterize defects in ceramic green bodies and granules[147-149]. The liquid immersion method is also an internal structure observation technique that can be applied to a system in which the material is transparent to the observation light and has a little optical anisotropy. A ceramic compact or a bulk body becomes transparent when an immersion liquid having the close refractive index to the raw material of the sample is permeated into the open pores, thus reducing light scattering on the surface of the raw material. Observation inside the samples becomes available using a fluorescent microscope by dissolving a small amount of fluorescent agent in the immersion liquid. In this study, this technique was used to characterize the structure of the porous ceramics. Figure 1.29 shows a schematic illustration of the observation method of the pore structure by a confocal laser fluorescent microscope using the liquid immersion method.

This is the first time that the observation technique has been used to characterize the three-dimensional pore structure of porous ceramics. It is also the first time to apply the liquid immersion method to the material systems of zeolite and hydroxyapatite. One of the purposes of this research is to verify whether the observation method can be used to characterize the structure of pores compared to the general characterization method.

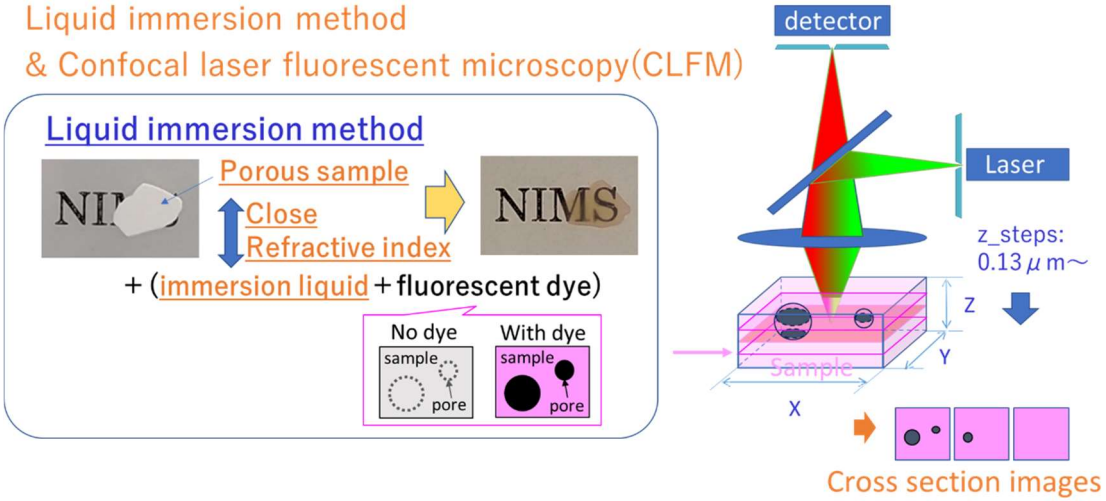

Figure 1.29. Observation of pore structure by a confocal laser fluorescent microscope using the liquid immersion method

1.5 Objective of the thesis

The objective of this thesis is as follows:

・Designing and fabrication of hierarchical porous zeolite bulk bodies with micropores, macropores and mesopores, and clarification of their structures and properties. The zeolite bulk has advantages such as excellent surface function due to the micropores, support/adsorption function due to the mesopores, and high-speed mass transfer due to the macropores.

・Clarification of the applicability of a material that combines the microstructure and macroporous structure of HAp.

・Clarification that the networked starch can be used as a pore-forming agent to control the macropore structure of ceramics.

・ Establishment of a three-dimensional observation method for characterizing the pore structure is verified in comparison to the general characterization methods.

Chapter 2 | Fabrication of zeolite bulk body and characterization of pore structure

2.1 Introduction

Zeolites are microporous crystalline aluminosilicates known as molecular sieves that have been widely used in industry as adsorbents, catalysts, and ion exchangers. The hydrothermal method is commonly used for the synthesis of zeolites, which are generally obtained as powders consisting of nano- to micron-sized crystals [30, 67, 73]. The molecular sieving ability of zeolites depends on their crystalline structure containing pores and cavities of molecular dimensions. Efforts have long been made to increase the pore size of the zeolite crystal units due to the potential capacity of chemical processes that require larger pore spaces as reaction fields. Consequently, the synthesis of extra-large pore zeolites has been attempted [37-39, 71, 150, 151], leading to the synthesis of ITQ-37 having a 30-membered ring. However, the diameter of the largest-free-sphere of zeolite units listed in the IZA database [36] is still less than 10 Å. For now, the reactants or supported materials on the zeolites are limited in terms of cavity size. Mesoporous materials, such as MCM-41, are also known as zeolite-like materials with nanoscale pore size structures [30, 40, 152, 153]. However, due to their low crystallinity, their ability to act as acid catalysts is lower than that of the zeolites.

Zeolite bulks containing mesopores and macropores have a significant potential to improve the capabilities of larger molecular reactors. S. Zou *et al.* reported the synthesis of a hierarchically porous zeolite using a polyurethane foam template [154], and M. Anderson *et al.* proposed a biomineralization method using diatoms [127]. However, they did not mention the mechanical strength of the resulting products. The handling

availability with a sufficient mechanical strength is an important factor for practical use as a bulk body. E. Igi *et al.* synthesized a porous zeolite bulk body by a one-pot hydrothermal method and reported that it had a sufficient mechanical strength for machining[155, 156]. A new processing method is now proposed for producing a porous zeolite bulk body that contains micropores, mesopores, and macropores and has a sufficiently high mechanical strength for handling. Hybrid materials consisting of zeolites and functional particles are expected to be used as novel catalysts or purification filters. Mesopores will be effective in supporting the functional nanoparticles. Continuous macropores will be essential for the smooth flow of a gas or liquid that needs to be treated.

Starch has been used as a pore-forming agent, and a hierarchical porous structure was introduced into the zeolite bulks. Starch forms a gel with an α-starch network when heated with water. The α-starch gel turns into solidified ß-starch after a cooling process while keeping the network structure[132, 133]. This starch property is appropriate for a pore-forming agent to make a networked porous structure [134]. The morphological changes of the pore structure in the zeolite bulk body involved with the gelation treatment of the pore-forming agent were investigated. In order to reveal the hierarchically pore structure, it is necessary to investigate the existence of micropores with a diameter of less than 2 nm, mesopores with a diameter of 2-50 nm, and macropores with a diameter of more than 50 nm. Micropores and mesopores can be generally characterized from N_2 gas adsorption/desorption isotherms [1, 138, 139]. For macropores, the direct observation of the pore structure using a confocal laser fluorescent microscope (CLFM) employing the liquid immersion method was attempted. It is a high-resolution three-dimensional observation method which was developed to characterize

the defects in a ceramic green-body and granules[148, 149]. The liquid immersion method is also an internal structure observation technique that can be applied to a system in which the material is transparent to the observation light and has a little optical anisotropy. Observation inside the samples becomes available using a fluorescent microscope by dissolving a small amount of fluorescent agent in the immersion liquid.

2.2 Experimental Procedure

Commercially-available ZSM-5 zeolite powder (HSZ-840HOA, Tosoh Corp., Japan) was used as the starting material. Aqueous colloidal silica (Snowtex ST-S, Nissan Chemical Corp., Japan) with the average particle size of 9 nm, containing 30 wt% SiO_2, was used as a binder. The ZSM-5 powder was added to the aqueous colloidal silica so that the weight ratio of zeolite to silica was 2:1. The slurry was ball-milled at 30 rpm for 24 hours using a zirconia ball medium (2- 10 mm diameter). Rice starch powder (Sigma-Aldrich Co. LLC) with the particle size range of 2.0- 8.0 μm was added to the slurry as a pore-forming agent in the amount of 20 wt% or 0 wt% vs. the solid contents in the slurry. The starch was mixed and dispersed in the slurry using a planetary centrifugal mixer (ARE-310, THINKY Corp., Japan) at 2000 rpm for 5 minutes. The slurry was cast into acrylic molds with a 16-mm diameter and steamed in water vapor at 80 ℃ for 10 minutes to gelatinize the starch or just dried with no heating. The green bodies were treated in an autoclave for 24 hours in steam at 180 °C without direct contact with water as shown in Figure 2.1 to bind the zeolite particles by a surface reaction between the colloidal silica and the zeolite. The consolidated bodies were then thermally treated in air at 450 ℃ for 24 hours to remove the starch. Finally, three porous zeolite bulk bodies formed by different processes were obtained. In other words, the following three types of samples were prepared as (1) starch-free (sample without starch), (2) starch-added (sample with starch and no heat-treatment), and (3) starch-gelated (sample with starch and heat-treatment at 80 ℃). The schematic illustrations of the expected internal structures of each sample are shown in Figure 2.2.

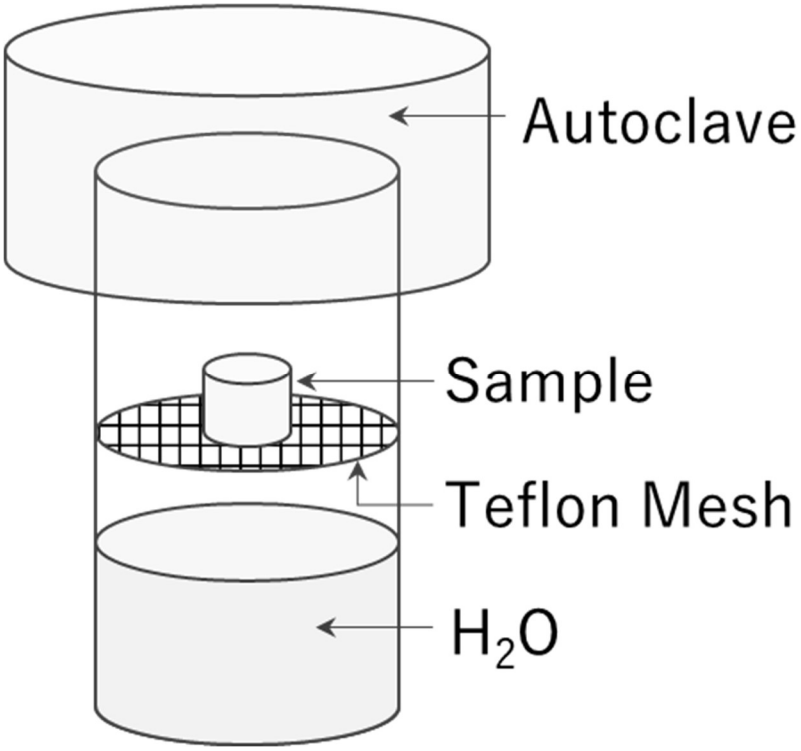

Figure 2.1. Schematic illustration of the sample heating process in an autoclave

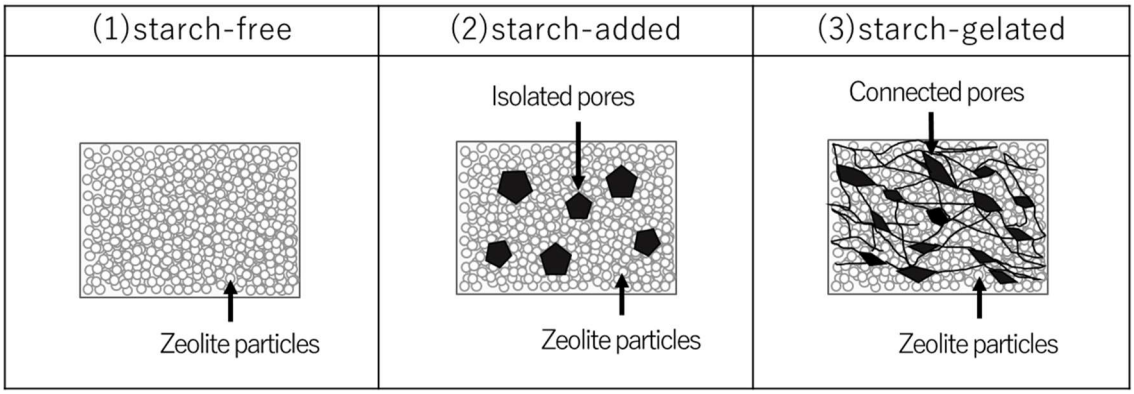

Figure 2.2. Schematic illustrations of the expected internal structure of each sample

The crystal structures of the raw zeolite powder and the bulk samples were identified by an X-ray powder diffraction measurement (Miniflex600, Rigaku) with CuKα radiation. The pore size distribution in the mesoporous region was characterized by a nitrogen-gas adsorption/desorption measurement using a surface area and pore distribution size analyzer (BELSORP-Ⅱ, MicrotracBEL). The Barrett-Joyner-Halenda (BJH) method was applied to the desorption isotherm to calculate the pore size distribution. The BJH method is based on the Kelvin equation, which assumes a system of open-ended, cylindrical mesopores. The capillary radius can be calculated when capillary condensation occurs from the Kelvin equation [144]. The specific surface area was calculated from the αs-plot since the Brunauer-Emmet-Teller (BET) theory is not applicable to microporous materials [1]. The fracture surface of the bulk bodies was observed by scanning electron microscopy (JSM-6500F, JEOL). The internal structure of the bulk bodies was observed by a confocal scanning laser fluorescence microscope (TCS-SP5, Leica Microsystem) using the liquid immersion method. The sample became transparent to visible light when the immersion liquid, which has the refractive index n close to that of the base material, permeated into the samples due to reducing the reflection of light at the interface of the powder particles and the surrounding medium. The refractive index of the synthesized ZSM-5 is 1.48[157], therefore, 1-methyl-2-francalboxyrate (n =1.48-1.49) [158]was selected as the immersion liquid. The fluorescent agent, Rhodamine B, was dissolved in the immersion liquid before liquid permeation to distinguish between the open pores and zeolite bulk. The samples were fractured, then ground with an abrasive paper to a thickness of 200-500 μm before the liquid immersion. The internal microstructures of the samples were observed by confocal scanning laser fluorescence microscopy. Cross-sectional images of the sample were

acquired continuously at arbitrary intervals of 0.08 to 0.26 μm from the surface to approximately a 100-μm depth. The sliced images were binarized into the pore and base material phases, then these images were stacked to create a three-dimensional image using image processing software (AVIZO, Thermo Fisher Scientific, Inc.). The density of the bulk bodies was measured by Archimedes' method using kerosene as the solvent.

The pore distributions of the three bulk bodies were evaluated by mercury porosimetry, (AutoPore Ⅳ 9520, Micromeritics Instrument Corp.) measuring the intrusion and extrusion curves.

2.3 Results and Discussion

Hard, crack-free bulk samples were successfully fabricated. A zeolite bulk body with gelated starch is shown in Figure 2.3. The other samples are also white lumps, suggesting that the starch has been completely removed. X-ray diffraction patterns of the raw ZSM-5 powder and the bulks are shown in Figure 2.4. All the peaks of the bulk samples were identified as peaks of the ZSM-5 phase. The results indicated that the bulk body maintained the crystal structure of the ZSM-5 zeolite through all the processes. The colloidal silica phase did not appear in the XRD probably because it remained as an amorphous phase.

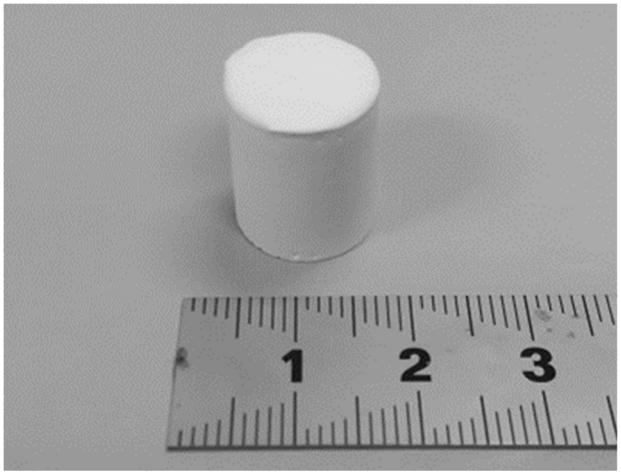

Figure 2.3. A zeolite bulk body (starch-gelated sample)

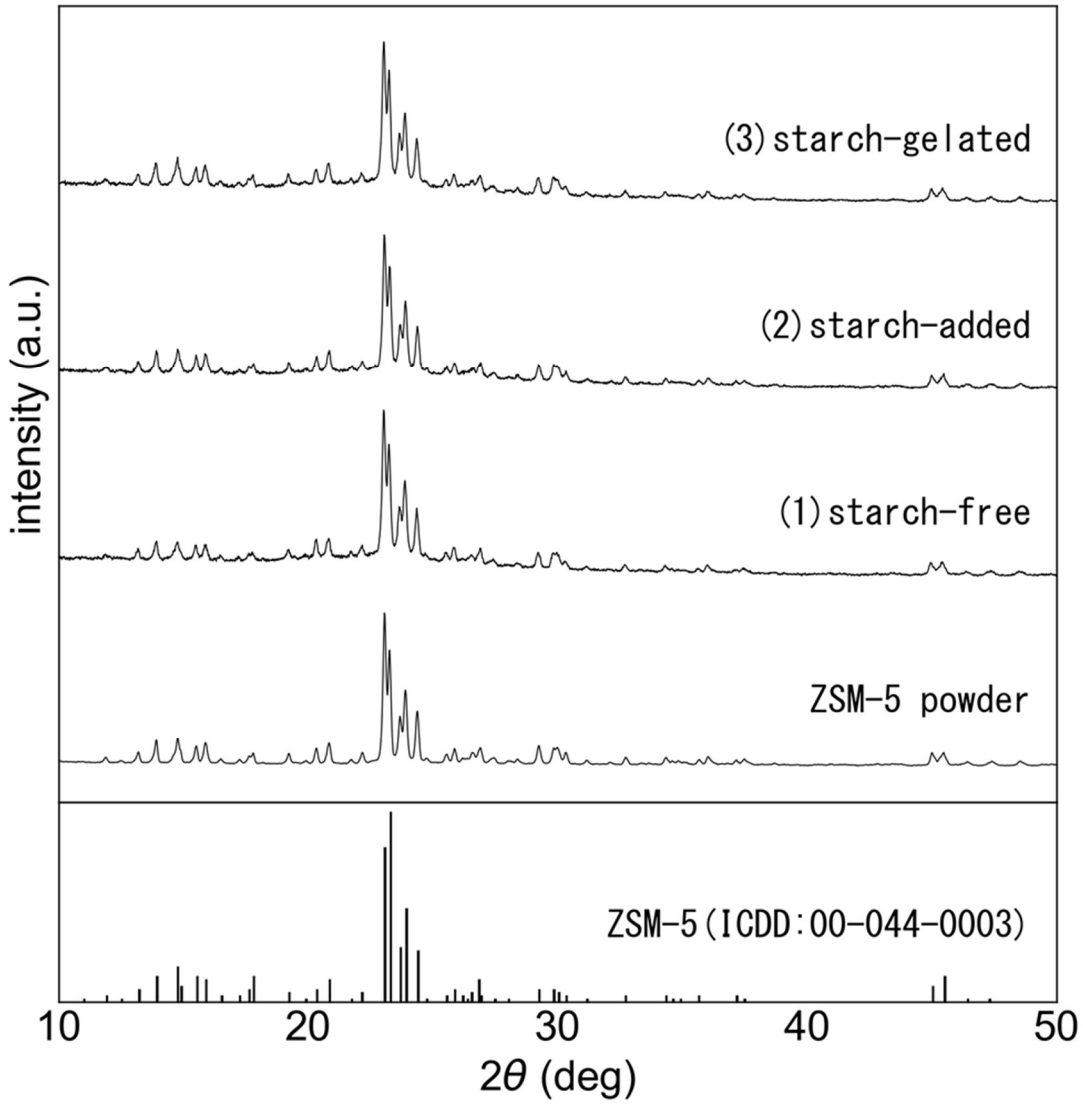

Figure 2.4. X-ray diffraction patterns of raw ZSM-5 powder and the bulk samples

The N_2 adsorption/desorption isotherms measured at 77 K are shown in Figure 2.5. According to the IUPAC classification, the isotherm of the raw ZSM-5 powder is classified as type I (a), indicating that it was a typical microporous material. On the other hand, the isotherms of the bulk bodies showed hysteresis loops which were provided by mesoporous adsorbents classified as Type IV(a). However, the isotherms of the bulk samples also indicated a steep uptake at a very low relative pressure, the same as the raw material due to the micropore filling. In addition, the successive uptake of the bulk's isotherms in the high relative pressure region revealed the presence of macropores. This suggested that the bulk samples contained pores of various sizes not found in the raw zeolite powder, such as mesopores and macropores. There was no significant difference in the shape of the adsorption isotherm between the starch-free sample and the starch-added sample. The starch-gelated sample clearly increased the amount of adsorption at the same relative pressure. For example, the amount of adsorption at a relative pressure of around 1.0 was approximately 200 cm^3(STP)/g for the starch-free sample and the starch-added sample, while it was approximately 240 cm^3(STP)/g for the starch-gelated sample.

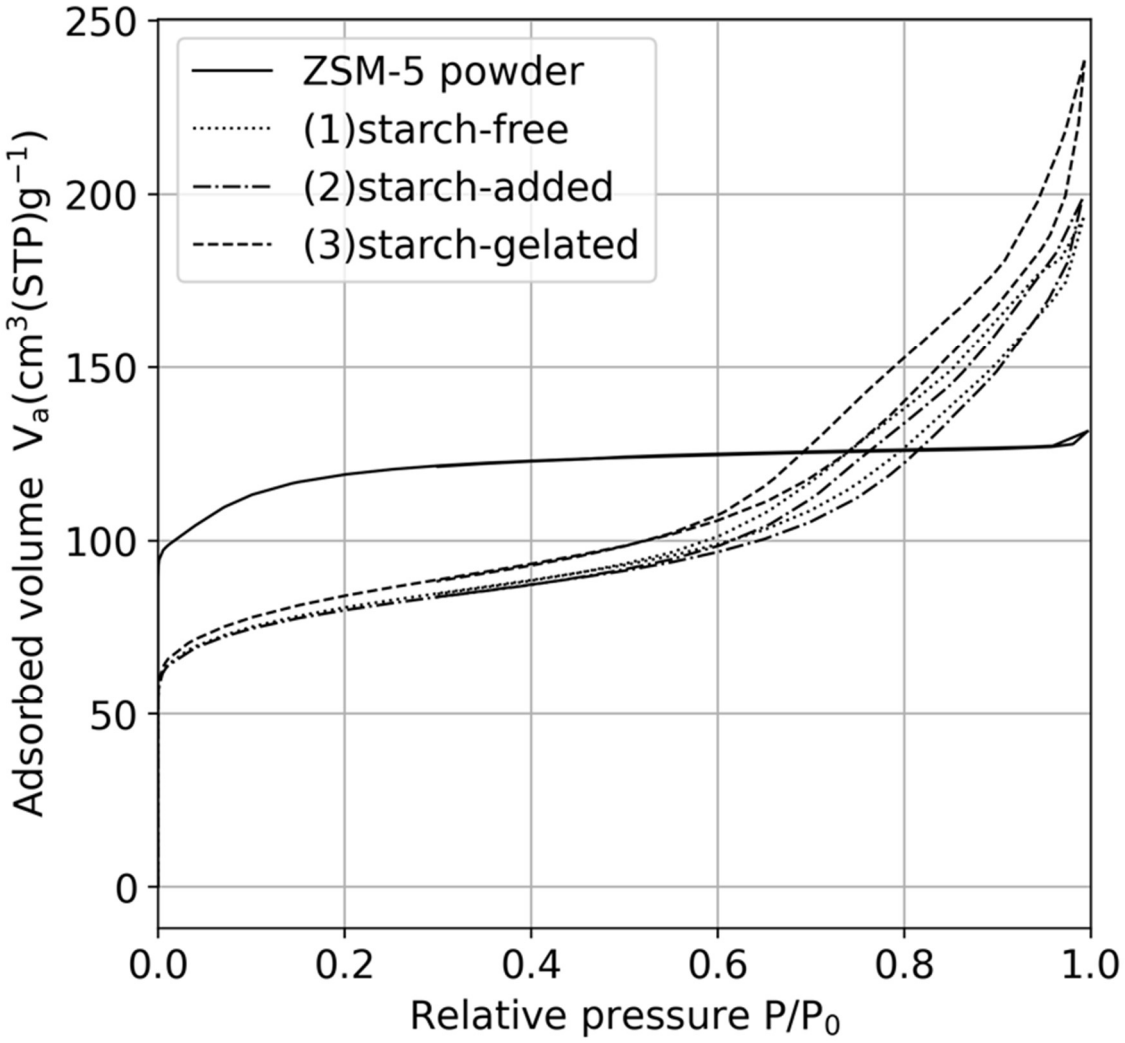

Figure 2.5. N_2 adsorption/desorption isotherms measured at 77K

The pore size distributions obtained from the BJH plots are shown in Figure 2.6. Since the capillary condensation theory cannot be applied to pores below 2 nm, the BJH plot cannot provide micropore comparisons. However, it is effective for discussion about the mesopore region. All the bulk samples had a peak distribution at 7-9 nm, corresponding to mesopores, regardless of the addition of starch. It was also found that starch-gelated sample contained the largest volume of mesopores. The amount of mesopores did not significantly change between the starch-free and starch-added samples. The results mean that mesopores would be formed between the zeolite particles in the bulk, and that they were increased by the starch network structure. The zeolite bulks with mesopores would be suitable for supporting functional nanoparticles. The specific surface area of the samples calculated by the α_s -plots[143] was as follows: starch-free: 378 m^2g^{-1}; starch-added: 375 m^2g^{-1}; starch-gelated: 387 m^2g^{-1}; ZSM-5 raw powder: 573 m^2g^{-1}. The three bulk samples have very similar specific surface areas to each other, and they were lower than that of the ZSM-5 raw powder. For the bulk sample, the contact between the particles leads to a lower surface area. The presence of the pore-forming agent did not contribute to the specific surface area because the amount of micropores was the dominant factor for the specific surface area of the bulk samples.

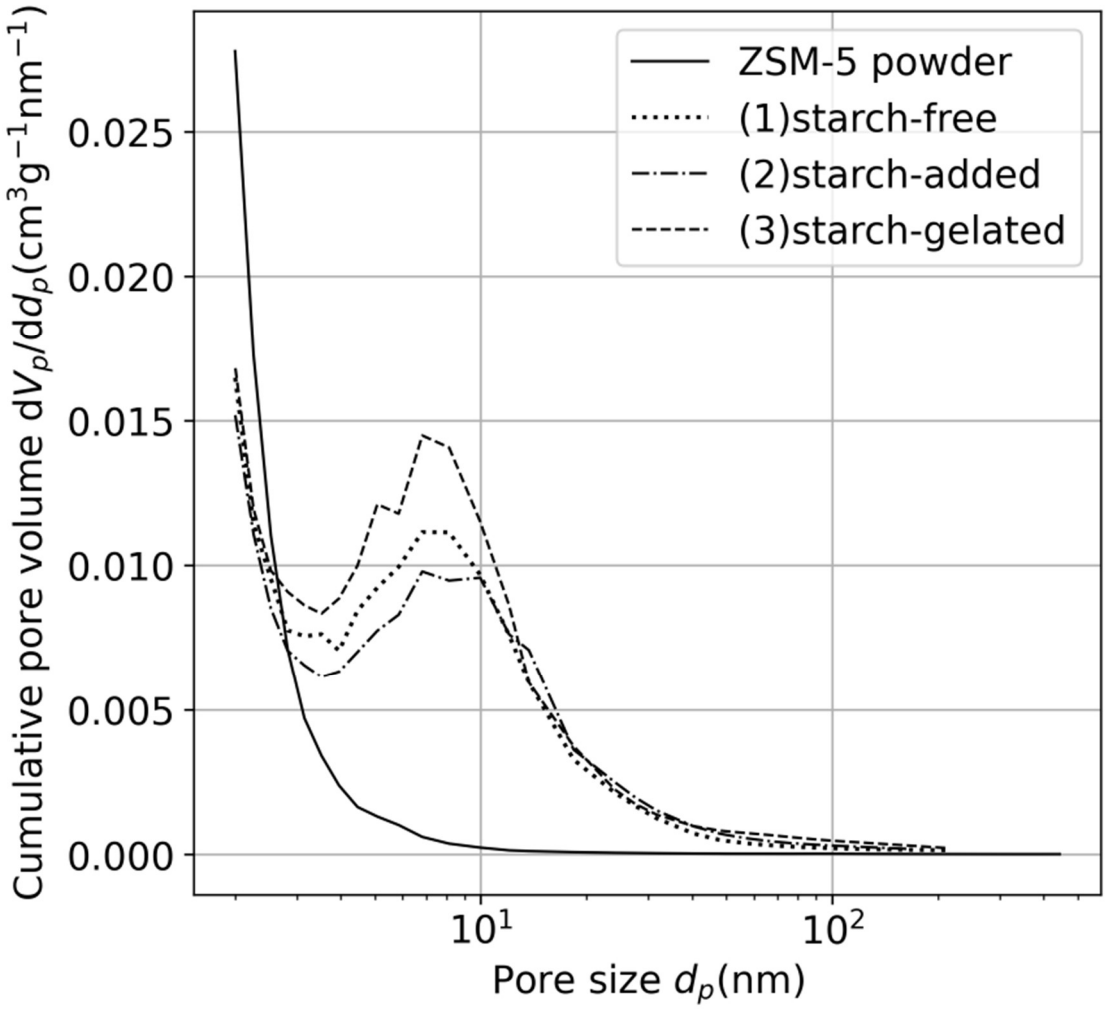

Figure 2.6. Pore size distribution obtained from the BJH plot

The macroporous structures were characterized by observation using a scanning electron microscope (SEM) and a confocal laser fluorescence microscope (CLFM). SEM images of the fracture surface at two different magnifications and CLFM images of the corresponding samples are shown in Figure 2.7. The CLFM images were taken at a depth of 20 mm from the sample surface. Black spots on the CLFM images correspond to pores. The structural images obtained by the two observation methods are similar demonstrating the validity of this internal observation method. Cross-sectional images by CLFM revealed that the structure of the pores clearly changes with the addition of starch and its gelation process. No large pores were observed in the starch-free sample. On the other hand, large pores with a size of more than 5 μm were observed in the starch-added and starch-gelated samples, and the two pore structures are different depending on the presence or absence of the heating process. Based on the higher magnified SEM images, the existence of pores that have a size of less than 1 μm was confirmed.

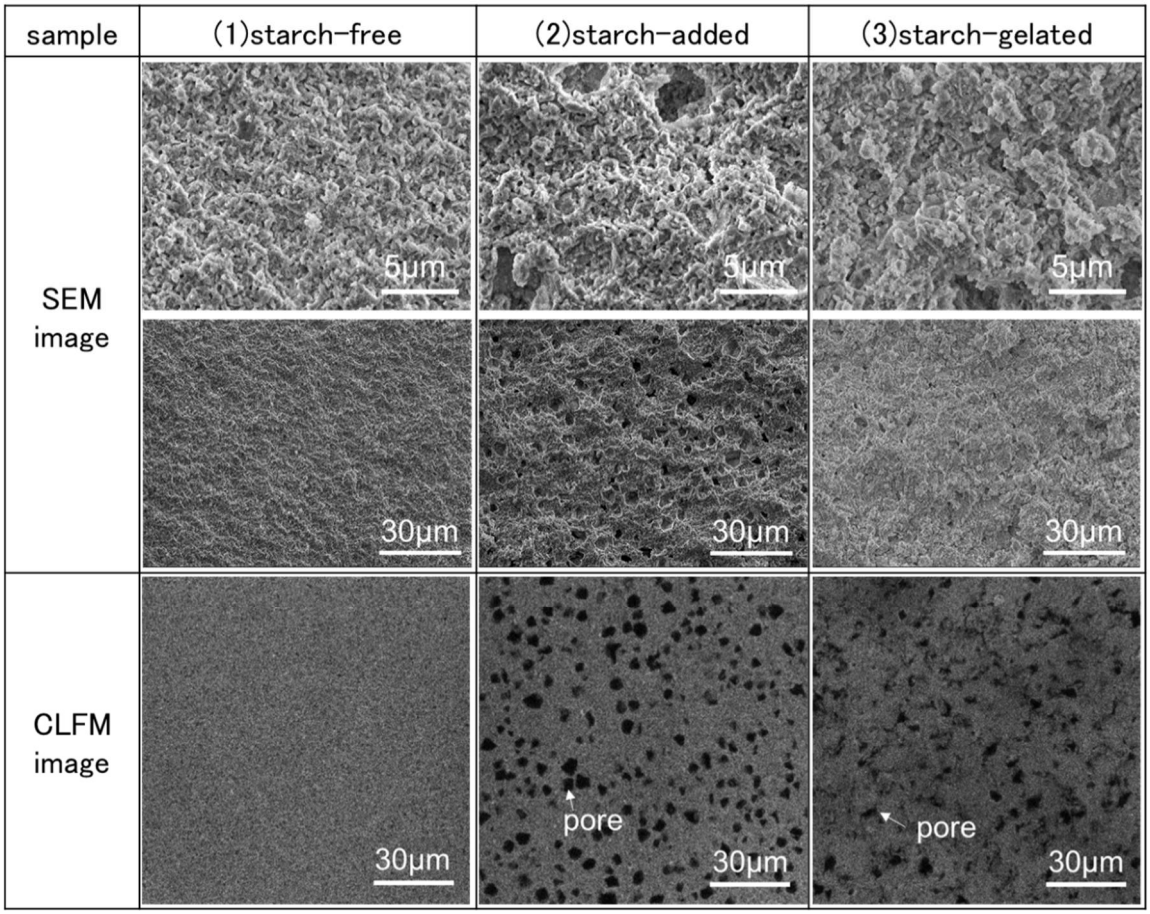

Figure 2.7. SEM images of the fracture surface at two different magnifications and CLFM images of the corresponding samples

The three-dimensional images of the macropores created from the CLFM images at the voxel of 0.08 μm and 0.25 μm are shown in Figure 2.8. Pores are shown in white in the images. The photos of 450 leaves and 280 leaves were used to create the three-dimensional images at each magnification. The acquisition time of the raw photos for one dataset was about 5-15 minutes.

The (1) starch-free sample did not contain micron-sized pores within the observed volume (Figure 2.8 (a), (d)). On the other hand, large-pore structures were observed in the samples with a pore-forming agent (Figure 2.8 (e), (f)). It was confirmed that the (2) starch-added sample had many spherical pores, and (3) the starch-gelated sample had

interconnected pores (Figure 2.8 (b), (c)). Conventional micro-X-ray CT is generally known as a three-dimensional observation method, but it is difficult to observe a pore structure of several microns in terms of resolution, except when using large synchrotron radiation facilities [159-161]. It was demonstrated that the CLFM method is excellent for facilitating the 3D high resolution observations. Results of the density measurement by Archimedes' method is shown in Table 2.1. As already mentioned, the (2) starch-added sample and the (3) starch-gelated sample had different macropore structures, but the porosity measured by Archimedes' method was similar because the same amount of pore-forming agent was added.

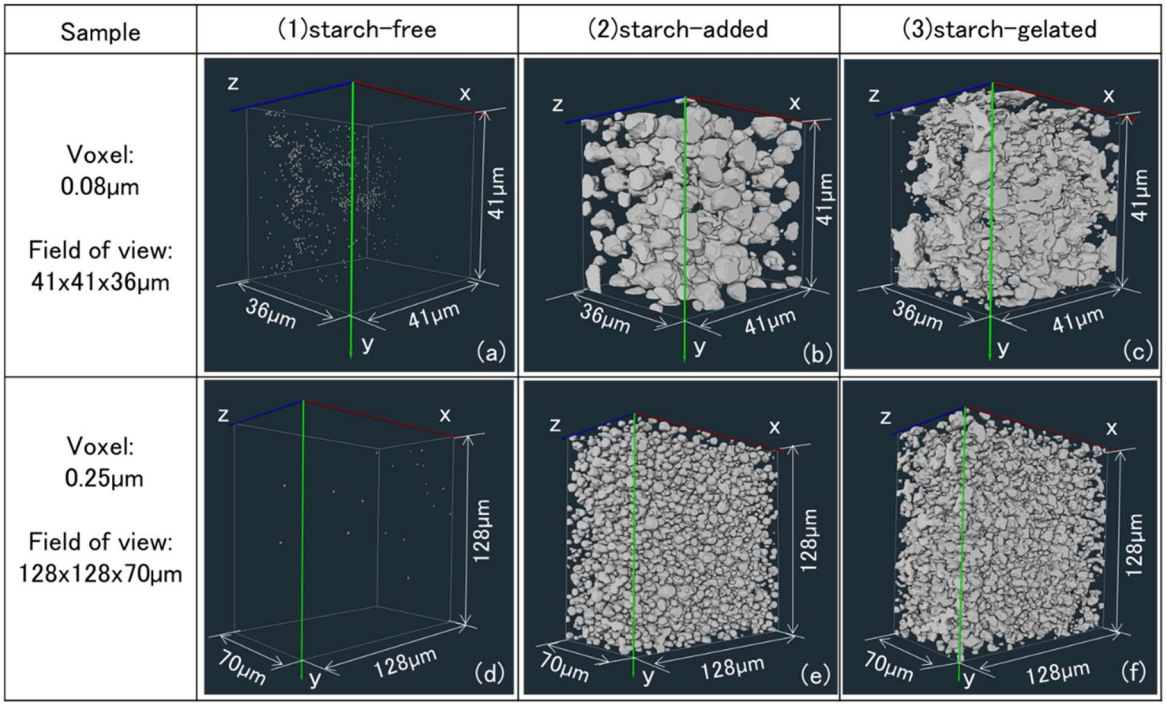

Figure 2.8. The three-dimensional images of macropores created from CLFM images

Table 2.1. Results of density measurement by Archimedes' method

Sample	(1)starch-free	(2)starch-added	(3)starch-gelated
Apparent density(g/cm^3)	2.07	2.06	2.08
Bulk density(g/cm^3)	1.36	1.12	1.13
Porosity(%)	34.2	45.6	45.5

The intrusion and extrusion curves of three zeolite bulk bodies measured by mercury porosimetry are shown in Figure 2.9. The intrusion curve and extrusion curve do not overlap, and the curves indicated a hysteresis shape. As shown in Figure 2.8, the pore shape of the zeolite bulk bodies was complicated and different from the ideal cylindrical shape, resulting in a hysteresis loop.

The pore size distribution of each sample estimated from the intrusion and extrusion curves are shown in Figure 2.10 and Figure 2.11, respectively. The difference in the presence of peaks and shift in the peak position in the two figures are due to the complexity of the pore shape. In Figure 2.10, which is generally regarded as the pore size distribution, all the graphs show a peak at pore sizes below 0.01 μm, consistent with the size of the mesopores confirmed by the gas adsorption measurements. Although the peak positions shift, the peaks around 0.01 μm were also confirmed in Figure 2.11. On the other hand, the large peaks observed around 0.1 μm in Figure 2.10 disappeared in Figure 2.11. The data suggests that the porous bodies had pores with a surface opening size of around 0.1 μm, and the volumes of the internal pores that were accessed through the surface pores were very large. The peak position indicates the entrance size of pore on the surface, that the (3) starch-gelated samples were the largest, and the (1) starch-free samples were the smallest. Pores of several microns, which were confirmed by the CLFM observation, could not be confirmed in Figure 2.10. However, in the enlarged view of

Figure 2.10, peaks that seem to be macropores due to the starch pore-forming agent were confirmed at the position of 4 to 5 μm (Figure 2.12). Since mercury porosimetry measures the size distribution of surface pore entrances, 'ink-bottle' shaped macropores in the bulk are counted as smaller pores. For samples with a hierarchical pore structure, it is difficult to accurately determine the distribution of macropores in the bulk by this method.

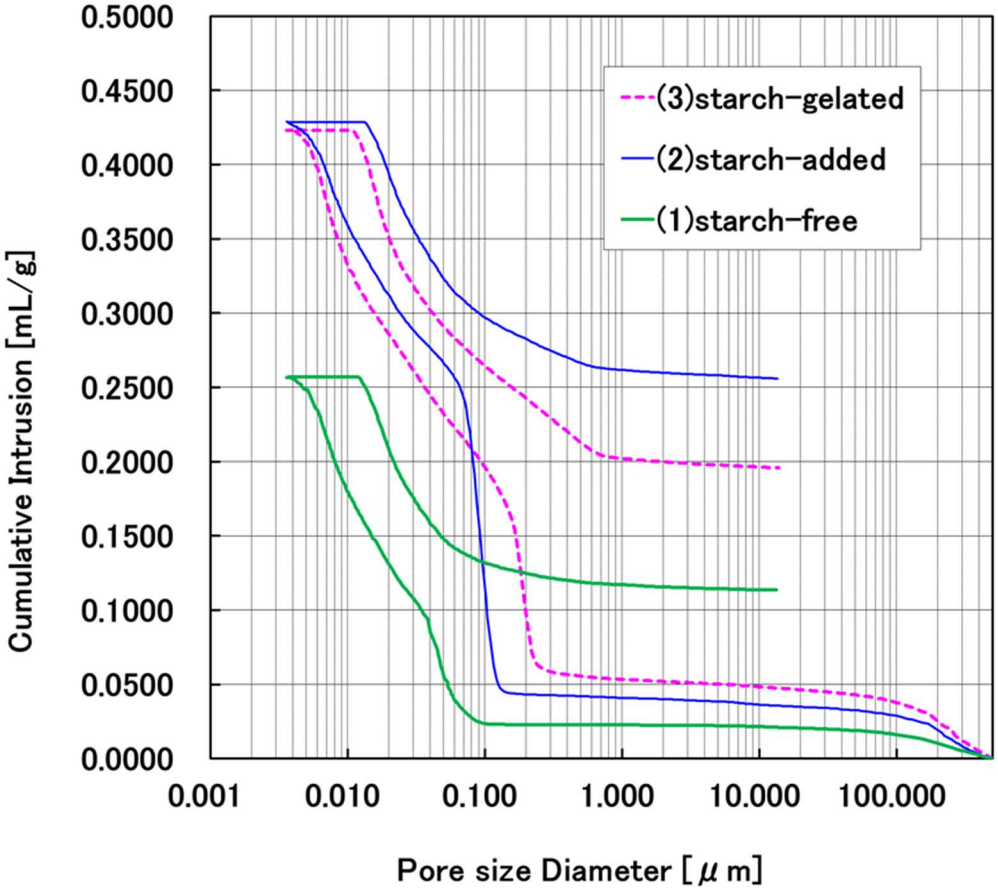

Figure 2.9. Intrusion and extrusion curve measured by mercury porosimetry

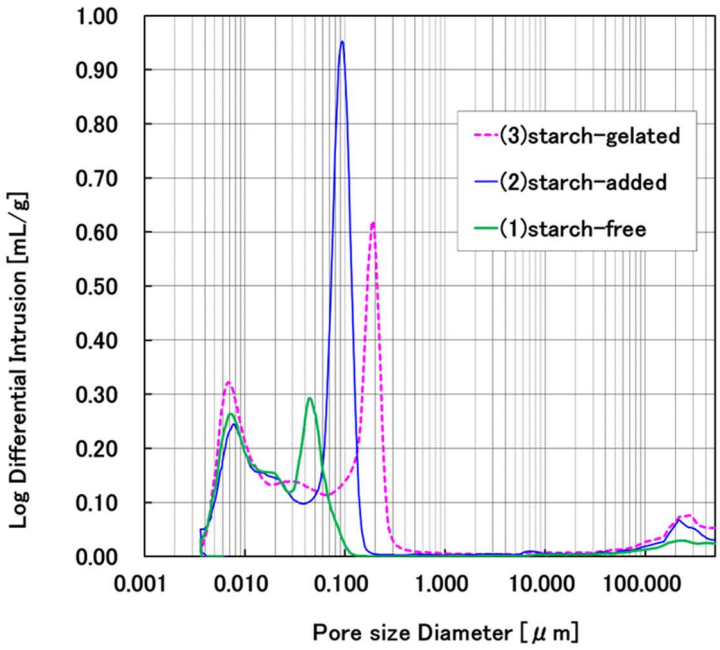

Figure 2.10. Pore size distribution of zeolite bulk bodies estimated from intrusion curves

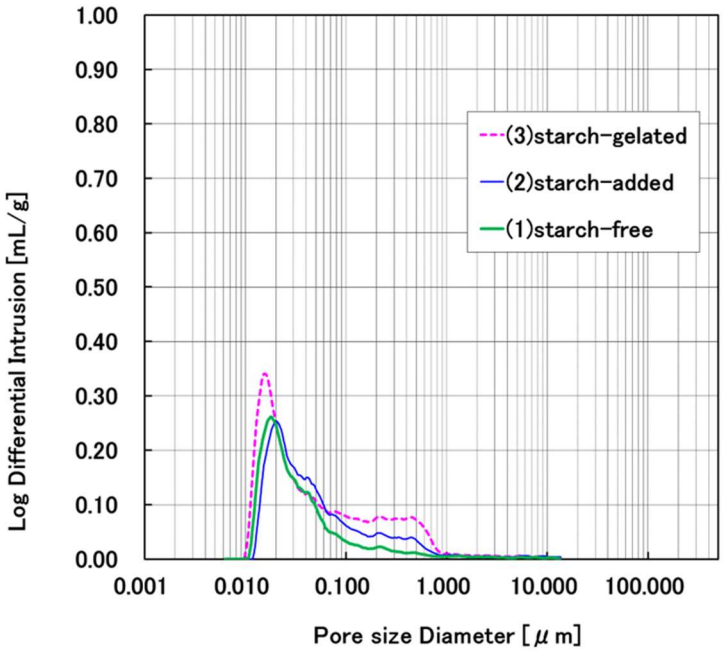

Figure 2.11. Pore size distribution of zeolite bulk bodies estimated from extrusion curves

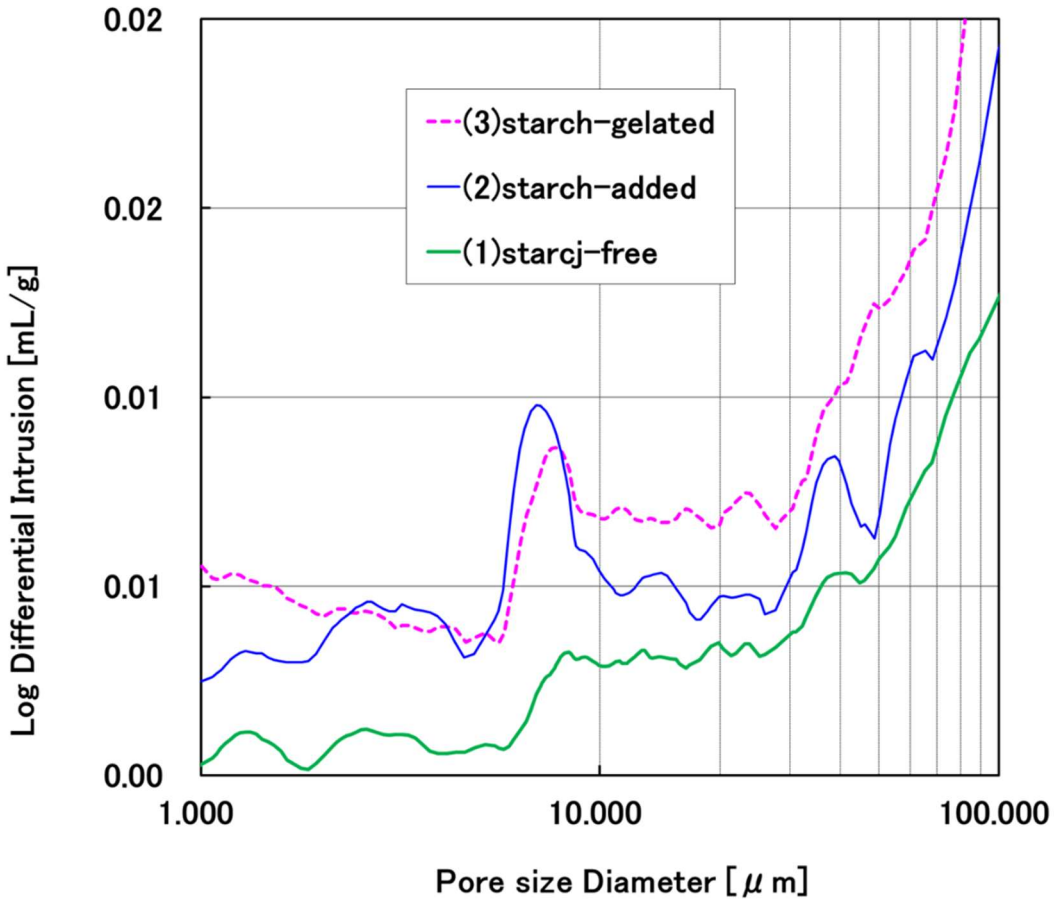

Figure 2.12. Pore size distribution of zeolite bulk bodies estimated from intrusion curves (Region of pore size:1-100μm)

2.4 Conclusions

Porous zeolite bulks were fabricated using starch as a pore-forming agent. An X-ray diffraction pattern indicated that the crystal structure of the starting ZSM-5 zeolite material was maintained in the bulk samples through all the processes, implying that the micropores in the zeolite crystal unit were maintained in the bulk bodies. The presence of micropores, mesopores, and macropores in the bulks was suggested by the adsorption / desorption isotherms of N_2 gas. The pore size distribution of the bulk samples had a peak at 7-9 nm, corresponding to mesopores which would be suitable for supporting functional nanoparticles. Changes in the macropore structure due to the starch heating process were confirmed from the cross-sectional images inside the samples observed by confocal laser fluorescence microscopy using the liquid immersion method. The three-dimensional images of the macropores created from the cross-sectional images had a higher resolution than from the industrial micro-X-ray computed tomography. This observation method can be applied to other porous materials by properly selecting the refractive index of the immersion liquid.

Chapter 3| Properties of zeolite bulk body

3.1 Introduction

In Chapter 3, the functional and mechanical properties of the zeolite bulk body described in chapter 2 were investigated. The compressive strength, water vapor adsorption properties, and gas permeability of the zeolite bulks were measured. These properties are important for applications in the separation and purification of gases and liquids and for environmental purification, and examined the relationship with the microstructure of the bulk body.

Today's homes in Japan are more airtight to save energy, but the air in the room tends to be very moist or very dry. In addition, the release and accumulation of formaldehyde and other harmful volatile organic compounds (VOCs) from man-made materials has created a new health-related problem known as the "sick building syndrome"[162-164]. To solve these problems, mesoporous materials with a humidity control capability have been developed. For example, Japanese Patent Application Laid-Open No. 2004-242848[165] mentioned a material obtained by a mixing and sintering method, consists of a main deodorizing component containing at least one of the metal hydroxides or metal oxides and a humidity control component made of inorganic materials. Through the joint research between the AIST group, which holds the patent, and the LIXIL Corporation (formerly the INAX Corporation), functional humidity control tiles have been developed and commercially sold [166, 167]. The tile is made from clay minerals, such as allophane, a hydrated aluminum silicate with a low crystallinity obtained from volcanic ash soil[168], contains mesopores of 1-10 nm, and indicates a higher humidity control performance than diatomite.

Zeolite is also mentioned as one of the humidity control materials, but it is not used as a raw material for the examples described in the patent. Zeolite is a crystalline aluminosilicate with micropores derived from the crystal structure having a high specific surface area, and is known to have excellent adsorption performance for water and volatile organic compounds. Therefore, the zeolite exhibits a deodorizing performance even as a single substance. However, it is difficult to obtain a solidified zeolite body with a sufficient strength for use as a structural material while maintaining the original crystal structure that can exhibit an adsorption performance, because the zeolite is difficult to sinter as a main component. Furthermore, zeolite in the powder form exhibits an adsorption performance, but doesn't exhibit a humidity control performance that releases water vapor when the relative pressure of the water vapor decreases[169].

The zeolite bulk body, which has a strength while maintaining the original adsorption function of the zeolite, may be applied as a structural material with a humidity control function. The compressive strength, water vapor adsorption isotherm, and gas permeability of the zeolite bulk body were measured and compared with the structure. The water vapor adsorption performance was also compared with previously reported literature materials.

3.2 Experimental Procedure

The properties of the three types of zeolite bulk bodies described in Chapter 2: (1) starch-free (sample without starch), (2) starch-added (sample with starch and no heat-treatment) and (3) starch-gelated (sample with starch and heat-treatment) were investigated.

The mechanical strength of the bulk bodies was evaluated by compressive strength tests using an autograph (AG-I, SHIMADZU, Corp.) based on Japanese industrial standards[170]. The samples were polished to a diameter of 12 mm and a height of 10 mm for the tests. Seven test pieces were used to measure the strength of each sample. The water adsorption characteristics of the raw zeolite powder and the zeolite bulk bodies were evaluated by adsorption /desorption isotherm measurement at 40°C using a surface area and pore distribution size analyzer (BELSORP-Ⅱ, MicrotracBEL) with a water vapor unit. The gas permeabilities of the samples were evaluated by a permeation membrane analyzer (PMA-601, SepraTek). A circular hole with a diameter of 6 mm was cut in the center of a round PET sheet with a diameter of 55 mm and a thickness of 110 μm. A sample with a diameter of 12 mm and a thickness of 2 mm was then fixed in the hole of the round PET sheet with epoxy resin. The sample fixed to the PET sheet was placed in the chamber of the analyzer. The amount of gas permeation per unit of time was measured by flowing 0.5 MPa of N_2 gas from one side of the sample as shown in Figure 3.1.

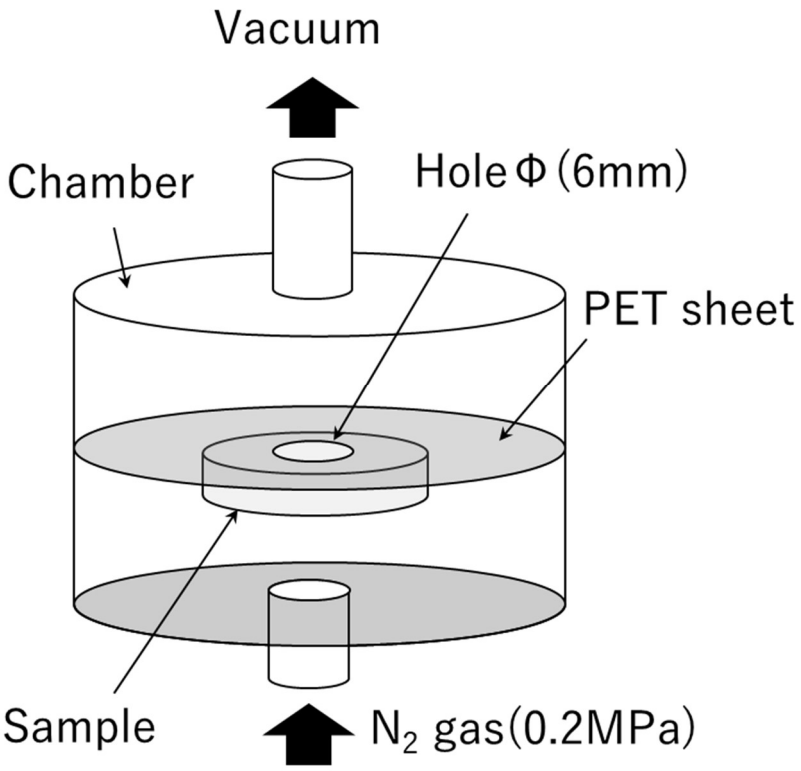

Figure 3.1. Schematic illustration of nitrogen gas permeability measurement

3.3 Results and Discussion

The compressive strength of the zeolite bulk bodies is shown in Figure 3.2. All the samples had a compressive strength above 25 MPa. The compressive strength of the bulks was more than that of general construction concrete which has a strength of 24 MPa[171]. When comparing the samples with different processes, the strength of the starch-free sample was the highest. According to the Weibull's weakest link theory[172] , the destruction of ceramics starts from the largest defect. Samples that used starch as a pore-forming agent had a lower strength because they contained macropores which acted as a starting point for the fracture.

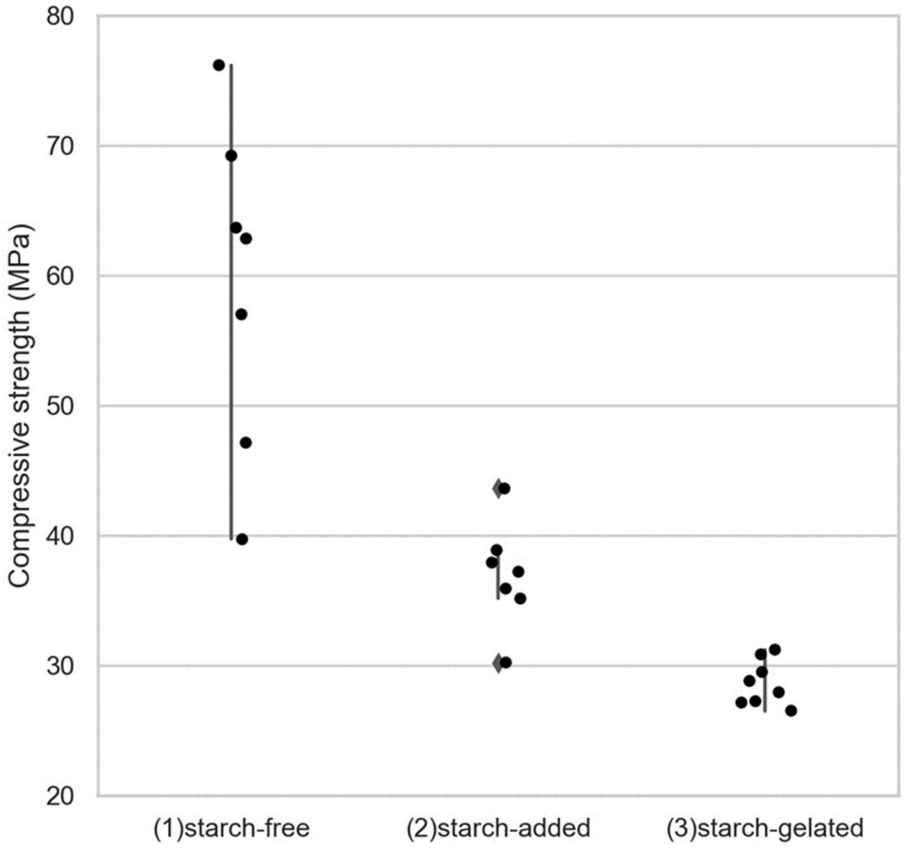

Figure 3.2. The compressive strength of the zeolite bulk bodies

Figure 3.3 shows the results of the adsorption/desorption isotherm of water. The x-axis is the relative humidity and the y-axis is the weight of water vapor adsorbed per weight of powder. For comparison, the adsorption isotherms of clay minerals measured by the INAX Corp. group is shown in Figure 3.4 [169]. In Figure 3.3, hysteresis curves that were not seen in the raw zeolite powder material were confirmed in the solidified bodies. It was also confirmed that the amount of water adsorbed in the high relative humidity was greater in the solidified bodies than in the raw zeolite powder material. This property indicates that the solidified bodies have an environmental humidity control performance. In particular, the steep increase in the slope at a high relative humidity and large hysteresis are excellent properties for humidity control. This means that the material tends to retain water, adsorbs more at a very high humidity, and slowly desorbs the retained water at a lower humidity. A comparison to the adsorption properties of clay minerals in Figure 3.4 shows that my bulk sample exhibits adsorption properties very similar to some clay minerals, which are different from conventional zeolites. Although the measurement temperature is different, the adsorption capacity of my samples is equal to or greater than previous reports because the adsorption isobaric lines generally show that the adsorption capacity decreases as the temperature increases. In their literature, clays with a high adsorption capacity are mentioned as containing large amounts of mesopores. It is noteworthy that the amount of water vapor adsorption varied between the samples in which the pore structure was modified by starch addition and the gelation process. It was confirmed that the amount of water vapor adsorbed was the highest in the (3) starch-gelated sample in which the pore networks were formed by the addition of starch and the heat treatment in steam at 80 °C. In the bulk sample for which the hysteresis curve was observed, it is considered that water was adsorbed on the

mesopores, like N_2 adsorption. According to Figure 2.6 in Section 2 and Figure 3.3, samples with more mesopores actually also adsorb more water vapor.

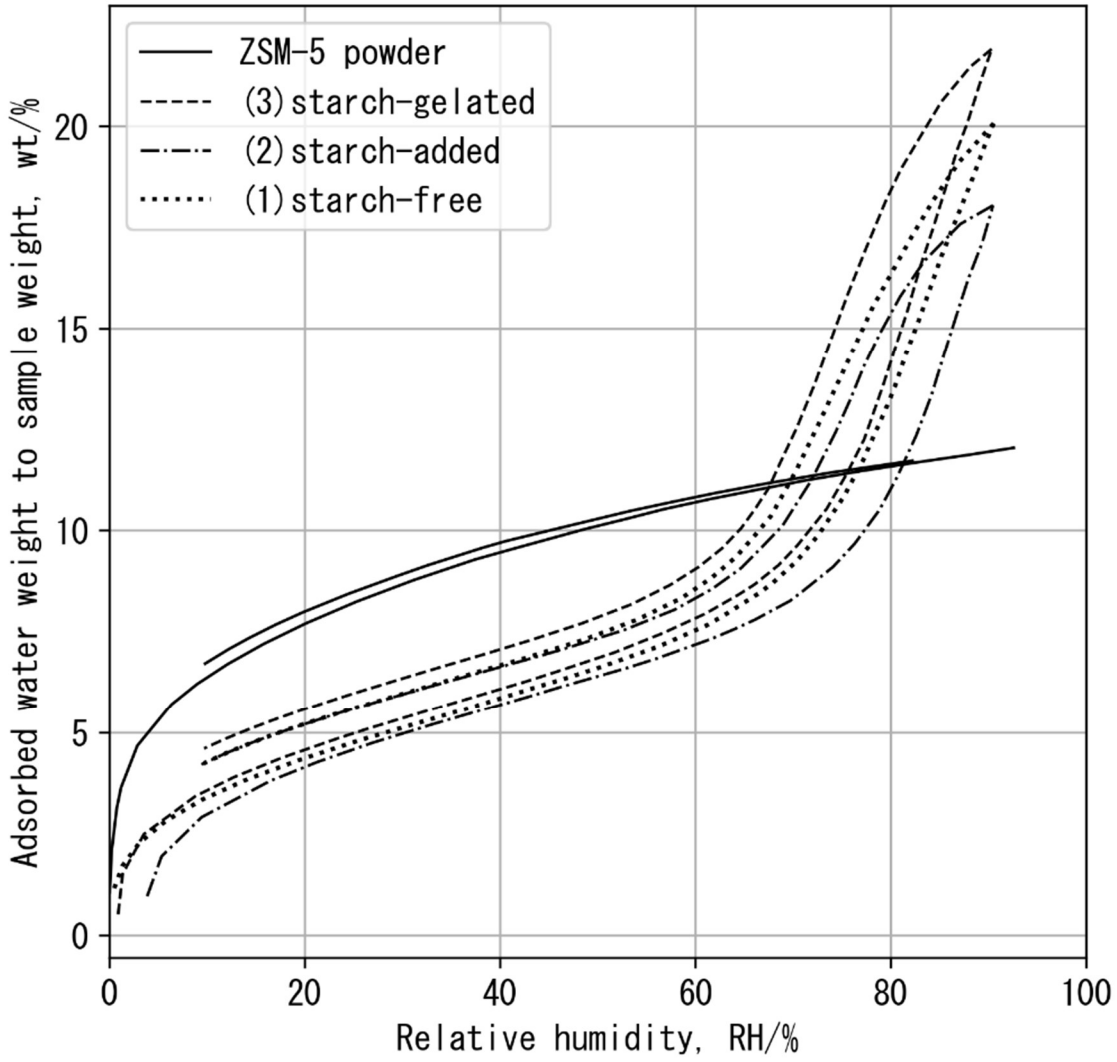

Figure 3.3. H_2O vapor Adsorption/ Desorption isotherm at 40℃

Mining area of each ceramic powder and minerals contained in each powder

(Ceramic powder)		(Area)産地	(Minerals) 構成鉱物
Zeolite	ゼオライト	秋田県	Mordenite, Quartz
Allophane	アロフェン	栃木県鹿沼市	Allophane, Albite, Orthoclase, Quartz
Sepiolite	セピオライト	スペイン	Sepiolite
Diatomite	珪藻土	北海道稚内市	Cristobalite, Albite, Quartz, Sericite
Halloysite	ハロイサイト	中国貴州省	Halloysite

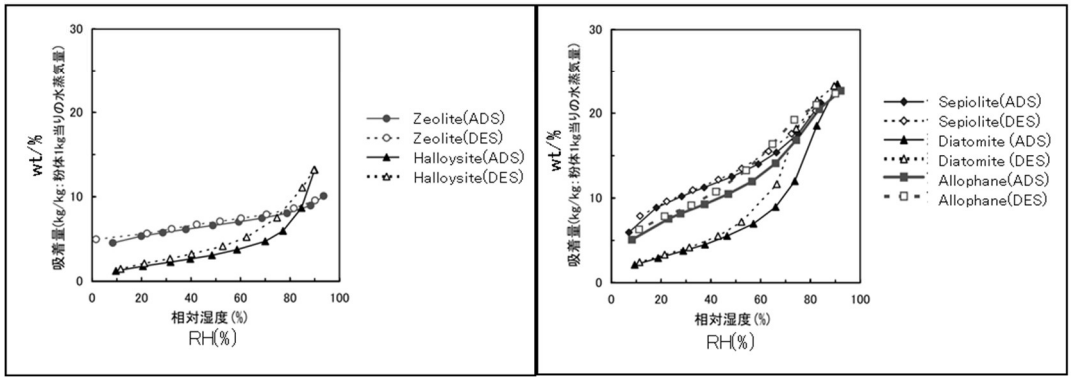

Figure 3.4. Adsorption isotherm for moisture in ceramic powder at 25℃ (modified from [169])

Figure 3.5 shows the N_2 gas permeability of the bulk bodies. The samples had almost no gas permeability as a filter considering the velocity of the carrier gas generally used in gas chromatography is set to about 30 cm/s[173]. The starch-gelated sample showed the highest gas permeability among the three, although the starch-gelated and the starch-added sample indicated almost the same porosity based on Archimedes' method. The differences occurred due to the pore structure. The CLFM observation results showed that isolated macropores as large as the starch grains were formed in the sample with the ungelated starch. The isolated macropores did not contribute to the gas permeability. Spherical pores derived from the starch irregularly expanded in the gelated sample to form a network structure. The increase in the connected structure pores resulted in an increased gas permeation in the sample containing the gelated starch.

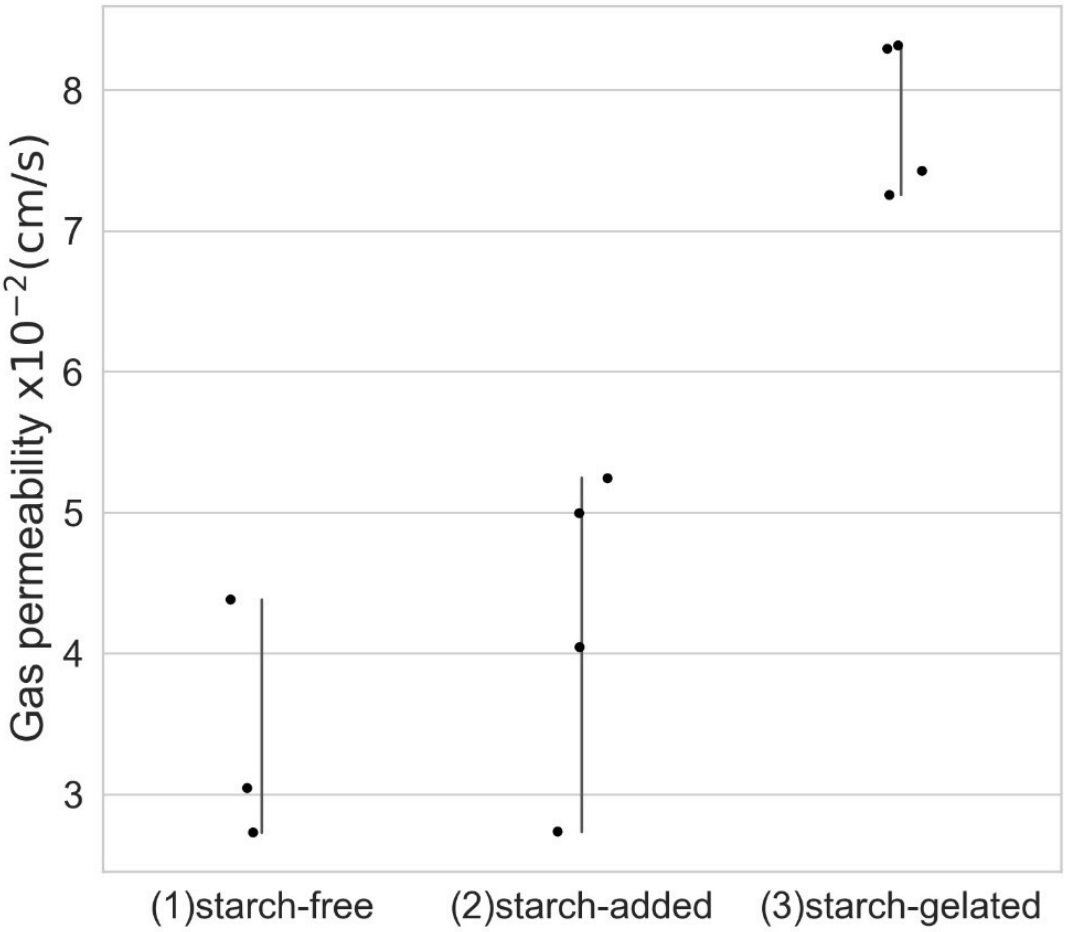

Figure 3.5. N_2 gas permeation rate of the bulks

3.4 Conclusions

The compressive strength of the zeolite bulk bodies was above 25 MPa, which was higher than the that of general concrete used for construction. This result showed that the bulk bodies had *a* sufficient mechanical strength for handling. The zeolite bulks exhibited water vapor adsorption properties similar to those of clay minerals unlike the zeolite powders. It was confirmed that the amount of adsorbed water vapor was the highest in the sample in which a pore network was formed by starch gelation. It was suggested that the adsorption properties could be controlled by the process. The starch-gelated sample showed the highest gas permeability among the three indicating that the starch networks as pore-forming agents are available to create continuous pore structures for a smooth gas flow.

Chapter 4 | Fabrication of Porous Hydroxyapatite

4.1 Introduction

Lack of safe water is a great issue for public health around the world. According to the WHO report, 771 million people lack even a basic drinking-water service, including 122 million people who are dependent on surface water in 2020[174]. Contaminated water can transmit diseases such diarrhoea, cholera, dysentery, typhoid, and polio[175]. Even in developed countries with centralized water treatment facilities, water pollution by microbes is one of the great threats to public health[176]. There are concerns about the aggravation of water problems due to global population growth, climate change, natural disasters, and the aging social infrastructure. PoU (point of use) water treatment technology is useful in areas where it is difficult to maintain a water distribution system.

Activated carbon has been widely used as PoU filtering medium to purify water [177]. The filter medium absorbs various harmful substances by physical adsorption due to its high specific surface area. It is a disposable material that is difficult to recycle as an adsorbent. Activated carbon has the function of decomposing chlorine by a catalytic reaction and is often used for the treatment of water that has already been disinfected with chlorine [178]. Another example of a practical filter is a hollow fiber membrane, which is an organic polymer-based filter [65, 176]. As an inorganic material filter, a tubular ceramic membrane is also known [61, 66]. These two types of filters remove harmful substances by passing water through submicron-sized pores. The substance that can be removed depends on the physical pore size of the filter. Bacteria can be removed by submicron-sized pores, but viruses of several nanometers cannot be removed by pore-size-dependent isolation processes. Ingenuity for disinfection needs to be added to the

filter[134]. As the pore size decreases, a higher pressure is required to allow water to pass through the pores.

The hydroxyapatite (HAp) porous material has a high potential as a material for water purification filters. HAp has a hexagonal crystal structure with two major crystal planes; the *a*-plane and *c*-plane. The *a*-plane is positively charged and the surface of a virus is mainly negatively charged. By using HAp crystals with a significantly exposed *a*-plane as a filter, viruses can be removed with a high efficiency by utilizing electrostatic attraction. In addition, HAp is a biomaterial ceramic that is highly safe for the human body and can be reused by heat treatment. In this study, fabrication of the HAp porous body with positively charged *a*-plane exposure and continuous pore structure was attempted. To expose the positive sites, rodlike HAp particles, which have a large surface area of *a*-planes, were used as the raw materials.

Starch was selected as a pore-forming agent utilizing its properties called gelatinization and retrogradation in which starch particles formed a self-network structure by heat treatment. The properties of starch are appropriate to form a networked porous structure. Starch is also a natural polymer and is promising for process design with less impact on the environment. Furthermore, a freeze casting method was used to achieve a high porosity of the sample[120].

A three-dimensional observation method combining a confocal laser scanning microscope and an immersion translucency method was applied for the evaluation of the networked structure. The method can be applied to single-composition ceramics with open pores if the immersion liquid to make the sample transparent is available. An immersion liquid suitable for HAp was selected, and observations were attempted.

4.2 Experimental Procedure

Commercially-available rodlike hydroxyapatite powder, which has a particle size diameter from 0.15 to 0.30 μm and length from 1.0 to 1.5 m. (HAP-200, Taihei Chemical Industrial Co., Ltd.) was selected as the starting material. Figure 4.1 shows an SEM image of the HAp raw powder. The powder was dispersed in distilled water with 1.5 mass% ammonium polyacrylate (A-30SL, Toagosei Co., Ltd.) and 4 mass% poly-vinyl alcohol (Japan Vam & Poval Co., Ltd.) based on the powder weight as the dispersant and the binder, respectively. An aqueous slurry with a solid loading of 12 vol% was prepared by ball milling for 24 hours. Rice starch powder with a diameter of 2.0 ~8.0 μm (Sigma-Aldrich Co. LLC) as a pore-forming agent was added to the slurry and dispersed using an ultrasonic homogenizer. The slurry was then cast into an acrylic mold with a 26-mm diameter and heated in steam at 80 ℃ for 30 minutes to gelatinize the starch. For comparison, the slurry without heat treatment was also cast. The slurries were one-directionally frozen from the bottom of the mold with liquid nitrogen. The frozen compacts were freeze-dried under a reduced pressure of 10 Pa for 48 hours. The dried samples were degreased at 500 ℃ for 5 hours, then sintered at 1200℃ for 12 hours to fabricate the porous bodies of hydroxyapatite.

The crystal structures of the raw HAp powder and the bulk samples were identified by an X-ray powder diffraction measurement (Miniflex600, Rigaku) with CuKα radiation. Fracture surface observations were performed by scanning electron microscopy (SEM). Samples were observed in the direction parallel to the cooling direction during the freeze-dry molding. The internal structures of the samples were observed by a confocal scanning laser fluorescence microscope (CLFM) using the immersion transmission method. The method of observing the internal structure of ceramic green bodies was applied to the

HAp porous bodies [10, 11]. As the immersion liquid, 1-bromonaphthalene (n = 1.66)[158] that has a refractive index, n, close to that of hydroxyapatite (n = 1.63-1.64) [179] was used to reduce light scattering at the interface between the pores and the matrix. The fluorescent agent, Rhodamine B, was dissolved in the immersion liquid, then the liquid was allowed to permeate into the slices of the samples having a thickness of 200-500 μm. The sliced samples were observed from the surface to the depth of 52 μm, and 180 images were obtained at intervals of 0.29 μm. The images were stacked to create a three-dimensional image after image processing to separate the matrix and pores. Finally, the density was measured by Archimedes' method. Five test pieces were used to measure the density of each sample.

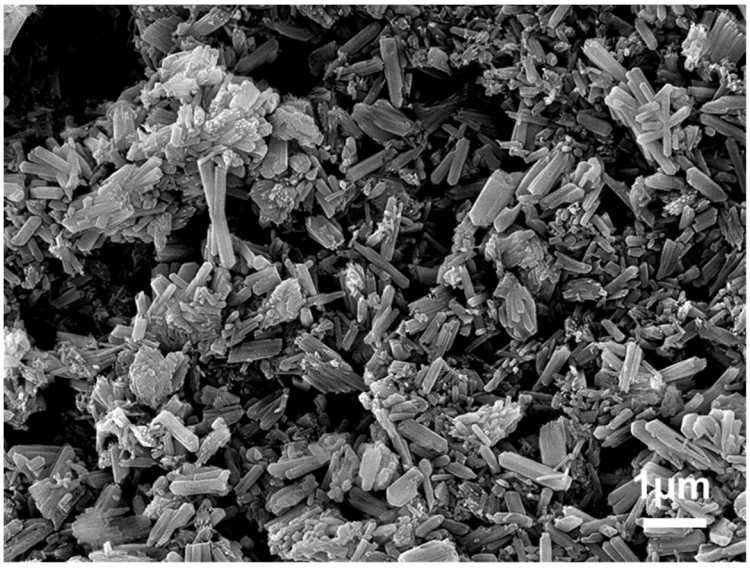

Figure 4.1. SEM image of the HAp raw powder

4.3 Results and Discussion

The carbon component of the starch was removed by a sufficiently long sintering time, and white bulk samples were obtained. X-ray diffraction patterns of the raw HAp powder and the porous bodies degreased at 500 ℃ for 5 hours, then sintered at 1050-1300℃ for 12 hours are shown in Figure 4.2. The bulk sample peak was identified as the HAp phase, with no decomposition or formation of other components confirmed at 1050-1300°C. Figure 4.3 shows the fracture surface of the porous hydroxyapatite observed by SEM. The vertical direction of the photos is the freezing direction. Figure 4.3 (a) and 4.3 (b) show the fracture surface of the samples with heat treatment at 80 ℃ and untreated, respectively. Three-dimensionally connected pores of about 5 μm with a low anisotropy were observed in Figure 4.3(a). On the other hand, elongated pores parallel to the freezing direction were confirmed in Figure 4.3(b). The elongated pores are derived from ice crystals grown in the uniaxial direction. Fukushima et al. reported the production of porous ceramics with a controlled pore structure by ice crystals[120]. The structure of the sample in which the starch network was formed was not affected by the freezing direction of the water.

Figure 4.4 (a1) and (a2) are cross-sectional images in the sample obtained at a depth of about 20 μm from the surface; the vertical direction of the images is the freezing direction. The structures similar to the fracture surface observed by SEM were confirmed. Since Figure 4.4 (a1) and (a2) are images optically cut from the confocal surface of the microscope, the observed surface is not affected by the roughness caused by the fracture. Figure 4.4 (b1) and (b2) are images of the YZ-plane of the samples created by stacking of the XY-plane observation images. The observation images taken at a greater depth position became darker. To reduce the influence of the image brightness on the image

analysis, 512 images of the YZ-plane were used. The YZ plane images were binarized by determining the matrix and the pore region using trainable Weka Segmentation[180] which is a machine learning technique. Figure 4.4 (c1) and (c2) show examples of the binarized images, and Figure 4.4 (d1) and (d2) show the Fourier transform images of each binarized image. The horizontal line in the center of Figure 4.4 (d2) means that the binarized images inside the sample without heat treatment had a lateral periodic structure. In fact, anisotropy due to the freezing direction was confirmed in Figure 4.4 (c2). Figure 4.4 (e1) and (e2) show three-dimensional images created by stacking the binarized images. The porosities of the samples estimated from Figure 4.4 (e1) and (e2) were 67% and 65%, respectively. The average porosity obtained from the results of the Archimedes density measurement was 72% and 73% for the samples with and without heat treatment, respectively. The standard deviations of the porosity were 1.5 for both samples. The porosity did not change with the heating of the starch, but the porosity estimated from the 3D image was lower than the actual porosity because the pores with a pixel size of less than 0.29 μm were not imaged by the CLFM. The samples have a sufficiently high porosity as a filter.

Zhang et al. reported fabrication of an HAp membrane and its performance for separating Au nanoparticles from a suspension[181]. In the report, they used the same commercially-available HAp powder that I used and succeeded in separating the negatively charged Au nanoparticles that were used as an alternative to the virus. My samples have structures influenced by both the starch networks and ice crystals. By combining these two factors in this way, it may be possible to control a more complex network structure of pores.

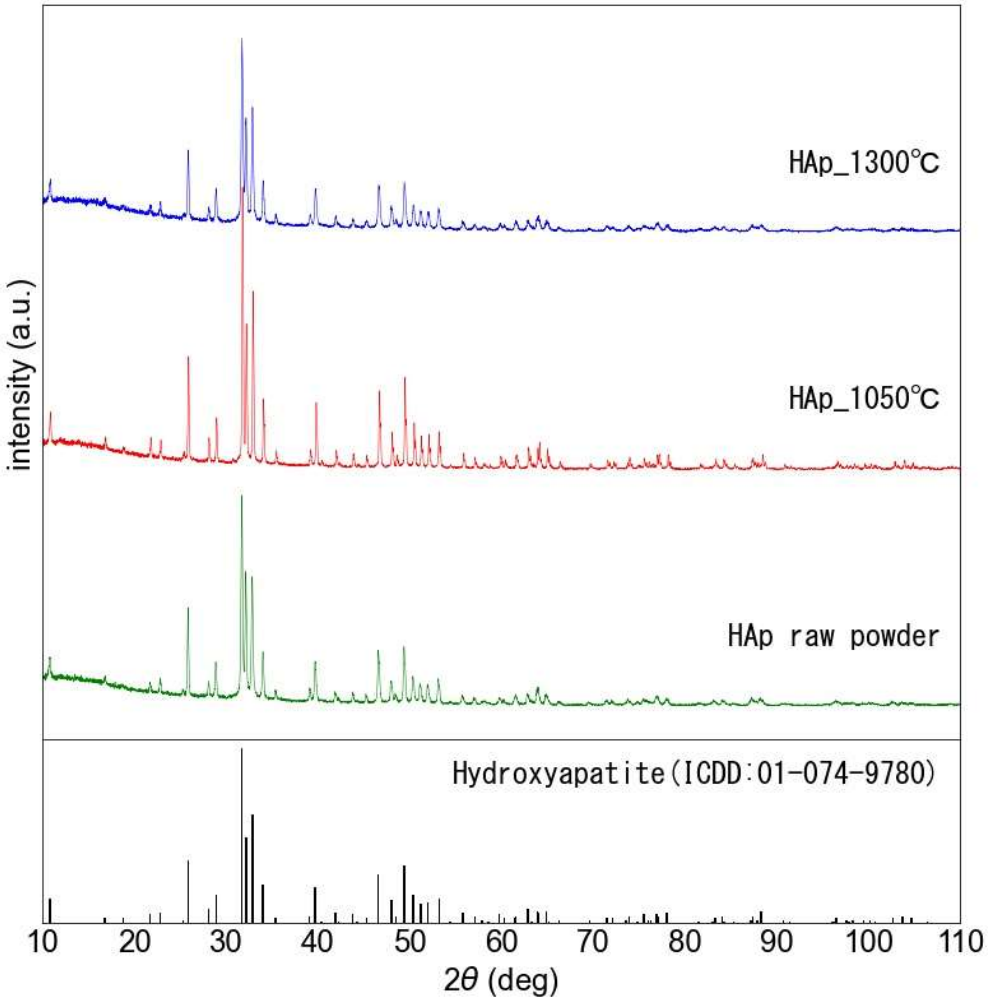

Figure 4.2. X-ray diffraction patterns of raw HAp powder and the porous bodies

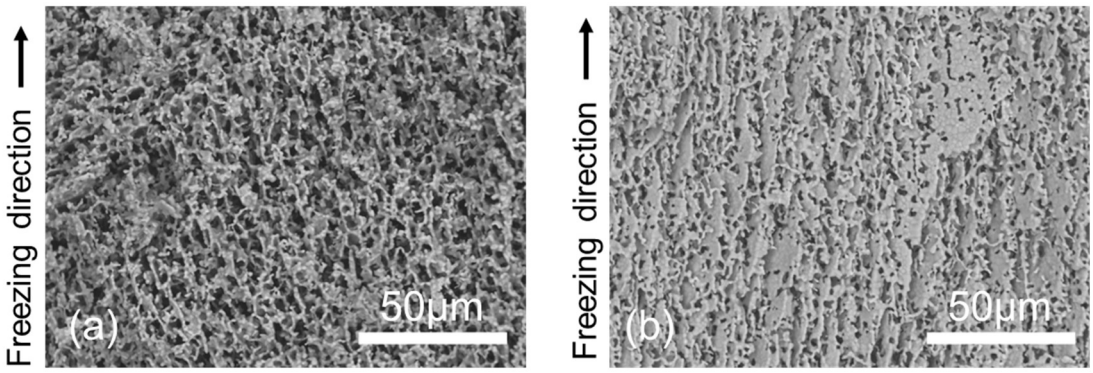

Figure 4.3. Fracture surface of the porous hydroxyapatite observed by SEM

(a)with heat treatment at 80 °C and (b) untreated

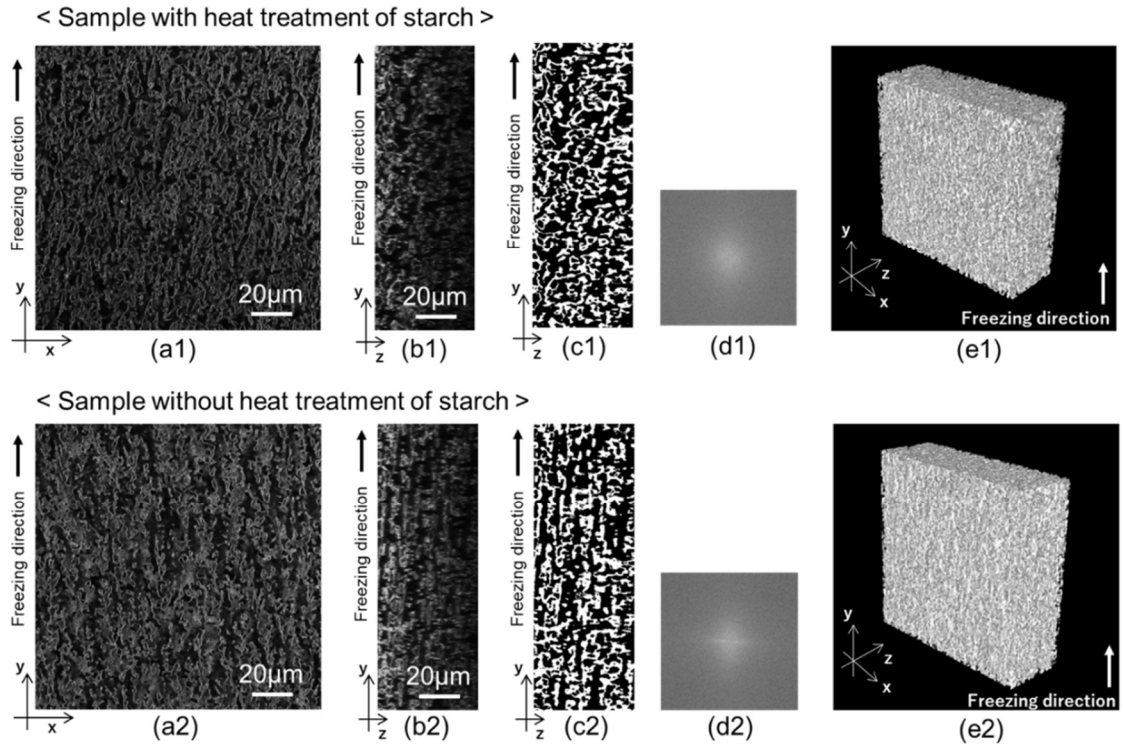

Figure 4.4. (a1, a2) Cross-sectional images of the hydroxyapatite porous body observed by CLFM, (b1, b2) YZ-plane images, (c1, c2) binarized YZ plane images, (d1, d2) Fast Fourier Transform images of binarized YZ-plane images, and (e1, e2) Three-dimensional images created by stacking the cross-sectional observation images.

4.4 Conclusions

Rice starch powder formed a network structure by the process of gelatinization and retrogradation. Subsequent sintering removed the starch, a pore-forming agent, resulting in the formation of a porous body with connecting pores. In the sintered body, pores derived from the starch networks were observed.

Chapter 5 | Characterization of porous hydroxyapatite

5.1 Introduction

In Chapter 5, the water purification performance of the hydroxyapatite porous material is described. Porous ceramics have already been put to practical use as filters for water purification, and removal of bacteria from water using porous filters has been previously reported. However, the removal of microorganisms by a ceramic porous body is based on the physical sieving effect of the pores. Therefore, it is generally difficult to remove viruses with a ceramic porous body having pores larger than the size of the viruses. An ultrafiltration membrane or nanomembrane filter is required for a virus [182]. Time period for filtration increases if the particles to remove are finer. Efficient filters can be designed by utilizing the electrochemical properties of the surface of the filter material.

Porous HAp was produced by the freeze-drying method and its structure was evaluated in previous chapter. The porous body had a high porosity of more than 70% and having continuous porous structure. However, it could not be used for the filtration test due to its cracking and brittleness, thus the fabrication process of the porous body was changed. A slip-casting process was adopted in which the concentration of the starting material in the ceramic slurry was increased. To maintain the porous structure with the rod-like powder shape, the grain growth during sintering must be minimized. On the other hand, if the sintering does not progress at all, the strength will decrease and the porous body will break during the filter test. It is necessary to promote necking of the particles to some extent. The partial sintering described in Section 1.3 is incorporated into the fabrication process of the pore structure. A hierarchically porous material with submicron pores created by partial sintering, larger macropores derived

from starch pore-forming agent and surface potential of the HAp was used for the filtration test. First, Escherichia coli (E. coli) was used for the test, then the human coronavirus was used. The concentration of the microorganisms contained in the buffer solution before and after filtration was confirmed to verify the performance of the ceramic porous body as a filter.

5.2 Experimental Procedure

Commercially-available rodlike hydroxyapatite powder, which has a particle size diameter from 0.15 to 0.30 μm and length from 1.0 to 1.5 μm (HAP-200, Taihei Chemical Industrial Co., Ltd.) was dispersed in distilled water with 2 wt% polyethyleneimine (EPOMIN SP-200, Nippon Shokubai Co., Ltd.) based on the powder weight as a dispersant. An aqueous slurry with a solid loading of 40 vol% was prepared by ball milling for 24 hours using a polyethylene bottle and a zirconia ball medium (2-10 mm diameter). Corn starch powder (Nihon Shokuhin Kako Co.,Ltd.) as a pore-forming agent was added to the slurry in the amount of 40 wt% vs. the powder contents in the slurry. The starch was mixed and dispersed in the slurry using a planetary centrifugal mixer (ARE-310, THINKY Corp., Japan) at 2000 rpm for 5 minutes. The slurry was cast into acrylic molds with a 35-mm diameter and steamed in water vapor at 90 ℃ for 20 minutes to gelatinize the starch. After the heat treatment, the cast bodies were dried at room temperature for 10 days. The dried green bodies were de-starched at 500°C for 5 hours, then sintered at 1050°C for 3 hours. A disk-shaped porous ceramic sample was obtained.

The shrinkage rate after sintering was calculated from the diameter of the samples. The density of the samples was measured by Archimedes' method using kerosene as the solvent. More than 2 test pieces were used for density measurement per each sample. The microstructure of the samples was observed by scanning electron microscopy and confocal laser fluorescent microscopy along with the liquid immersion method using 1-bromonaphthalene as the immersion liquid.

Figure 5.1 shows the filtration test apparatus for the porous ceramics. The ceramic samples washed with distilled water were dried in an oven of 60℃ for one day, and the sample surface was covered with parafilm (PM-996, Bemis Manufacturing Company). The sample was then placed in the center of a plastic mold and PDMS (SYLGARD TM 184, The DOW Chemical Company) was poured into the mold. After curing the PDMS in an oven at 60°C for one day, the parafilm on the sample top and bottom was cut off. The PDMS-sealed samples were fixed on glass suction filters after sterilization in an autoclave. The inside of the sample was washed with sterilized water before the filtration test. A 5-ml aliquot of sterilized water was poured on the sample top and suctioned by vacuum. The starting time and end time of the suction was recorded. The washing operation was repeated three times. The cloudy water in the suction bottle was removed with a pipette.

E. coli was used for the bacteria removal filtration test. A buffer containing E. coli with an OD600 of 0.3 was prepared and further diluted 10-fold with the buffer. OD600 is a common absorbance index for evaluating the concentration of bacterial cultures[183]. The procedure of pouring and suction of the 5-ml buffer solution containing E. coli onto the sample was repeated four times. The time period required to filter each 5 ml sample was recorded. The filtered liquid was pipetted from the suction bottle each time. The buffer solution before filtration and the liquid after filtration were diluted in a power of 10 from 0 to 10^6. The area of the agar medium in the sterilized petri dish was divided into 6 areas, and 9 points of the diluted solution were dropped on each area. The petri dishes were kept in a constant temperature oven at 60° C for one day, and the presence of E. coli in the buffer solution was confirmed by the bacterial colonies cultured on the agar medium.

Human strains of coronavirus 229E[184] were used for the viral removal filtration test. As viruses cannot be cultured in buffers or agar media, the preparation methods must be different from bacteria. Human liver cancer cells (Huh7:[185]) were used for the virus culture. A 229E viral solution (~10^5 viral particles/ ml) in phosphate-buffered saline (PBS buffer) was prepared. The viral solution (5 ml) was then placed on the top of the ceramic sample and vacuumed the same as the bacteria filtration test. The buffer solutions before and after filtration were serially diluted, Huh7 cells in the wells were infected, and incubated for 4-6 days. The tissue culture infective dose was used for determination of the viral particles concentration assay (TCID50 assay[186]). The broth was discarded from each well and rinsed with 1×PBS buffer. A 100-µl sample of 2.5% paraformaldehyde was added to the PBS buffer and incubated overnight at 4°C. After incubation, the buffer was removed and stained with 50 µl of DAPI stain for 30 minutes in the dark. Viable cells observed in blue and virus-infected dead cells were counted using a fluorescence microscope (EVOS imaging system) with a DAPI filter. Based on the number of the cells, the percent reduction and log reduction of the cells were characterized by formulas 1 and 2, and the effect of virus removal was evaluated.

$$(\text{Percent Reduction}) = (A - B) \times 100 / A \qquad \text{—formula 1}$$

$$(\text{Log Reduction}) = \log_{10}(A) - \log_{10}(B) \qquad \text{—formula 2}$$

where A is the number of viable microorganisms before treatment, and B is the number of viable microorganisms after treatment.

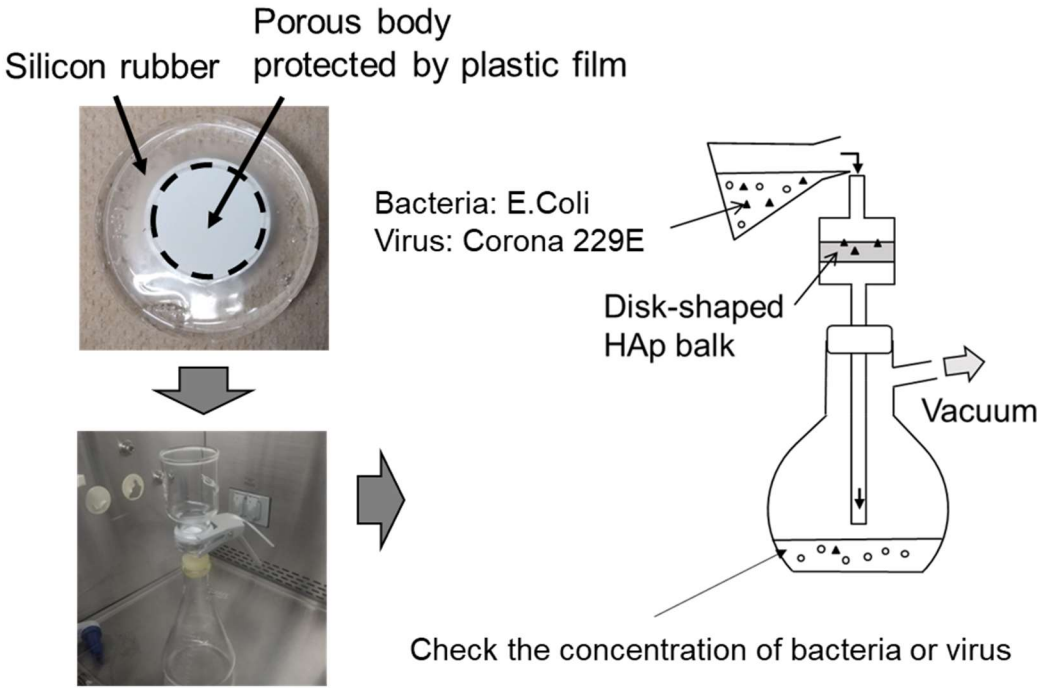

Figure 5.1. Filtration test apparatus for porous ceramics

5.3 Results and Discussion

A white disk-shaped porous body with a diameter of 30 mm and a height of 5 mm was obtained. The shrinkage rate after sintering was 8-10%. Density measurements by the Archimedes method indicated that the porosity of the sample was 57-59%. Although the porosity was lower than that of the HAp porous body prepared in Chapter 4, cracks were not observed on the surface. A suitable sample for the filtration test was thus obtained.

Figure 5.2 shows the microstructure of the sample observed by scanning electron microscopy. Spherical pores with a size of about 10 μm are pores produced from the starch pore-forming agent. Based on observations at a higher magnification, the necking structure between the HAp particles was confirmed. Submicron-sized pores existed around the particles. Figure 5.3 shows the results of three-dimensional observations of the porous HAp. A shell-like structure was observed around the pores. The structure may formed from hydroxyapatite particles incorporated into the surface of the starch pore-forming agent. The same structure was confirmed in the observations of the fracture surface by SEM. The pores formed by starch were connected according to the three-dimensional observations.

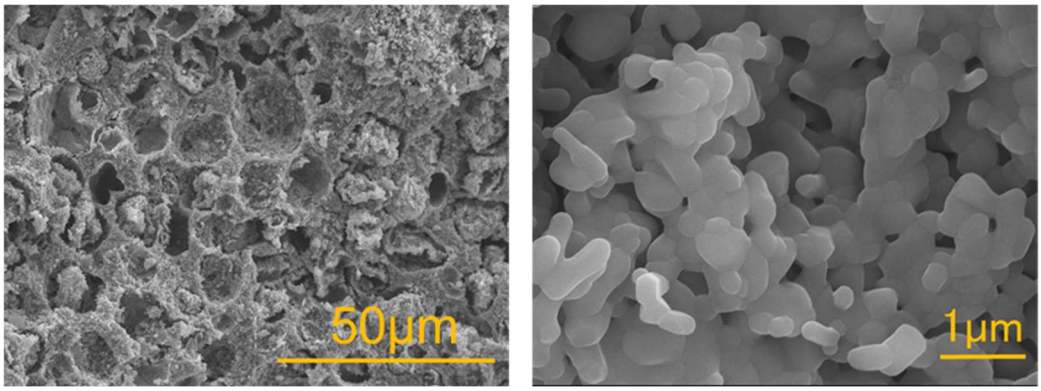

Figure 5.2. Microstructure of the porous HAp observed by scanning electron microscopy

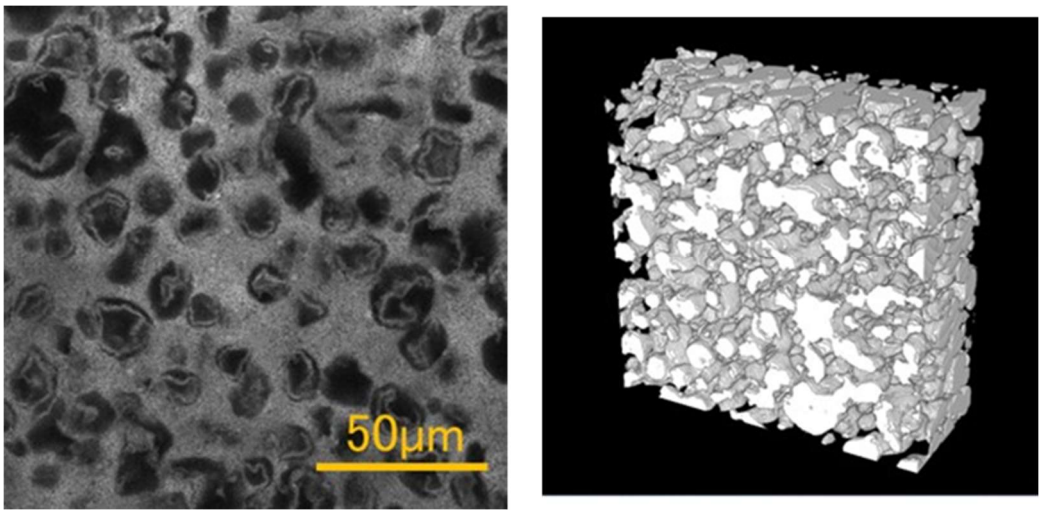

Figure 5.3. Three-dimensional structure of the porous HAp observed by confocal laser fluorescent microscopy using liquid immersion method

Figure 5.4 shows the results of the bacteria removal test. It took approximately 8-12 minutes for filtration of the 5-ml buffer. Colonies of E. coli were confirmed in the petri dish in which the buffer solution before filtration was cultured. On the other hand, no colony of E. coli was observed in the petri dishes in which the solution after filtration were cultured. E. coli is an elongated bacterium with a length of 20 μm and a diameter of about 5 μm [187]. The E. coli was physically removed considering the observed pore structure and pore size of the porous body. The filtration test process worked and the porous body was available to remove the E. coli.

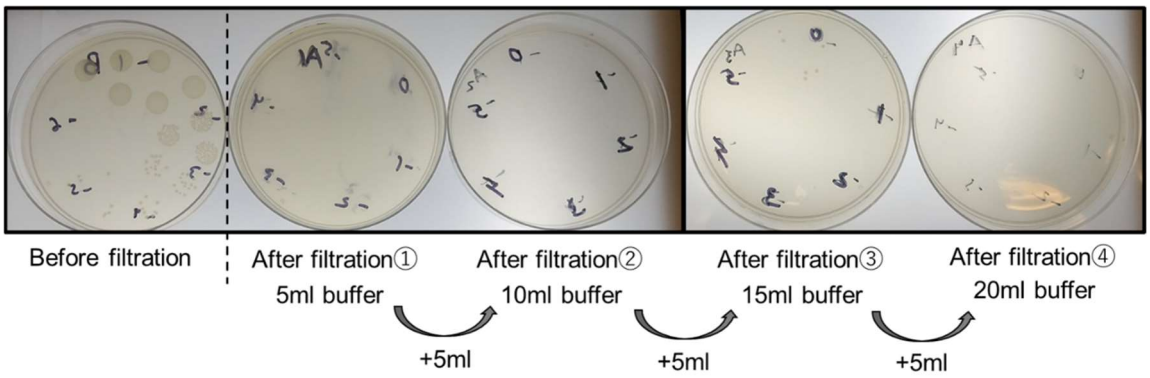

Figure 5.4. Cultured bacteria colony using buffer solution before and after filtration

Table 5.1 shows the reduction rate of the virus by filtration. The buffer solution before filtration contained viruses, but the solution after filtration did not contain any, confirming the very high removal performance of 99.998%. The size of the human coronavirus is about 0.1-0.2 μm[184] and considering the pore structure of the porous body, physical removal of the virus is difficult. However, a high removal rate was confirmed. It could be explained that the virus was electrochemically adsorbed on the surface of the hydroxyapatite and removed. Verification tests are necessary in the future since the number of tests is currently one.

Table 5.1. Reduction rate of the virus by filtration

	Viral solution	Filtrate #1	Filtrate #2
	1.8×10^5	3.16	3.16
+sd	2.5×10^5	0.0	0.0
-sd	1.4×10^5	0.0	0.0
Log	5.3	0.5	0.5
Log reduction		**4.8**	**4.8**
% reduction		**99.998**	**99.998**

5.4 Conclusions

The filtration performance of porous HAp was verified by the test to remove bacteria and viruses from the contaminated liquid A buffer solution containing E. coli at a concentration of 2.4×10^{7} cells/ml filtered by suction four times, in succession at 5 ml, and it was confirmed that the filtrate contained no detectable concentration of E. coli. In addition, a buffer solution containing human coronavirus 229E at a virus infectious titer of 1.8×10^{5} TCID50/ml was filtered twice in succession at 5 ml each time, and 99.998% of the virus was removed. These results indicated the applicability of the hydroxyapatite porous material as a polluted water purification filter.

Chapter 6 | Summary

Porous materials are used in a broad field such as the environment, energy, optics, medicine, and electronics. In recent years, there are high expectations for porous materials that will contribute to solving environmental problems associated with global warming. The sophistication of the pore structure control technology is becoming more and more important. Polymer beads, carbon, starch, etc., have been used as pore-forming agents for forming macropores using sacrificial fugitives, which is a process that has been widely used in the manufacture of porous ceramics. Generally, pores were introduced into the porous material using the initial shape of the pore-forming agent particles as a template. In this research, the starch properties called gelatinization and retrogradation were focused on, in which starch self-forms a three-dimensional network structure by heating and cooling with water. A new process for producing porous bodies using the networked starch as a pore-forming agent were developed. In addition, it was demonstrated that the network structure can be changed by adjusting the process, such as the heat treatment method, and that the macropore structure of the ceramic porous material can be controlled. In this study, zeolite, which has micropores derived from the crystal structure, and hydroxyapatite, which has different surface potentials depending on the crystal orientation, were selected as raw materials for the porous ceramics. It was clarified that these porous materials exhibit new functions derived from the pore structure. Furthermore, for a structural characterization of the connected macropores, a three-dimensional observation method of the internal structure of the ceramics using a confocal laser fluorescence microscope and a liquid immersion method were proposed. The liquid immersion method is a technique that enables transmission observation of the inside of a porous body by impregnating a porous body sample with a liquid having

the same refractive index as the raw material. The three-dimensional structure of macropores, which was difficult to evaluate by conventional techniques, could be evaluated by this three-dimensional observation method.

Chapter 1

The position of this research on the application of ceramic porous bodies was shown, and the research purpose of this paper was described.

Chapter 2

Zeolite bulk bodies were fabricated using zeolite powder, which is a typical microporous material as a raw material, and the relationship between the fabrication process and the internal structure of the porous body was verified. ZSM-5, which is widely used in industry, was selected as the zeolite raw material. Since zeolites are decomposed at high temperatures, they are generally difficult to form a bulk body by sintering, and are usually synthesized as nano- to micron-sized crystalline powders by a hydrothermal method. Therefore, the zeolite synthesis process using high-pressure steam, called the dry gel conversion method, was applied to make the bulk body. Starch powder was used as the pore-forming agent and colloidal silica was used as the binder. Bulk bodies were produced after the treatment in hot steam and degreasing treatment at 450°C for 24 hours. The microstructure of the bulk bodies was characterized by X-ray diffraction measurements, nitrogen gas adsorption, mercury porosimetry, fracture surface observations by scanning electron microscopy, and three-dimensional observation by confocal laser fluorescence microscopy with the liquid immersion method.

The prepared bulk body maintained the crystal structure of the ZSM-5 zeolite and had mesopores and macropores. In addition, the macropore structure was changed by the heat treatment process for the gelation of starch. It was clarified that the three-dimensional observation method of the internal structure used in this study can be applied to zeolite bulk bodies, and that the pore structure can be controlled by the process of heat treatment to make a network structure of the pore-forming agent.

Chapter 3

The properties of the zeolite bulk body prepared in the previous chapter were investigated. The compressive strength, water vapor adsorption properties, and gas permeability, which are important for applications in the separation and purification of gases and liquids and for environmental purification, were characterized. The relationship between the properties and microstructure of the bulk body were evaluated. The fabricated bulk bodies were confirmed to have a compressive strength of more than 25 MPa, which is about the same as general concrete (18-24 MPa), and it was shown that they have a potential for practical use based on their strength. In addition, a hysteresis curve, which is not seen in the raw zeolite powder, appears in the adsorption isotherm of water vapor with the bulk bodies. In the sample with an improved macropore connectivity by changing the heat treatment method, the improvement of nitrogen gas permeability was confirmed, demonstrating that the characteristics can be changed by controlling the pore structure in this study. The results indicated the potential of the process using the starch as a pore forming agent to control the properties such as water adsorption and permiability.

Chapter 4

The preparation process of the porous materials using starch as a pore-forming agent and the three-dimensional observation method by confocal laser fluorescence microscopy were applied to the hydroxyapatite porous material. The purpose of this chapter is to describe how to produce porous ceramics for contaminated water treatment using the anisotropy of the surface potential of the hydroxyapatite crystal planes. Hydroxyapatite porous bodies were produced, and their three-dimensional structure was evaluated. As in Chapter 2, it was demonstrated that the internal structure of the porous material changes depending on the process, and that the three-dimensional observation method used in this study can be applied to the hydroxyapatite porous material.

Chapter 5

The use of the hydroxyapatite porous material as a water purification filter was investigated. In this chapter, the porous material tested its ability as a filter to remove bacteria and viruses from contaminated liquids. A buffer solution containing E. coli at a concentration of 2.4×10^{7} cells/ml was filtered by suction four times in succession, each 5 ml, and it was confirmed that the liquid after filtration contained no detectable concentration of E. coli. In addition, a buffer solution containing human coronavirus 229E at a virus infectious titer of 1.8×10^{5} TCID50/ml was suctioned and filtered twice in succession at 5 ml each time, and 99.998% of the virus was removed by filtration. These results indicated the applicability of the hydroxyapatite porous material as a polluted water purification filter.

Improvement of the functionality of porous ceramics by controlling the pore structure of the ceramics using starch, which forms a network structure, as a pore-forming agent was clarified. The three-dimensional observation method of the internal structure was applied to the two types of ceramics; i.e., zeolite and hydroxyapatite. The method can be applied in principle to any material to which the liquid immersion method can be used, as an additional characterization technique for the structure of porous ceramics.

References

[1] M. Thommes, K. Kaneko, A. Neimark, J. Olivier, F. Rodriguez-Reinoso, J. Rouquerol, K. Sing, Physisorption of gases, with special reference to the evaluation of surface area and pore size distribution (IUPAC Technical Report), Pure and Applied Chemistry 87(9-10) (2015) 1051-1069.

[2] K. Kaneko, H. Otsuka, New IUPAC recommendation and characterization of nanoporous materials with physical adsorption, Accounts of Materials & Surface Research 5(2) (2020) 25-32.

[3] T. Ohji, M. Fukushima, Macro-porous ceramics: processing and properties, International Materials Reviews 57(2) (2012) 115-131.

[4] E.K. Lee, W.J. Koros, "Membranes, Synthetic, Applications" in Encyclopedia of Physical Science and Technology Third Edition, Elsevior 2003

[5] H. Roberge, P. Moreau, E. Couallier, P. Abellan, Determination of the key structural factors affecting permeability and selectivity of PAN and PES polymeric filtration membranes using 3D FIB/ SEM, Journal of Membrane Science 653 (2022).

[6] M. Furuta, Y. Mukai, E. Iritani, H. Nakakura, Evaluation of Retention Performance of Submicron Particle by Ceramic Microfiltration Membrane, Journal of the Society of Powder Technology Japan 43 (2006) pp.270-277.

[7] R. Singh, N. Hankins, Introduction to Membrane Processes for Water Treatment. In Emerging Membrane Technology for Sustainable Water Treatment, Elsevier, Amsterdam, 2016.

[8] T. Giakoumis, C. Vaghela, N. Voulvoulis, The role of water reuse in the circular economy' in Advances in Chemical Pollution, Environmental Management and Protection, 2020, pp. pp.227-252.

[9] B. Zdravkov, J. Čermák, M. Šefara, J. Janků, Pore classification in the characterization of porous materials: A perspective, Open Chemistry 5(2) (2007) 385-395.

[10] Y. Takeuchi, Porous Materials - Characterization, Production and Application -, Fuji-Techno System, Japan, 1999.

[11] J. Rouquerol, D. Avnir, C.W. Fairbridge, D.H. Everett, J.M. Haynes, N. Pernicone, J.D.F. Ramsay, K.S.W. Sing, K.K. Unger, Recommendations for the characterization of porous solids (Technical Report), Pure and Applied Chemistry 66(8) (1994) 1739-1758.

[12] Y. Chen, N. Wang, O. Ola, Y. Xia, Y. Zhu, Porous ceramics: Light in weight but heavy in energy and environment technologies, Materials Science & Engineering R-Reports 143 (2021).

[13] E.C. Hammel, O.L.R. Ighodaro, O.I. Okoli, Processing and properties of advanced porous ceramics: An application based review, Ceramics International 40(10) (2014) 15351-15370.

[14] A. Studart, U. Gonzenbach, E. Tervoort, L. Gauckler, Processing routes to macroporous ceramics: A review, Journal of the American Ceramic Society 89(6) (2006) 1771-1789.

[15] F. Payri, A. Broatch, J.R. Serrano, P. Piqueras, Experimental–theoretical methodology for determination of inertial pressure drop distribution and pore structure properties in wall-flow diesel particulate filters (DPFs), Energy 36(12) (2011) 6731-6744.

[16] E. Kikuchi, U. Imizu, K. Segawa, A. Tada, H. Hattori, Novel catalytic chemistry (Atarashii Shokubai Kagaku), Sankyo Shuppan Co.,Ltd. 2019.

[17] E. Bissett, Mathematical-Model Of The Thermal Regeneration of A Wall-Flow Monolith Diesel Particulate Filter, Chemical Engineering Science 39(7-8) (1984) 1233-1244.

[18] R. Khobragade, S. Singh, P. Shukla, T. Gupta, A. Al-Fatesh, A. Agarwal, N. Labhasetwar, Chemical composition of diesel particulate matter and its control, Catalysis Reviews-Science and Engineering 61(4) (2019) 447-515.

[19] NGK Inslater, Ltd., Diesel particle filters (https://www.ngk-insulators.com/en/product/search-business/automobile/), 2022. (Accessed Dec.13 2022).

[20] M.D. Sobsey, C.E. Stauber, L.M. Casanova, J.M. Brown, M.A. Elliott, Point of Use Household Drinking Water Filtration: A Practical, Effective Solution for Providing Sustained Access to Safe Drinking Water in the Developing World, Environmental Science & Technology 42(12) (2008) 4261-4267.

[21] H. Yang, S. Xu, D. Chitwood, Y. Wang, Ceramic water filter for point-of-use water treatment in developing countries: Principles, challenges and opportunities, Frontiers of Environmental Science & Engineering 14(5) (2020).

[22] M.W. Hakami, A. Alkhudhiri, S. Al-Batty, M.P. Zacharof, J. Maddy, N. Hilal, Ceramic Microfiltration Membranes in Wastewater Treatment: Filtration Behavior, Fouling and Prevention, Membranes 10(9) (2020) 248.

[23] The Americal Ceramics Society, Ceramics for clean water: Nanofiltration membranes break separation limits (https://ceramics.org/tag/ceramic-membrane) , 2017. (Accessed Dec.13 2022).

[24] NGK Inslater, Ltd., NGK Ceramic filters Cefilt® (https://www.ngk.co.jp/product/cm-cefilt.html), 2022. (Accessed Dec.13 2022)

[25] T. Nakajima, T. Ogawa, Application of Hydroxyapatite ceramics as Artificial Bone (in Japanese), Inorganic Materials 6 (1999) 231-237.

[26] M. Sakamoto, M. Nakasu, T. Matsumoto, H. Okihana, Development of superporous hydroxyapatites and their examination with a culture of primary rat osteoblasts, Journal of Biomedical Materials Research Part A 82A(1) (2007) 238-242.

[27] M. Sakamoto, Development and evaluation of superporous hydroxyapatite ceramics with triple pore structure as bone tissue scaffold, Journal of the Ceramic Society of Japan 118(1380) (2010) 753-757.

[28] T. Nakajima, Ceramics Archives, CERAMICS JAPAN 43 (2008) 984-986.

[29] C. Murphy, M. Haugh, F. O'Brien, The effect of mean pore size on cell attachment, proliferation and migration in collagen-glycosaminoglycan scaffolds for bone tissue engineering, Biomaterials 31(3) (2010) 461-466.

[30] A. Corma, From Microporous to Mesoporous Molecular Sieve Materials and Their Use in Catalysis, Chemical Reviews 97(6) (1997) 2373-2420.

[31] C. Marcilly, Present status and future trends in catalysis for refining and petrochemicals, Journal of Catalysis 216(1-2) (2003) 47-62.

[32] M. Matsukura, F. Kurosaki, Development of Zeolite-Based Adsorbents for Highly Contaminated Water in Fukushima, Journal of Ion Exchange 28(3) (2017) pp.51-57.

[33] B. Yilmaz, U. Müller, Catalytic Applications of Zeolites in Chemical Industry, Topics in Catalysis 52(6-7) (2009) 888-895.

[34] S. Mitchell, N.-L. Michels, J. Pérez-Ramírez, From powder to technical body: the undervalued science of catalyst scale up, Chemical Society Reviews 42(14) (2013) 6094.

[35] M. Yu, R.D. Noble, J.L. Falconer, Zeolite Membranes: Microstructure Characterization and Permeation Mechanisms, Accounts of Chemical Research 44(11) (2011) 1196-1206.

[36] C. Baerlocher, L. McCusker, Database of Zeolite Structures: (http://www.iza-structure.org/databases/) (Accessed in 2023), 2022.

[37] J. Jiang, J. Yu, A. Corma, Extra-Large-Pore Zeolites: Bridging the Gap between Micro and Mesoporous Structures, Angewandte Chemie-International Edition 49(18) (2010) 3120-3145.

[38] L. Bieseki, R. Simancas, J. Jorda, P. Bereciartua, A. Cantin, J. Simancas, S. Pergher, S. Valencia, F. Rey, A. Corma, Synthesis and structure determination via ultra-fast electron diffraction of the

new microporous zeolitic germanosilicate ITQ-62, Chemical Communications 54(17) (2018) 2122-2125.

[39] E. Kapaca, J. Jiang, J. Cho, J. Jorda, M. Diaz-Cabanas, X. Zou, A. Corma, T. Willhammar, Synthesis and Structure of a 22 x 12 x 12 Extra-Large Pore Zeolite ITQ-56 Determined by 3D Electron Diffraction, Journal of the American Chemical Society 143(23) (2021) 8713-8719.

[40] J. Beck, J. Vartuli, W. Roth, M. Leonowicz, C. Kresge, K. Schmitt, C. Chu, D. Olson, E. Sheppard, S. Mccullen, J. Higgins, J. Schlenker, A New Family of Mesoporous Molecular-Sieves Prepared with Liquid-Crystal Templates, Journal of the American Chemical Society 114(27) (1992) 10834-10843.

[41] C. Kresge, M. Leonowicz, W. Roth, J. Vartuli, J. Beck, Ordered mesoporous molecular-sieves synthesized by a liquid-crystal template mechanism, Nature 359(6397) (1992) 710-712.

[42] S. Inagaki, Y. Fukushima, K. Kuroda, Synthesis of highly ordered mesoporous materials from a layered polysilicate, Journal of the Chemical Society, Chemical Communications (8) (1993) 680.

[43] S. Fujita, S. Inagaki, Mesoporous Organic-Inorganic Hybrid Films, MEMBRANE (Japanese) 32(6) (2007) 318-324.

[44] M. Waki, S. Shirai, K.-I. Yamanaka, Y. Maegawa, S. Inagaki, Heterogeneous water oxidation photocatalysis based on periodic mesoporous organosilica immobilizing a tris(2,2′-bipyridine)ruthenium sensitizer, RSC Advances 10(24) (2020) 13960-13967.

[45] M. Waki, Y. Maegawa, K. Hara, Y. Goto, S. Shirai, Y. Yamada, N. Mizoshita, T. Tani, W. Chun, S. Muratsugu, M. Tada, A. Fukuoka, S. Inagaki, A Solid Chelating Ligand: Periodic Mesoporous Organosilica Containing 2,2 '-Bipyridine within the Pore Walls, Journal of the American Chemical Society 136(10) (2014) 4003-4011.

[46] N. Mizoshita, T. Tani, S. Inagaki, Syntheses, properties and applications of periodic mesoporous organosilicas prepared from bridged organosilane precursors, Chemical Society Reviews 40(2) (2011) 789-800.

[47] K. Kuroda, Silica-based mesoporous molecular sieves derived from a layered polysilicate kanemite - A review, Journal of Porous Materials 3(2) (1996) 107-114.

[48] V. Luca, D.J. Maclachlan, J.M. Hook, R. Withers, Synthesis and Characterization of Mesostructured Vanadium Oxide, Chemistry of Materials 7(12) (1995) 2220-2223.

[49] D. Lu, T. Katou, M. Uchida, J.N. Kondo, K. Domen, In Situ TEM Observation of Crystallization of Amorphous Ordered Mesoporous Nb−Ta and Mg−Ta Mixed Oxides, Chemistry of Materials 17(3) (2005) 632-637.

[50] S.L. James, Metal-organic frameworks, Chemical Society Reviews 32(5) (2003) 276.

[51] K. Nakanishi, N. Tanaka, Sol–Gel with Phase Separation. Hierarchically Porous Materials Optimized for High-Performance Liquid Chromatography Separations, Accounts of Chemical Research 40(9) (2007) 863-873.

[52] T. Tomita, K. Nakayama, H. Sakai, Gas separation characteristics of DDR type zeolite membrane, Microporous and Mesoporous Materials 68(1-3) (2004) 71-75.

[53] K. Kusakabe, S. Yoneshige, A. Murata, S. Morooka, Morphology and gas permeance of ZSM-5-type zeolite membrane formed on a porous alpha-alumina support tube, Journal of Membrane Science 116(1) (1996) 39-46.

[54] K. Kusakabe, T. Kuroda, S. Morooka, Separation of carbon dioxide from nitrogen using ion-exchanged faujasite-type zeolite membranes formed on porous support tubes, Journal of Membrane Science 148(1) (1998) 13-23.

[55] S. Morooka, T. Kuroda, K. Kusakabe, T. Inui, M. Anpo, K. Izui, S. Yanagida, T. Yamaguchi, Carbon dioxide separation from nitrogen using Y-type zeolite membranes, Advances in Chemical Conversions For Mitigating Carbon Dioxide 114 (1998) 665-668.

[56] Z. Vroon, K. Keizer, M. Gilde, H. Verweij, A. Burggraaf, Transport properties of alkanes through ceramic thin zeolite MFI membranes, Journal of Membrane Science 113(2) (1996) 293-300.

[57] H. Hasegawa, K. Nishida, S. Oguro, Y. Fujimura, K. Yajima, M. Niino, M. Isomura, T. Tomita, T. Dixon, L. Laloui, S. Twinning, Gas separation process for CO_2 removal from natural gas with DDR-type zeolite membrane, 13th International Conference on Greenhouse Gas Control Technologies, GHGT-13 114 (2017) 32-36.

[58] J.C. Díaz, I.D. Gil-Chávez, L. Giraldo, J.C. Moreno-Piraján, Separation of Ethanol-Water MixtureUsing Type-A Zeolite Molecular Sieve, E-Journal of Chemistry 7(2) (2010) 483-495.

[59] T. Kyotani, Study on Mcroscopic Structure and Dehydration Characteristic of Tubular Zeolite Membrane, BUNSEKI KAGAKU 68(1) (2019) 9-21.

[60] S. Holmes, M. Schmitt, C. Markert, R. Plaisted, J. Forrest, P. Sharratt, A. Garforth, C. Cundy, J. Dwyer, Zeolite A membranes for use in alcohol/water separations - Part I: Experimental investigation, Chemical Engineering Research & Design 78(A8) (2000) 1084-1088.

[61] M. Aizawa, T. Matsuura, Z. Zhuang, Syntheses of Single-Crystal Apatite Particles with Preferred Orientation to the a- and c-Axes as Models of Hard Tissue and Their Applications, Biological & Pharmaceutical Bulletin 36(11) (2013) 1654-1661.

[62] M. Pasero, A. Kampf, C. Ferraris, I. Pekov, J. Rakovan, T. White, Nomenclature of the apatite supergroup minerals, European Journal of Mineralogy 22(2) (2010) 163-179.

[63] S. Rujitanapanich, P. Kumpapan, P. Wanjanoi, P. Yupapin, S. PivsaArt, H. Ohgaki, Synthesis of Hydroxyapatite from Oyster Shell via Precipitation, 11th Eco-Energy and Materials Science and Engineering (11th Emses) 56 (2014) 112-117.

[64] M. Aizawa, Development of bioceramics with life functions by harnessing crystallographic anisotropy and their biological evaluations, Journal of the Ceramic Society of Japan 128(12) (2020) 997-1004.

[65] H. Yang, S. Xu, D.E. Chitwood, Y. Wang, Ceramic water filter for point-of-use water treatment in developing countries: Principles, challenges and opportunities, Frontiers of Environmental Science & Engineering 14(5) (2020).

[66] L. Yang, T. Yamamoto, Quantification of Virus Particles Using Nanopore-Based Resistive-Pulse Sensing Techniques, Frontiers in Microbiology 7 (2016).

[67] C. Cundy, P. Cox, The hydrothermal synthesis of zeolites: History and development from the earliest days to the present time, Chemical Reviews 103(3) (2003) 663-701.

[68] H. Tominaga, Science and application of zeolite (Zeolite no kagaku to ouyou), KODANSHA LTD.1998.

[69] C. Baerlocher, L.B. McCusker, Database of Zeolite Structures:, (http://www.iza-structure.org/databases/). 1996. (Accessed Dec.12 2022).

[70] R. Bingre, B. Louis, P. Nguyen, An Overview on Zeolite Shaping Technology and Solutions to Overcome Diffusion Limitations, Catalysts 8(4) (2018) 163.

[71] J. Sun, C. Bonneau, A. Cantin, A. Corma, M. Diaz-Cabanas, M. Moliner, D. Zhang, M. Li, X. Zou, The ITQ-37 mesoporous chiral zeolite, Nature 458(7242) (2009) 1154-1158.

[72] M. Iwamoto, N. Mizuno, H. Yahiro, Removal of Nitrogen Monoxide over Copper Ion-exchanged Zeolite Catalysts., Journal of The Japan Petroleum Institute 34(5) (1991) 375-390.

[73] C. Cundy, P. Cox, The hydrothermal synthesis of zeolites: Precursors, intermediates and reaction mechanism, Microporous and Mesoporous Materials 82(1-2) (2005) 1-78.

[74] Y. Kubota, T. Tatsumi, Recent Developments in Zeolite Science and Technology, Journal of the Vacuum Society of Japan 49(4) (2006) pp.205-212.

[75] J.E. Schmidt, D. Xie, M.E. Davis, Synthesis of the RTH-type layer: the first small-pore, two dimensional layered zeolite precursor, Chemical Science 6(10) (2015) 5955-5963.

[76] M.E. Davis, R.F. Lobo, Zeolite and molecular sieve synthesis, Chemistry of Materials 4(4) (1992) 756-768.

[77] T. Wakihara, T. Okubo, Hydrothermal synthesis and characterization of zeolites, Chemistry Letters 34(3) (2005) 276-281.

[78] Z. Liu, K. Okabe, C. Anand, Y. Yonezawa, J. Zhu, H. Yamada, A. Endo, Y. Yanaba, T. Yoshikawa, K. Ohara, T. Okubo, T. Wakihara, Continuous flow synthesis of ZSM-5 zeolite on the order of seconds, Proceedings of the National Academy of Sciences 113(50) (2016) 14267-14271.

[79] F. Crea, R. Aiello, A. Nastro, J. Nagy, Synthesis of ZSM-5 Zeolite from Very Dense Systems - Formation of Pelleted ZSM-5 Zeolite From (Na, Li, Tpa, Si, Al) Hydrogels, Zeolites 11(5) (1991) 521-527.

[80] Z. Liu, J. Zhu, T. Wakihara, T. Okubo, Ultrafast synthesis of zeolites: breakthrough, progress and perspective, Inorganic Chemistry Frontiers 6(1) (2019) 14-31.

[81] Y. Kamimura, W. Chaikittisilp, K. Itabashi, A. Shimojima, T. Okubo, Critical Factors in the Seed-Assisted Synthesis of Zeolite Beta and “Green Beta” from OSDA-Free Na^{+}-Aluminosilicate Gels, Chemistry - An Asian Journal 5(10) (2010) 2182-2191.

[82] J. Zhu, Z. Liu, A. Endo, Y. Yanaba, T. Yoshikawa, T. Wakihara, T. Okubo, Ultrafast, OSDA-free synthesis of mordenite zeolite, Crystengcomm 19(4) (2017) 632-640.

[83] Y. Kamimura, S. Tanahashi, K. Itabashi, A. Sugawara, T. Wakihara, A. Shimojima, T. Okubo, Crystallization Behavior of Zeolite Beta in OSDA-Free, Seed-Assisted Synthesis, Journal of Physical Chemistry C 115(3) (2011) 744-750.

[84] J. Tomita, S. Elangovan, K. Itabashi, A. Chokkalingam, H. Fujinuma, Z. Hao, A. Kanno, K. Hayashi, K. Iyoki, T. Wakihara, T. Okubo, OSDA-free synthesis of zeolite beta: Broadening the methodology for a successful use of the product as a seed, Advanced Powder Technology 33(9) (2022).

[85] M. Pan, Y. Lin, Template-free secondary growth synthesis of MFI type zeolite membranes, Microporous and Mesoporous Materials 43(3) (2001) 319-327.

[86] N. Nishiyama, K. Ueyama, M. Matsukata, Synthesis of defect-free zeolite-alumina composite membranes by a vapor-phase transport method, Microporous Materials 7(6) (1996) 299-308.

[87] C. Matsunaga, T. Uchikoshi, T. Suzuki, Y. Sakka, M. Matsuda, Fabrication of the c-axis oriented zeolite L compacts using strong magnetic field, Materials Letters 93 (2013) 408-410.

[88] W. Xu, J. Dong, J. Li, J. Li, F. Wu, A Novel Method for the Preparation of Zeolite ZSM-5, Journal of the Chemical Society-Chemical Communications (10) (1990) 755-756.

[89] M. Kim, H. Li, M. Davis, Synthesis of Zeolites by Water-Organic Vapor-Phase Transport, Microporous Materials 1(3) (1993) 191-200.

[90] M. Matsukata, M. Ogura, T. Osaki, P. Rao, M. Nomura, E. Kikuchi, Conversion of dry gel to microporous crystals in gas phase, Topics in Catalysis 9(1-2) (1999) 77-92.

[91] C. Bian, C. Zhang, S. Pan, F. Chen, W. Zhang, X. Meng, S. Maurer, D. Dai, A.-N. Parvulescu, U. Müller, F.-S. Xiao, Generalized high-temperature synthesis of zeolite catalysts with unpredictably high space-time yields (STYs), Journal of Materials Chemistry A 5(6) (2017) 2613-2618.

[92] K. Takizawa, M. Ogura, Synthesis of zeolite-mesoporous material composite by steam-assisted crystallization, Journal of Institute of Industrial Science, The University of Tokyo 59(3) (2007).

[93] P. Colombo, Conventional and novel processing methods for cellular ceramics, Philosophical Transactions of the Royal Society a-Mathematical Physical and Engineering Sciences 364(1838) (2006) 109-124.

[94] I. Kim, J. Park, Y. Han, S. Kim, J. Shackelford, Wet Foam Stability from Colloidal Suspension to Porous Ceramics: A Review, Journal of the Korean Ceramic Society 56(3) (2019) 211-232.

[95] M. Bohner, F. Buchanan, Bioresorbable ceramics, Degradation Rate of Bioresorbable Materials: Prediction and Evaluation (2008) 95-114.

[96] M. Bohner, B.L.G. Santoni, N. Döbelin, β-tricalcium phosphate for bone substitution: Synthesis and properties, Acta Biomaterialia 13 (2020) pp.23-41.

[97] S. Dorozhkin, Bioceramics of calcium orthophosphates, Biomaterials 31(7) (2010) 1465-1485.

[98] P. Colombo, H. Degischer, Highly porous metals and ceramics, Materials Science and Technology 26(10) (2010) 1145-1158.

[99] M. Descamps, T. Duhoo, F. Monchau, J. Lu, P. Hardouin, J. Hornez, A. Leriche, Manufacture of macroporous beta-tricalcium phosphate bioceramics, Journal of the European Ceramic Society 28(1) (2008) 149-157.

[100] P. Colombo, Engineering porosity in polymer-derived ceramics, Journal of the European Ceramic Society 28(7) (2008) 1389-1395.

[101] H. Alves, G. Tari, A. Fonseca, J. Ferreira, Processing of porous cordierite bodies by starch consolidation, Materials Research Bulletin 33(10) (1998) 1439-1448.

[102] Z. Chen, G. Xu, H. Cui, X. Zhang, X. Zhan, Preparation of porous Al2O3 ceramics by starch consolidation casting method, International Journal of Applied Ceramic Technology 15(6) (2018) 1550-1558.

[103] A. Diaz, S. Hampshire, Characterisation of porous silicon nitride materials produced with starch, Journal of the European Ceramic Society 24(2) (2004) 413-419.

[104] Z. Zivcova, M. Cerny, W. Pabst, E. Gregorova, Elastic properties of porous oxide ceramics prepared using starch as a pore-forming agent, Journal of the European Ceramic Society 29(13) (2009) 2765-2771.

[105] Z. Zivcova-Vlckova, J. Locs, M. Keuper, I. Sedlarova, M. Chmelickova, Microstructural comparison of porous oxide ceramics from the system Al_2O_3-ZrO_2 prepared with starch as a pore-forming agent, Journal of the European Ceramic Society 32(10) (2012) 2163-2172.

[106] E. Gregorova, W. Pabst, I. Bohacenko, Characterization of different starch types for their application in ceramic processing, Journal of the European Ceramic Society 26(8) (2006) 1301-1309.

[107] M. Sandoval, M. Talou, A. Martinez, M. Camerucci, E. Gregorova, W. Pabst, Porous cordierite-based ceramics processed by starch consolidation casting -Microstructure and high-temperature mechanical behavior, Ceramics International 44(4) (2018) 3893-3903.

[108] O. Lyckfeldt, J.M.F. Ferreira, Processing of porous ceramics by 'starch consolidation', Journal of the European Ceramic Society 18(2) (1998) 131-140.

[109] E. Gregorova, W. Pabst, Porosity and pore size control in starch consolidation casting of oxide ceramics - Achievements and problems, Journal of the European Ceramic Society 27(2-3) (2007) 669-672.

[110] R. Khattab, M. Wahsh, N. Khalil, Preparation and characterization of porous alumina ceramics through starch consolidation casting technique, Ceramics International 38(6) (2012) 4723-4728.

[111] K. Lim, Y. Kim, I. Song, Porous sodium borate-bonded SiC ceramics, Ceramics International 39(6) (2013) 6827-6834.

[112] M. Wang, F. Liu, Y. Chen, J. Gao, Fabrication of Macroporous Biomorphic SiC from Cellulose Nanofibers Aerogel, Materials 11(12) (2018).

[113] L. Fang, C. Chen, Y. Wang, Carbon Fibers and Graphite as Pore-Forming Agents for the Obtention of Porous Alumina: Correlating Physical and Fractal Characteristics, Fractal and Fractional 6(9) (2022).

[114] A. Celik, G. Caglar, Y. Celik, Fabrication of porous Al2O3 ceramics using carbon black as a pore forming agent by spark plasma sintering, Ceramics International 48(19) (2022) 28181-28190.

[115] Y. Shao, D. Jia, Y. Zhou, B. Liu, Novel Method for Fabrication of Silicon Nitride/Silicon Oxynitride Composite Ceramic Foams Using Fly Ash Cenosphere as a Pore-Forming Agent, Journal of the American Ceramic Society 91(11) (2008) 3781-3785.

[116] Y. Shao, D. Jia, B. Liu, Characterization of porous silicon nitride ceramics by pressureless sintering using fly ash cenosphere as a pore-forming agent, Journal of the European Ceramic Society 29(8) (2009) 1529-1534.

[117] K. Okada, F. Ikawa, T. Isobe, Y. Kameshima, A. Nakajima, Low temperature preparation and machinability of porous ceramics from talc and foamed glass particles, Journal of the European Ceramic Society 29(6) (2009) 1047-1052.

[118] T. Fukasawa, Z.-Y. Deng, M. Ando, T. Ohji, S. Kanzaki, Synthesis of Porous Silicon Nitride with Unidirectionally Aligned Channels Using Freeze-Drying Process, Journal of the American Ceramic Society 85(9) (2002) 2151-2155.

[119] M. Fukushima, S. Tsuda, Y.-I. Yoshizawa, Fabrication of Highly Porous Alumina Prepared by Gelation Freezing Route with Antifreeze Protein, Journal of the American Ceramic Society 96(4) (2013) 1029-1031.

[120] M. Fukushima, Y.-I. Yoshizawa, T. Ohji, Macroporous Ceramics by Gelation-Freezing Route Using Gelatin, Advanced Engineering Materials 16(6) (2014) 607-620.

[121] H. Ge, G. Wang, B. Yuan, B. Dong, H. Li, Fabrication and microstructure of porous SiC ceramics using suspension emulsions as pore-forming agents, Ceramics International 40(8) (2014) 11705-11711.

[122] M.D.M. Innocentini, P. Sepulveda, V.R. Salvini, V.C. Pandolfelli, J.R. Coury, Permeability and Structure of Cellular Ceramics: A Comparison between Two Preparation Techniques, Journal of the American Ceramic Society 81(12) (1998) 3349-3352.

[123] E. Vogli, H. Sieber, P. Greil, Biomorphic SiC-ceramic prepared by Si-vapor phase infiltration of wood, Journal of the European Ceramic Society 22(14-15) (2002) 2663-2668.

[124] C.R. Rambo, H. Sieber, Novel Synthetic Route to Biomorphic Al_2O_3 Ceramics, Advanced Materials 17(8) (2005) 1088-1091.

[125] B. Ben-Nissan, Natural bioceramics: from coral to bone and beyond, Current Opinion in Solid State & Materials Science 7(4-5) (2003) 283-288.

[126] Y. Lee, Y. Kim, K. Jun, N. Viswanadham, J. Bae, H. Park, Textural Properties and Catalytic Applications of ZSM-5 Monolith Foam for Methanol Conversion, Catalysis Letters 129(3-4) (2009) 408-415.

[127] M. Anderson, S. Holmes, N. Hanif, C. Cundy, Hierarchical pore structures through diatom zeolitization, Angewandte Chemie-International Edition 39(15) (2000) 2707-2710.

[128] U. Gonzenbach, A. Studart, E. Tervoort, L. Gauckler, Macroporous ceramics from particle-stabilized wet foams, Journal of the American Ceramic Society 90(1) (2007) 16-22.

[129] F. Li, M. Liang, X. Ma, X. Huang, G. Zhang, Preparation and characterization of stoichiometric zirconium carbide foams by direct foaming of zirconia sols, Journal of Porous Materials 22(2) (2015) 493-500.

[130] P. Sepulveda, F. Ortega, M. Innocentini, V. Pandolfelli, Properties of highly porous hydroxyapatite obtained by the gelcasting of foams, Journal of the American Ceramic Society 83(12) (2000) 3021-3024.

[131] T. Tomita, S. Kawasaki, K. Okada, Effect of viscosity on preparation of foamed silica ceramics by a rapid gelation foaming method, Journal of Porous Materials 12(2) (2005) 123-129.

[132] S. Hizukuri, K. Ito, I. Maeda, Z. Nikuni, Temperature Dependence of Retrogradation of Starch Pastes, Journal of the Japanese Society of Starch Science 19(2) (1972) 70-75.

[133] A. Buléon, P. Colonna, V. Planchot, S. Ball, Starch granules: structure and biosynthesis, International Journal of Biological Macromolecules 23(2) (1998) 85-112.

[134] K. Ishii, M. Shimizu, H. Sameshima, S. Samitsu, T. Ishigaki, T. Uchikoshi, Fabrication of porous (Ba,Sr)(Co,Fe)O3-delta (BSCF) ceramics using gelatinization and retrogradation phenomena of starch as pore-forming agent, Ceramics International 46(9) (2020) 13047-13053.

[135] S. Goto, Measurements of pore structure, Journal of the Clay Science Society of Japan 24(1) (1984).

[136] S. Gregg, K. Sing, ”Adsorption, Surface Area and Porosity” 2n^{d} Edhition Academic Press1982.

[137] M. Konno, Y. Suzuki, H. Inada, K. Nakamura, G. Moebus, T. Walther, R. Brydson, D. Ozkaya, M. I, S. Donnelly, P. Nellist, Z. Li, R. Baker, Y. Chiu, High-resolution SEM observation at the atomic level using a dedicated STEM with aberration correction, Electron Microscopy and Analysis Group Conference 2011 (Emag 2011) 371 (2012).

[138] K. Sing, The Use of Gas-Adsorption for the Characterization of Porous Solids, Colloids and Surfaces 38(1-3) (1989) 113-124.

[139] S. Gregg, K. Sing, The Effect of Heat Treatment on the Surface Properties of Gibbsite .1. Adsorption Isotherms of Nitrogen and of Oxygen at -182.7-degrees-C, Journal of Physical and Colloid Chemistry 55(4) (1951) 592-597.

[140] S. Brunauer, P. Emmett, E. Teller, Adsorption of gases in multimolecular layers, Journal of the American Chemical Society 60 (1938) 309-319.

[141] G. Nicolis, I. Prigogine, Fluctuations in Nonequilibrium Systems, Proceedings of the National Academy of Sciences 68(9) (1971) 2102-2107.

[142] K. Mukaida, Study on the Measurement of the Pore Structure of Porous Matter, Journal of the Society of Powder Technology, Japan 16(9) (1979).

[143] S. Kondo, T. Ishikawa, I. Abe, Adsorption Science (Kyuutyaku-no-kagaku) 3rd Edition, Maruzen Publishing Co.,Ltd., Japan, 2020.

[144] E. Barrett, L. Joyner, P. Halenda, The Determination of Pore Volume and Area Distributions in Porous Substances .1. Computations from Nitrogen Isotherms, Journal of the American Chemical Society 73(1) (1951) 373-380.

[145] C. Leon y Leon, New perspectives in mercury porosimetry, Advances in Colloid and Interface Science 76 (1998) 341-372.

[146] K. Takeuchi, K. Washio, Mercury porosimetry, Refractories (Taikabutsu) 41(7) (1989) pp.11-17.

[147] M. Furukawa, T. Hotta, K. Okamoto, H. Abe, M. Naito, K. Ewsuk, K. Nogi, M. Reiterer, A. Tomsia, S. Glass, R. Waesche, K. Uematsu, Effects of slurry preparation conditions on granule properties and the strength of alumina ceramics, Characterization and Control of Interfaces For High Quality Advanced Materials 146 (2005) 73-79.

[148] K. Uematsu, Immersion microscopy for detailed characterization of defects in ceramic powders and green bodies, Powder Technology 88(3) (1996) 291-298.

[149] K. Uematsu, Processing defects in ceramic powders and powder compacts, Advanced Powder Technology 25(1) (2014) 154-162.

[150] J. Jiang, Y. Yun, X. Zou, J. Jorda, A. Corma, ITQ-54: a multi-dimensional extra-large pore zeolite with 20 x 14 x 12-ring channels, Chemical Science 6(1) (2015) 480-485.

[151] A. Sala, E. Perez-Botella, J. Jorda, A. Cantin, F. Rey, S. Valencia, ITQ-69: A Germanium-Containing Zeolite and its Synthesis, Structure Determination, and Adsorption Properties, Angewandte Chemie-International Edition 60(21) (2021) 11745-11750.

[152] C.T. Kresge, M.E. Leonowicz, W.J. Roth, J.C. Vartuli, J.S. Beck, Ordered mesoporous molecular sieves synthesized by a liquid-crystal template mechanism, Nature 359(6397) (1992) 710-712.

[153] U. Ciesla, F. Schuth, Ordered mesoporous materials, Microporous and Mesoporous Materials 27(2-3) (1999) 131-149.

[154] S. Zou, M. Zhang, S. Mo, H. Cheng, M. Fu, P. Chen, L. Chen, W. Shi, D. Ye, Catalytic Performance of Toluene Combustion over Pt Nanoparticles Supported on Pore-Modified Macro-Meso-Microporous Zeolite Foam, Nanomaterials 10(1) (2020).

[155] E. Igi, Y. Kameshima, S. Nishimoto, M. Miyake, Fabrication of Large Porous ZSM-5 Bulk Bodies by a One-pot Hydrothermal Method, Chemistry Letters 41(11) (2012) 1414-1416.

[156] E. Igi, Y. Kameshima, S. Nishimoto, M. Miyake, Separation of alcohol/water mixtures by ZSM-5 bulk bodies prepared with a one-pot hydrothermal method, Microporous and Mesoporous Materials 208 (2015) 160-164.

[157] D. Olson, W. Haag, R. Lago, Chemical and Physical-Properties of the ZSM-5 Substitutional Series, Journal of Catalysis 61(2) (1980) 390-396.

[158] Handbook of Chemistry: Pure Chemistry II, 4th ed., Maruzen Publishing Co.,Ltd., Japan, 1993.

[159] M. Promentilla, T. Sugiyama, T. Hitomi, N. Takeda, Characterizing the 3D pore structure of hardened cement paste with synchrotron microtomography, Journal of Advanced Concrete Technology 6(2) (2008) 273-286.

[160] T. Sugiyama, M. Promentilla, T. Hitomi, N. Takeda, Application of synchrotron microtomography for pore structure characterization of deteriorated cementitious materials due to leaching, Cement and Concrete Research 40(8) (2010) 1265-1270.

[161] F. Tariq, R. Haswell, P. Lee, D. McComb, Characterization of hierarchical pore structures in ceramics using multiscale tomography, Acta Materialia 59(5) (2011) 2109-2120.

[162] T. Takigawa, Indoor air pollution by chemical substances and sick house syndrome, Japanese Journal of Occupational Medicine and Traumatology 54(5) (2006).

[163] E. Gallego, X. Roca, J.F. Perales, X. Guardino, Determining indoor air quality and identifying the origin of odour episodes in indoor environments, Journal of Environmental Sciences 21(3) (2009) 333-339.

[164] M. Hanazato, N. Suzuki, C. Koga, H. Nakaoka, C. Mori, A Study of Design for Reduction and Monitoring of Volatile Organic Compounds in Indoor Air: the Case of a Commercial Bank in Japan, Journal of Asian Architecture and Building Engineering 17(3) (2018) 573-579.

[165] Y. Shibasaki, M. Maeda, M. Suzuki, N. Takeda, Humidity control deodorant and method for producing (Chōshitsu shōshūzai oyobi sono seizō hōhō), Japan, 2004.

[166] LIXIL, Functional Interior wall tile: Ecocarat Plus (https://www.lixil.co.jp/lineup/tile/ecocarat/), 2023. (Accessed Jan. 23 2023).

[167]AIST, Humidity-controlling Construction Materials Employing Porous Ceramics (https://www.aist.go.jp/sst/en/exhibition/innovation_zone/zone28/index.html), 2023. (Accessed Jan.12 2023).

[168] B. Theng, B. Theng, The Clay Minerals, Formation and Properties of Clay-Polymer Complexes, 2nd Edition 4 (2012) 3-45.

[169] H. Fukumizu, S. Yokoyama, K. Kitamura, Study on a New Humidity Controlling Material Porous Soil “Allophane” —Design of Humidity Controlling Material— Resources processing (Kankyo-shigen-kougaku) 52 (2005) pp.128-135.

[170] Japan Industrial Standards, R1608, Testing methods for compressive strength of fine ceramics, Japanese Industrial Standard Committee, Japan, 2003.

[171] A. Shimizu, T. Noguchi, Outline of Japanese Architectural Standard Specification for Reinforced Concrete Works (JASS 5), Concr. J. 43 (2003) pp.23-29.

[172] F. Zok, On weakest link theory and Weibull statistics, Journal of the American Ceramic Society 100(4) (2017) 1265-1268.

[173] Shimadzu Corp., Basics of GC Analysis (https://www.an.shimadzu.co.jp/gc/support/faq/fundamentals/carrier_gas.htm), 2023. (Accessed Jun.22 2023).

[174] WHO/UNICEF(JMP), Progress on household drinking water, sanitation and hygiene 2000–2020: Five years into the SDGs, WHO/UNICEF Joint Monitoring Programme for Water Supply, Sanitation and Hygiene, 2021.

[175] M. Shannon, P. Bohn, M. Elimelech, J. Georgiadis, B. Marinas, A. Mayes, Science and technology for water purification in the coming decades, Nature 452(7185) (2008) 301-310.

[176] C. Wu, S. Ghosh, K. Martin, A. Pinto, V. Denef, T. Olson, N. Love, The microbial colonization of activated carbon block point-of-use (PoU) filters with and without chlorinated phenol disinfection by-products, Environmental Science-Water Research & Technology 3(5) (2017) 830-843.

[177] K. Goh, L. Setiawan, L. Wei, R. Si, A. Fane, R. Wang, Y. Chen, Graphene oxide as effective selective barriers on a hollow fiber membrane for water treatment process, Journal of Membrane Science 474 (2015) 244-253.

[178] A. Abdullayev, M. Bekheet, D. Hanaor, A. Gurlo, Materials and Applications for Low-Cost Ceramic Membranes, Membranes 9(9) (2019).

[179] D. Holzmann, D. Holzinger, G. Hesser, T. Schmidt, G. Knor, Hydroxyapatite nanoparticles as novel low-refractive index additives for the long-term UV-photoprotection of transparent composite materials, Journal of Materials Chemistry 19(43) (2009) 8102-8106.

[180] I. Arganda-Carreras, V. Kaynig, C. Rueden, K. Eliceiri, J. Schindelin, A. Cardona, H. Seung, Trainable Weka Segmentation: a machine learning tool for microscopy pixel classification, Bioinformatics 33(15) (2017) 2424-2426.

[181] C. Zhang, T. Uchikoshi, L. Liu, M. Kikuchi, I. Ichinose, Nest-like microstructured biocompatible membrane fabricated by hydrothermally-synthesized hydroxyapatite (HAp) whiskers, Journal of the European Ceramic Society 40(2) (2020) 513-520.

[182] R.A. Mulvenna, J.L. Weidman, B. Jing, J.A. Pople, Y. Zhu, B.W. Boudouris, W.A. Phillip, Tunable nanoporous membranes with chemically-tailored pore walls from triblock polymer templates, Journal of Membrane Science 470 (2014) 246-256.

[183] Y. Takahashi, Application of polydimethylsiloxane-based optical system for measuring optical density of microbial culture, Bioscience Biotechnology and Biochemistry 80(12) (2016) 2486-2489.

[184] S.L. Warnes, Z.R. Little, C.W. Keevil, Human Coronavirus 229E Remains Infectious on Common Touch Surface Materials, mBio 6(6) (2015) e01697-15-e01697.

[185] M. Kawamoto, T. Yamaji, K. Saito, Y. Shirasago, K. Satomura, T. Endo, M. Fukasawa, K. Hanada, N. Osada, Identification of Characteristic Genomic Markers in Human Hepatoma HuH-7 and Huh7.5.1-8 Cell Lines, Frontiers in Genetics 11 (2020).

[186] D. Hochdorfer, R. Businger, D. Hotter, C. Seifried, J. Solzin, Automated, label-free TCID50 assay to determine the infectious titer of virus-based therapeutics, Journal of Virological Methods 299 (2022).

[187] N. Grossman, E. Ron, C. Woldringh, Changes in Cell Dimensions during Amino-Acid Starvation of Escherichia-Coli, Journal of Bacteriology 152(1) (1982) 35-41.

Achievements

Publications:

1. Masako Uematsu, Kento Ishii, Sadaki Samitsu, Edhuan Bin Ismail, Izumi Ichinose, Naoki Ohashi, David Berthebaud, Jean-François Halet, Takamasa Ishigaki, Tetsuo Uchikoshi: “Fabrication and characterization of zeolite bulk body containing mesopores and macropores using starch as pore-forming agent”, Advanced Powder Technology Vol.33, No.6, 103626 (2022)

2. Masako Uematsu, Kento Ishii, Hiroki Sameshima, Megumi Ito, Thi Kim Ngan Nguyen, Takamasa Ishigaki, Tetsuo Uchikoshi: “Fabrication of hydroxyapatite porous body with connective pores using the self-networking property of rice starch powder by heat treatment”, Materials Letters. Vol.326, 132939 (2022)

3. 植松 昌子, 石井 健斗, 打越 哲郎: “共焦点レーザー蛍光顕微鏡によるセラミックス多孔体の高解像度３次元観察”, CERAMICS JAPAN, Vol.57, No.6, pp. 401-404 (2022)

Presentations:

1. 植松 昌子, 打越 哲郎:“マイクロリアクター用マクロメソポーラスゼオライトバルク体の作製”, 日本セラミックス協会, 第 59 回基礎科学討論会(2021 年 1 月, Online, 口頭発表)

2. 植松 昌子, 石井 健斗, 佐光 貞樹, 打越 哲郎 : “マクロ・メソ孔を有するゼオライトバルク体の作製と内部構造評価”, 日本セラミックス協会, 2021年日本セラミックス協会年会(2021 年 3 月, Online, 口頭発表)

3. 植松 昌子, 石井 健斗, 佐光 貞樹, 打越 哲郎: “多孔質ゼオライトバルク体の作製と階層的気孔構造の評価”, 粉体粉末冶金協会, 2021 年度春季大会 (2021 年 6 月, Online, 口頭発表)

4. 植松 昌子, 石井 健斗, 打越 哲郎 : “でんぷんを造孔剤に用いたアパタイトセラミックス多孔体の作製”, 触媒学会, 第 10 回 JACI/GSC シンポジウム(2021 年 6 月, Online, ポスター発表)

5. 植松 昌子, 石井 健斗, 佐光 貞樹, 打越 哲郎 : “スターチの糊化・老化現象を利用したゼオライト多孔質バルク体の作製”, 日本セラミックス協会, 第 3 回資源・環境関連材料部会討論会(2021 年 6 月, Online, 口頭発表)

6. 植松 昌子, 石井 健斗, 打越 哲郎: “共焦点レーザー蛍光顕微鏡による多孔質セラミックスの高解像度３次元観察”, 日本セラミックス協会, 第３４回秋季シンポジウム(2021 年 9 月, Online, 口頭発表)

7. 植松 昌子, 石井 健斗, 打越 哲郎: “連通孔を有するハイドロキシアパタイト多孔体の作製と内部構造観察”, 第 58 回粉体に関する討論会 (2021 年 9 月, Online, 口頭発表)

8. 植松 昌子, 石井 健斗, Edhuan Bin Ismail, 一ノ瀬 泉, 佐光 貞樹, 打越 哲郎: “連通気孔構造を有するゼオライトバルク体のガス透過性評価”, 粉体粉末冶金協会, 2021 年度秋季大会(2021 年 11 月, Online, 口頭発表)

9. Masako Uematsu, Kento Ishii, Edhuan Bin Ismail, Izumi Ichinose, Sadaki Samitsu, Tetsuo Uchikoshi : “Evaluation of gas permeability and mechanical property of ZSM-5 zeolite bulk with macro-porous networks”, 日本セラミックス協会, 第 60 回基礎科学討論会 (2022 年 1 月, 熊本, 口頭発表)

10. 植松 昌子, 石井 健斗, 佐光 貞樹, 打越 哲郎 : “スターチを造孔剤に用いたゼオライト多孔質バルク体の気孔構造解析”, 日本セラミックス協会, 2022 年日本セラミックス協会年会 (2022 年 3 月, Online, 口頭発表)

11. 植松 昌子, 伊藤 恵美, 石井 健斗, グェン ティ キム ンガン, 打越 哲郎 : “スターチ原料粉体の形態変化と多孔質セラミックス造孔剤への利用”, 粉体粉末冶金協会, 2022 年度春季大会 (2022 年 5 月, Online, 口頭発表)

12. Masako Uematsu, Kento Ishii, Tetsuo Uchikoshi : “Characterization of pore structure in ceramics bulk body by confocal laser fluorescent microscopy”, 粉体工学会, ICCCI2022 (2022 年 11 月, 富士吉田, 口頭発表)

13. 植松 昌子, Dalal Asker, 石井 健斗, Benjamin D. Hatton, 打越 哲郎 : “ハイドロキシアパタイトフィルターの作製とバクテリア汚染水の浄化性能の評価”, 日本セラミックス協会, 第 61 回基礎科学討論会 (2023 年 1 月, 岡山, 口頭発表)

Patent:

1. ゼオライトバルク体およびその製造方法, 特願 2021-205694 (出願日 2021-12-02)
   発明者 : 植松 昌子, 石井 健斗, 打越 哲郎

Awards:

1. 口頭発表「スターチの糊化・老化現象を利用したゼオライト多孔質バルク体の作製」により，日本セラミックス協会資源・環境関連材料部会から「2021 年度第 3 回資源・環境関連材料部会討論会優秀奨励賞」を受賞（2021 年 6 月 24 日）

2. 口頭発表「連通気孔構造を有するゼオライトバルク体のガス透過性評価」により，一般社団法人粉体粉末冶金協会から「2021 年度秋季大会優秀講演発表賞」を受賞（2021 年 11 月 11 日）